LOW FREQUENCY CRITICAL CURRENT NOISE AND TWO LEVEL SYSTEM
DEFECTS IN JOSEPHSON JUNCTIONS

BY

CHRISTOPHER DANIEL NUGROHO

DISSERTATION

Submitted in partial fulfillment of the requirements
for the degree of Doctor of Philosophy in Physics
in the Graduate College of the
University of Illinois at Urbana-Champaign, 2015

Urbana, Illinois

Doctoral Committee:

      Professor James Eckstein, Chair
      Professor Dale Van Harlingen, Director of Research
      Professor Michael Weissmann
      Associate Professor Mark Neubauer

ABSTRACT

The critical current in a Josephson junction is known to exhibit a $1/f^\alpha$ low frequency noise. Implemented as a superconducting qubit, this low frequency noise can lead to decoherence. While the $1/f$ noise has been known to arise from an ensemble of two level systems connected to the tunnel barrier, the precise microscopic nature of these TLSs remain a mystery.

In this thesis we will present measurements of the $1/f^\alpha$ low frequency noise in the critical current and tunneling resistance of Al-AlO$_x$-Al Josephson junctions. Measurements in a wide range of resistively shunted and unshunted junctions confirm the equality of critical current and tunneling resistance noise. That is the critical current fluctuation corresponds to fluctuations of the tunneling resistance. In not too small Al-AlO$_x$-Al junctions we have found that the fractional power spectral density scales linearly with temperature, described by the formula: $S_{I_c}/I_c^2 \equiv S_R/R^2 \approx 1 \times 10^{-13} (T(K)/A~(\mu\mathrm{m}^2)) 1/f$ Hz^{-1}.

We confirmed that the $1/f^\alpha$ power spectrum is the result of a large number of two level systems modulating the tunneling resistance. At small junction areas and low temperatures, the number of thermally active TLSs is insufficient to integrate out a featureless $1/f$ spectral shape. By analyzing the spectral variance in small junction areas, we deduced a TLS density of approximately, $n \approx 2.53$ per μm^2 per Kelvin spread in the TLS energy per factor e in the TLS lifetimes, or $\sigma_0 = 69.7~\mu\mathrm{m}^{-2}\mathrm{K}^{-1}$, consistent with the density of tunneling TLSs found in glassy insulators, as well as the density deduced from coherent TLSs interacting at qubit frequencies. This density combined with the magnitude of the $1/f$ power spectral density in large area junctions, gives an average TLS effective area, $\langle \delta A^2 \rangle \approx (0.3~\mathrm{nm}^2)^2$.

In ultra small tunnel junctions, $A \approx 0.008~\mu$m^2, we have studied the time-domain dynamics

of isolated TLSs. We have found a TLS whose dynamics is described by the quantum tunneling between the two localized wells, and a one-phonon absorption/emission switching rate. From the quantum limiting rate and the WKB approximation, we estimated that the TLS has a mass and tunneling distance product, $m^{1/2}d \approx 1.5 \times 10^{-23} \sqrt{\text{kg}}.\text{m}$, consistent with an atomic mass tunneling through crystal lattice distances, $d \sim 1$ Å. At higher temperatures TLSs have been found that obey a simple thermal activation dynamics.

By analyzing the TLS response to an external electric field, we have deduced that the TLS electric dipole is in the order of, $P \sim 1$ eÅ ~ 5 D, consistent with the TLS having the charge of one electron tunneling through a disorder potential of distances ~ 1 Å.

TABLE OF CONTENTS

LIST OF FIGURES

CHAPTER 1

INTRODUCTION

Superconducting quantum bits have developed into a promising quantum computing architecture. The absence of dissipation associated with superconductivity provides a natural platform for the manipulation of fragile quantum states, and their compatibility with microfabrication techniques provide a path towards scalability.

The superconducting qubit can interact strongly through the electromagnetic environment, a feature that allows for strong multi-qubit coupling accessible [9], but also makes controlling unwanted interactions difficult [80]. One of the challenges for superconducting qubits is therefore the minimization of decoherence [48]. The quantum state encoded into a qubit has to be preserved long enough for practical gate operations and multi-qubit coupling to take place. Unfortunately the qubit resides in a solid-state environment that contains a variety of defects, thus presenting numerous pathways for decoherence [48, 86].

Recent progress in superconducting qubits have resulted in longer coherence times [47]. How far this improvement can continue depends crucially on understanding the various decoherence mechanisms and developing strategies to mitigate them. One such decoherence source, and the topic of this thesis, is critical current fluctuations. The critical current of a Josephson junction is known to exhibit a low-frequency $1/f^\alpha$ ($\alpha \sim 1$) spectrum [67], which is generally understood to arise from a collection of TLSs in the tunnel barrier [74, 17]. Despite decades of research, the precise microscopic origin of these TLSs and the accompanying coupling mechanism remain relatively unknown.

1.1   Thesis organization

We will first discuss the background device physics of the Josephson junction and superconducting qubits, which will form the bulk of chapter 1. These will be invaluable in discussing critical current noise in the context of qubit decoherence.

In chapter 2 we will discuss how critical current factors into qubit decoherence. We will also describe the state of the field in critical current noise and discuss some of the motivations for the experiments in this thesis.

In chapter 3 we will introduce the well established foundations of $1/f$ noise, and a description of the tunneling TLS model which may be important to describe defects at low temperatures. Chapters 4 and 5 will discuss device fabrication and measurement methods.

The experiments, results, and analysis presented in this thesis are contained in chapters 6 and 7. In chapter 6 we will cover our measurements of the $1/f$ noise in Al-AlO$_x$-Al junctions. The second half of chapter 6 will discuss our observation of the breakdown of Gaussianity, thus the emergence of isolated two level systems. Chapter 7 will detail our measurements and analysis of individual TLSs in the time-domain.

Finally, we conclude the thesis with a brief discussion and some preliminary results of our experiments into the strain response of the TLSs and their dynamics in a highly disordered tunnel barrier (chapter 8). We will summarize and highlight our key findings in Chapter 9, which will conclude this thesis.

1.2   The Josephson Junction

The Josephson junction is central to many superconducting quantum circuits. In superconductors the electrons at the Fermi energy pair up with opposite momentum states $(\mathbf{k}, -\mathbf{k})$ forming a Cooper pair. A microscopic theory explaining the condensation of the Fermi electrons into a Cooper pair condensate is given by the BCS theory [7]. The central idea is that an electron can locally polarize the crystal by attracting the positively charged ions, which in turn provides

an attractive force for the second electron. If this attractive electron-phonon interaction is sufficiently strong to offset against the Coulomb repulsion, then the net attractive potential results in the pairing of the electrons.

The resulting superconducting order can be described by a macroscopic order parameter $\psi(\mathbf{r}) = \psi_0(\mathbf{r})e^{i\varphi(\mathbf{r})}$. If two superconducting regions are brought into contact through a weak link such as a thin insulating barrier, the exponentially decaying tail of the wavefunction from (I) can overlap into (II), and a phase difference $\Delta\varphi = \varphi_I - \varphi_{II}$ can exist across the junction and a supercurrent can flow through the junction. Intuitively this can be understood as the quantum mechanical tunneling of Cooper pairs. The supercurrent through the junction is given by the first Josephson relation, also called the current-phase relation:

$$I_s(\phi) = I_0 \sin\phi, \tag{1.1}$$

where I_s is the supercurrent through the junction, I_0 is the critical current, and $\phi = \Delta\varphi - 2\pi/\Phi_0 \int \mathbf{A} \cdot d\mathbf{s}$ is the gauge-invariant phase difference across the junction. More generally, stemming from the fact the wavefunction must be 2π periodic, the current-phase relation is given by the Fourier series:

$$I_s(\phi) = \sum_{n=1}^{\infty} I_{c,n} \sin(n\phi) \tag{1.2}$$

For the conventional superconductor-insulator-superconductor (SIS) tunnel junction, experiments have shown that the $n = 1$ term is the dominant contribution, thus the current-phase relation for SIS junctions take on the simple form of equation 1.1.

The second Josephson relation provides the relationship between the time evolution of the gauge-invariant phase ϕ to a voltage difference across the junction:

$$\frac{d\phi}{dt} = \frac{2eV}{\hbar}, \tag{1.3}$$

which leads to the ac-Josephson effect where a constant voltage V_0 across the junction leads

to a time evolution of the phase, $\phi(t) = \phi(0) + 2eV_0 t/\hbar$, and resulting in an *ac* supercurrent:

$$I_s = I_0 \sin \left(2\pi f_J t + \phi_0\right), \tag{1.4}$$

where f_J is the Josephson frequency given by:

$$f_J = \frac{2eV_0}{h} = \frac{V_0}{\Phi_0} \approx 0.48 \text{ GHz}/\mu\text{V} \tag{1.5}$$

The energy stored in the Josephson element can be obtained by considering the work done by an external battery in taking the junction from zero voltage to some voltage V. Using both the junction current-phase relation and the second Josephson relation:

$$E = \int_0^\tau IV \ dt = \frac{\hbar I_0}{2e} \int_0^\tau \sin\phi \frac{d\phi}{dt} \ dt = E_J \left(1 - \cos\phi\right), \tag{1.6}$$

where $E_J = \hbar I_0/2e$ is the Josephson energy. In the SIS junction an intrinsic capacitance is created by the geometry of the two electrodes separated by the thin insulating dielectric. This self-capacitance can often be approximated by a parallel plate geometry, $C_J = \epsilon A/d$, leading to a charging energy, $E_c = e^2/2C_J$. The competition between the Josephson energy and the junction charging energy is often characterized by the ratio E_J/E_C, which is one of the basic parameters when designing a qubit system.

Another property of the junction is its non-linear Josephson inductance, an important effect in all of the qubit systems and especially utilized in the fluxonium qubit to achieve a super-inductance [42]. From the definition of self-inductance, $V = L \ dI/dt$, we can use the Josephson relations to arrive at:

$$L_J = \frac{\Phi_0}{2\pi I_0 \cos\phi} \tag{1.7}$$

The importance of the Josephson inductance can be intuitively understood by considering the qubit as a quantized LC oscillator. The quantized LC oscillator has a harmonic potential, which results in regular $\hbar\omega$ energy spacings of the excitation spectrum. The non-linearity of

the Josephson inductance gives the required anharmonicity to isolate an effective two level system to form the qubit.

1.2.1 The Ambegaokar-Baratoff Relation

Ambegaokar and Baratoff [1] derived a relationship between the critical current I_c and the normal state resistance R_n:

$$I_c R_n = \frac{\pi \Delta}{2e} \tanh \left(\frac{\Delta}{2k_B T} \right),$$ (1.8)

and in the limit $T \to 0$:

$$I_c(0) R_n = \frac{\pi \Delta(0)}{2e}$$ (1.9)

Intuitively this can be understood by noting that the normal state resistance R_n parameterizes the tunneling probability, which is identical in the cases of Cooper pair and normal electron tunneling. More importantly in our discussion of noise processes, this relationship provides a link between critical current and resistive fluctuations. Additionally it is also useful as a practical tool to perform a quick estimate of the junction critical current based on its room temperature tunneling resistance.

1.2.2 The RCSJ Model

The circuit dynamics of the Josephson junction can be analyzed in the resistively and capacitively shunted junction (RCSJ) model. In this model the equation of motion for the Josephson junction is:

$$I = I_0 \sin \phi + \frac{V}{R} + C \frac{dV}{dt},$$ (1.10)

and in terms of the gauge-invariant phase ϕ:

$$I = I_0 \sin \phi + \frac{1}{R} \frac{\hbar}{2e} \frac{d\phi}{dt} + C \frac{\hbar}{2e} \frac{d^2\phi}{dt^2}$$ (1.11)
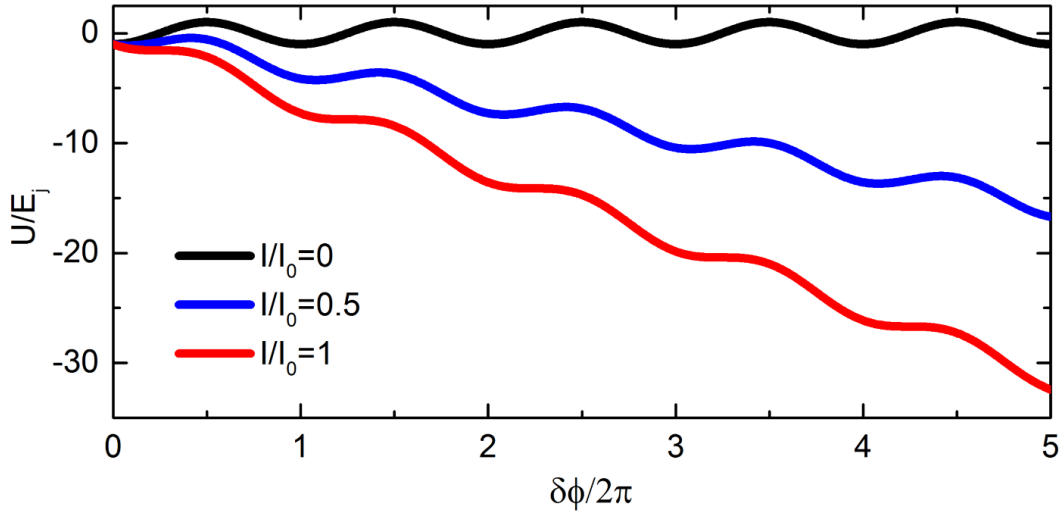
Figure 1.1: RCSJ potential energy at three different bias points, I/I_0. At zero bias, the phase is trapped in a local minimum. At $I/I_0 = 1$, the tilting of the washboard turns the local minima into inflection points, thus allowing the phase to roll and the junction enters its voltage state, $d\phi/dt = 2eV/\hbar$.

We can also define a dimensionless time variable $\tau = \omega_p t$, with $\omega_p = (2eI_o/\hbar C)^{1/2}$, so that the equation of motion can be re-written as:

$$I/I_0 = \sin\phi + \beta_c^{-1/2}\frac{d\phi}{d\tau} + \frac{d^2\phi}{d\tau^2}, \tag{1.12}$$

where,

$$\beta_c = \frac{2\pi R^2 C I_0}{\Phi_0}, \tag{1.13}$$

is the Stewart-McCumber parameter.

An intuitive insight can be gained by noting that the equation of motion of the phase particle, equation 1.12, is the equation of motion of a particle with mass, $(\Phi_0/2\pi)^2 C$, moving in a potential $U = -(\Phi_0 I_0/2\pi)\cos\phi - (\Phi_0 I/2\pi)\phi$, with a drag force $(\Phi_0/2\pi)^2(1/R)\ d\phi/dt$ representing the shunting resistance. Figure 1.1 plots this tilted washboard potential.

In the regime where $\beta_c < 1$, the junction is said to be overdamped and the IV is non-hysteretic. In the limit $\beta_c \ll 1$ and at $T = 0$ K, the IV characteristic is given by:
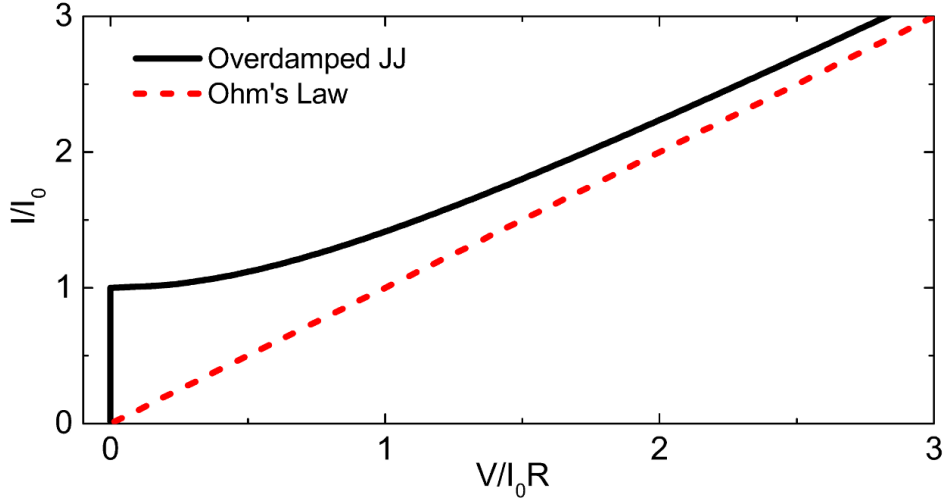
Figure 1.2: IV characteristics of an overdamped (resistively shunted) Josephson junction.

$$V = \begin{cases} 0 & I < I_0 \\ R(I^2 - I_0^2)^{1/2} & I \geq I_0 \end{cases} \tag{1.14}$$

In the regime $\beta_c \geq 1$ the junction is underdamped and the IV characteristic displays a hysteresis corresponding to the inertia of the phase particle. The bias current I acts to tilt the washboard potential and at $I = I_0$ the potential has been tilted so far as to make the local minima mere inflections, which then allows the phase particle to run freely, putting the junction in the voltage state. In the retrapping branch, the inertia of the phase particle allows it to escape the potential minima until the bias current has been sufficiently lowered to fully re-trap the phase particle.

1.3   The dc-SQUID

The dc-Superconducting Quantum Interference Device (SQUID) is formed by two Josephson junctions connected through a superconducting loop. The supercurrent through a SQUID inherits a Φ_0 periodic structure due to the fluxoid quantization in superconductors. This periodicity in magnetic flux makes the SQUID a very sensitive flux-to-voltage amplifier (trans-

(A)

(B)
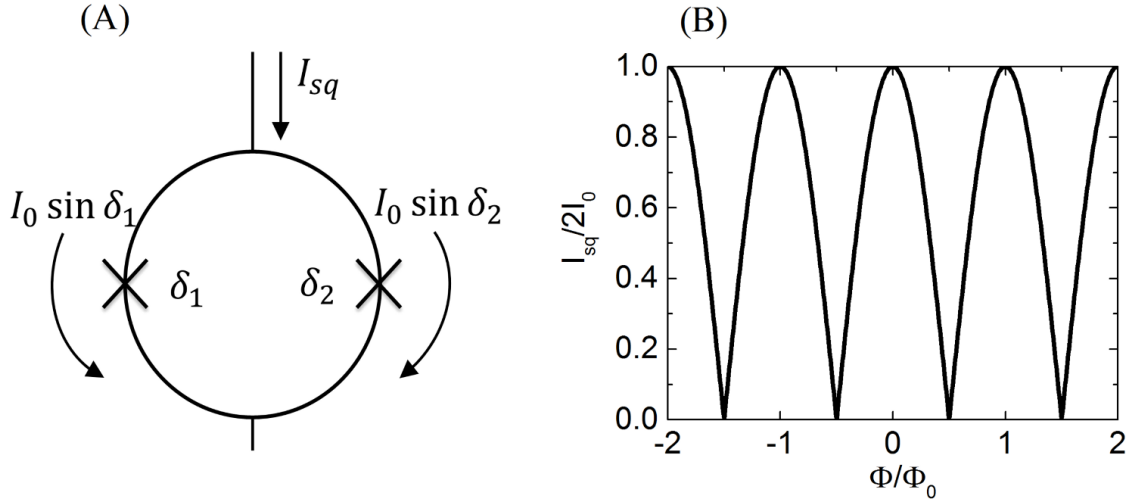
Figure 1.3: (A) Circuit diagram of a SQUID. (B) Modulation of the SQUID's critical current I_{sq} as a function of the magnetic flux Φ/Φ_0, $2I_0$ is the maximum critical current.

ducer). In a SQUID with symmetric junctions of critical current I_0, the total supercurrent I_{sq} is given by:

$$I_{sq} = I_0 \left(\sin \delta_1 + \sin \delta_2\right) = 2I_0 \sin\left(\frac{\delta_1 + \delta_2}{2}\right) \cos\left(\frac{\delta_1 - \delta_2}{2}\right) \tag{1.15}$$

The phase quantization condition for a SQUID is:

$$2\pi \frac{\Phi}{\Phi_0} = \delta_2 - \delta_1, \tag{1.16}$$

The total flux in the SQUID is the sum of the externally applied flux Φ_x and the flux generated by the circulating current I_q in the SQUID loop inductance L:

$$\Phi = \Phi_x + LI_q \tag{1.17}$$

If the loop inductance is small, such that the maximum flux contribution due to the circulating current is much smaller than the flux quantum, $2LI_0/\Phi_0 \ll 1$, then the SQUID supercurrent takes on the form:

$$I_{sq} = \left|2I_0 \cos\left(\pi \frac{\Phi_x}{\Phi_0}\right)\right| \sin\left(\frac{\delta_2 + \delta_1}{2}\right) \tag{1.18}$$

The SQUID screening parameter $\beta_L = 2I_0 L/\Phi_0$, is important when designing a SQUID. For $\beta_L \ll 1$ the SQUID supercurrent I_c^{SQ} modulates from its maximum $2I_0$ to 0. The modulation depth decreases as β_L is increased. When $\beta_L > 1$, more than one value of the circulating current is possible to satisfy the fluxoid quantization condition, leading to magnetic hysteresis.

1.4 Superconducting quantum bits

1.4.1 Model two level system

The simplest representation of the qubit is that of the hamiltonian of a pseudospin-1/2 system.

$$\mathbf{H} = \frac{1}{2}\left(\epsilon_z \hat{\sigma}_z + \epsilon_x \hat{\sigma}_x\right) \tag{1.19}$$

Labeling the eigenstates of the qubit $|0\rangle$ and $|1\rangle$, the generic state of the qubit takes on the form:

$$|\psi\rangle = \alpha|0\rangle + \beta|1\rangle, \tag{1.20}$$

with $|\alpha|^2 + |\beta|^2 = 1$. All the possible states of a qubit map out the surface of a sphere, commonly referred to as the Bloch sphere.

1.4.2 Superconducting flux qubit

The three energy terms relevant in the superconducting flux qubit are the charging energy, the Josephson energy, and the energy stored in the loop inductance by the circulating current:

$$\mathbf{H} = \frac{1}{2}C_J V^2 + \frac{1}{2}L_q I_q^2 - E_J \cos\phi \tag{1.21}$$

We can recast the Hamiltonian slightly in terms of some more physically accessible variables: the total flux is $\Phi = \Phi_x + \Phi_q$, where Φ_x is the externally applied flux, and Φ_q is the flux due
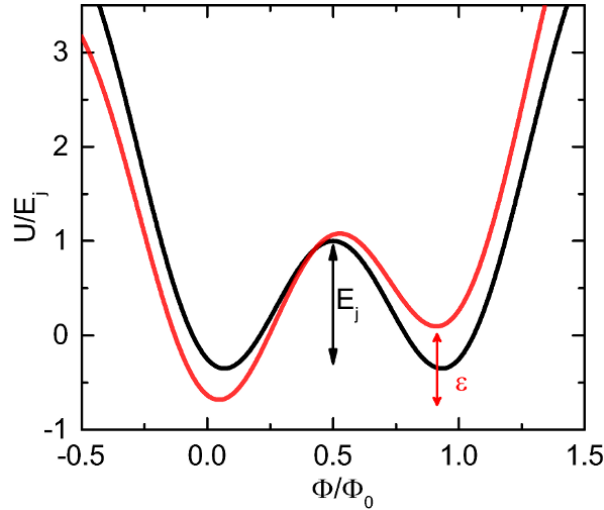
Figure 1.4: (Black line) Degenerate double well potential of a flux qubit biased at $\Phi_x = \Phi_0/2$. (Red line) Tilted double well potential away from the degeneracy point. E_J controls the height of the tunneling barrier. The magnetic flux bias controls ϵ which is the energy difference between the left/right wells.

to the circulating current given by $\Phi_q = L_q I_q$. Using the flux quantization condition:

$$2\pi \frac{\Phi}{\Phi_0} = \phi, \tag{1.22}$$

and denoting the single electron charging energy, $E_C = e^2/2C_J$, then the Hamiltonian can be re-expressed as:

$$\mathbf{H} = 4E_c \left(\frac{Q}{2e}\right)^2 + \frac{(\Phi - \Phi_x)^2}{2L_q} - E_J \cos\left(2\pi \frac{\Phi}{\Phi_0}\right), \tag{1.23}$$

By analogy to mechanical systems, the charging energy term can be seen as the kinetic energy, while the last two terms form the potential energy. At an external flux bias $\Phi_x = \Phi_0/2$ the flux qubit is biased at a special point called the degeneracy point. At this flux bias point, the quadratic inductive potential is at a minimum at the same point where the Josephson energy is at a maximum. This condition creates a double well potential as illustrated in figure 1.4.

The classic double well potential is formed where the potential barrier height is related to the Josephson energy E_J, which determines the tunnel coupling Δ_0 between the left and right wells. The energy asymmetry ϵ is controlled by the external flux bias Φ_x. The double-well

potential is degenerate, $\epsilon = 0$, when $\Phi_x = \Phi_0/2$. The qubit energy is given by:

$$E_{01} = \sqrt{\Delta_0^2 + \epsilon^2} \tag{1.24}$$

In the localized left/right well basis, the qubit eigenstates $|0\rangle$ and $|1\rangle$ at the degeneracy point are the symmetric and anti-symmetric combinations:

$$|0\rangle = \frac{|L\rangle + |R\rangle}{\sqrt{2}} \tag{1.25}$$

$$|1\rangle = \frac{|L\rangle - |R\rangle}{\sqrt{2}}, \tag{1.26}$$

separated by an energy $E_{01} = \Delta_0$ where Δ_0 is the tunnel coupling strength controlled by the height of the barrier, which is in turn dependent on the critical current I_c of the Josephson junction forming the qubit. Hence fluctuations in the critical current will manifest as fluctuations in the qubit frequency, $f_{01} = E_{01}/h$

1.4.3 Phase qubit

An earlier superconducting qubit architecture is the current-biased phase qubit. It makes use of the tilted-washboard potential of the Josephson junction (figure 1.1), where the current bias is tuned so that the local potential well contains three bound states used to realize the logical qubit states and a readout state. Consequently the qubit is highly sensitive to noise coupled in through this external current biasing line. A modern incarnation of the phase qubit places the Josephson junction in a superconducting loop, so that the current bias can be achieved through an external magnetic flux bias. Nevertheless, the Hamiltonian of the current biased phase qubit still serves as a prototypical example of how the Hamiltonian of the Josephson junction system can be engineered to realize a quantum bit.

The potential energy in the current biased phase qubit is essentially the current biased/tilted

washboard potential, hence has the Hamiltonian:

$$\mathbf{H} = \frac{Q^2}{2C_J} - E_j \cos\phi - \left(\frac{\Phi_0 I}{2\pi}\right)\phi \qquad (1.27)$$

For current biases $I \approx I_0$, the potential well confining the phase particle is shallow, and it is possible to choose the correct bias parameters such that there are only three discrete states in the local minima. The first two states $|0\rangle$ and $|1\rangle$ form the logical qubit states, while the third $|3\rangle$ serves as a read-out state. Since the local minima arises due to the cosine dependence of the Josephson energy ($E_J = E_{J0}\cos\phi$), fluctuations in the Josephson energy lead to perturbations in the qubit states and eigenenergies.

The Hamiltonian of the flux biased phase qubit is identical to that of the flux qubit, the differences in operation comes from the choice of circuit parameters. As such the potential energy for the phase qubit is identical to figure 1.4. In the phase qubit the double well potential is extremely tilted to one side, such that one of the localized potential well is so shallow that it only supports about 3 discrete energy levels. The opposite well is now deep enough to contain many energy states that it can be treated as essentially a continuum of energy states that will serve as the readout states. Again in this architecture the Josephson energy E_J is the term that gives rise to the localizing potential, thus fluctuations in I_0 can perturb the qubit frequency.

1.5   Fluctuations

Due to some fundamental physical processes, a physical quantity $x(t)$ can fluctuate around its mean value $\langle x \rangle$. For example, Brownian motion is the fluctuation on the spatial coordinates $\mathbf{r}(t)$ of particles suspended in a liquid. In the case of Brownian motion, the cause of this fluctuation turns out to be the thermal motion of the molecules comprising the liquid. To be able to deduce the physical processes responsible for fluctuations, it is imperative that we understand how we can describe these fluctuations.

We can assign a probability density function, $w(x,t)$ to a physical variable $x(t)$. The probability that at time t the variable x takes on the value in the range of $x_0 \leq x \leq x_1$, is given by:

$$P(x_0 \leq x \leq x_1, t) = \int_{x_0}^{x_1} w(x,t) \, dx \tag{1.28}$$

The variable $x(t)$ is said to be *stationary* if the probability density function independent of time, so that: $w(x,t) = w(x)$. The mean and mean square values are defined in the usual way:

$$\langle x \rangle = \int_{-\infty}^{+\infty} x \, w(x) \, dx, \tag{1.29}$$

$$\langle x^2 \rangle = \int_{-\infty}^{+\infty} x^2 \, w(x) \, dx, \tag{1.30}$$

We define fluctuations in the variable $x(t)$ to be deviations from the mean:

$$\delta x(t) = x(t) - \langle x \rangle, \tag{1.31}$$

and the variance σ^2 is defined as the mean value of the fluctuation squared:

$$\sigma^2 = \langle \delta x^2 \rangle = \langle (x - \langle x \rangle)^2 \rangle = \langle x^2 \rangle - \langle x \rangle^2 \tag{1.32}$$

An important class of fluctuations is when the physical quantity $x(t)$ takes on values that are distributed according to the normal (Gaussian) distribution:

$$w(x) = \frac{1}{\sqrt{2\pi\sigma^2}} \exp\left(-\frac{(\delta x)^2}{2\sigma^2}\right) \tag{1.33}$$

An extreme case of non-Gaussian distribution, one that is central to this thesis, is the case of a random telegraph signal, or a two level system. In this case the variable $x(t)$, usually either voltage $V(t)$ or the resistance $R(t)$, takes on only two discrete values x_1 and x_2, instead of the continuous range of values required for the Gaussian distribution. However the superposition of many ($N \gg 1$) and independent two level systems can sum to fluctuations that are normally

(Gaussian) distributed, a manifestation of the central limit theorem.

To describe how the fluctuations $\delta x(t)$ evolve in time, we invoke the correlation function:

$$\psi(\tau) = \langle \delta x(t+\tau)\delta x(t)\rangle = \int_{-\infty}^{+\infty} \delta x(t+\tau) \; \delta x(t) \; dt \tag{1.34}$$

The correlator $\psi(\tau)$ measures how similar the signal $x(t)$ is to itself at a time offset τ (autocorrelator), it therefore reveals the time evolution of the fluctuations. In our analysis it is often useful to analyze the spectral content of the fluctuations. The Wiener-Khintchine theorem links the Fourier transform of the autocorrelator to the power spectral density, $S_x(f)$, of the signal $x(t)$:

$$S_x(f) = \int \psi(\tau) \; e^{-2\pi i f \tau} \; d\tau \tag{1.35}$$

A random process is said to be *Gaussian* if its statistics is fully described by its power spectral density, therefore equivalently its 2-point correlation functions $\psi(t_1, t_2)$. That is any higher order n-point correlation functions do not contain information that is not already in the 2-point correlations.

The spectral information contained in the power spectral density can reveal important characteristics of the fundamental physical processes that drive the fluctuations under study. One canonical example is the thermal noise of electrons in a resistor, commonly referred to as the Johnson-Nyquist noise. The thermal excitations of electrons in a resistor give rise to finite voltage fluctuations, even at zero voltage bias. While the instantaneous voltage fluctuates from zero, the average voltage is of course zero. The power spectral density of the thermal voltage fluctuations is a constant (white noise), given by:

$$S_V = 4k_B T R, \tag{1.36}$$

or in terms of current noise:

$$S_I = \frac{4k_B T}{R}, \tag{1.37}$$

where k_B is the Boltzmann constant.

CHAPTER 2

THE CRITICAL CURRENT NOISE PROBLEM IN QUANTUM BITS

2.1 Qubit Coherence
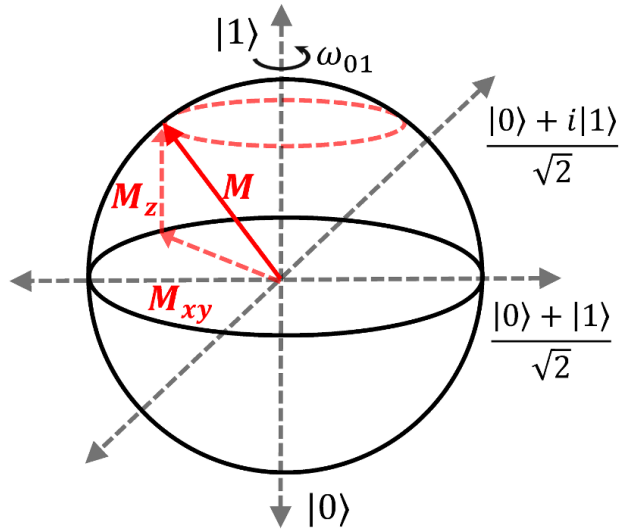
Figure 2.1: The Bloch sphere. The qubit state $|\psi\rangle$ is represented by the Bloch vector $\mathbf{M}$, with components M_z and M_{xy} is the vector component in the xy-plane.

A qubit can be described by the Hamiltonian of a spin-$\frac{1}{2}$ particle in a magnetic field:

$$\mathbf{H} = \frac{1}{2}E_{01}\hat{\sigma}_z, \tag{2.1}$$

with the energy eigenstates $|0\rangle$ and $|1\rangle$, and E_{01} is the qubit energy. The general qubit state is then the superposition, $|\psi\rangle = \alpha|0\rangle + \beta|1\rangle$, with the normalization $|\alpha|^2 + |\beta|^2 = 1$.

The qubit state vector $|\psi\rangle$ can be thought of as mapping the surface of a sphere of unit

radius, called the Bloch sphere (figure 2.1). Each possible state of the qubit corresponds to a point on the surface of the Bloch sphere, represented by the Bloch vector $\mathbf{M}$. The time evolution (Schrödinger equation) of the Bloch vector turns out to be the precession about the $\hat{z}$-axis with frequency $\omega_{01} = E_{01}/\hbar$. To manipulate the qubit, microwave pulses are applied in the $\hat{x}$ (or $\hat{y}$) axis which will act to rotate the Bloch vector.

2.1.1 T_1 - energy relaxation

If the qubit is able to exchange energy with an external bath of oscillators, then the information encoded in the qubit is no longer preserved. In energy relaxation processes typically the qubit loses its energy and decays into the ground state (it can also be excited and gain energy from the environment, in either case the energy stored in the qubit is no longer controlled, thus the information encoded is essentially lost). A qubit prepared in the excited state $|1\rangle$ will decay into the ground state $|0\rangle$ over a characteristic energy relaxation time T_1, where the probability $P_1(t)$ for finding the qubit in the excited state is given by:

$$P_1(t) = e^{-t/\tau_1} \tag{2.2}$$

2.1.2 T_2^* free induction decay

In free induction decay, the qubit interaction with the external bath does not involve energy exchange. Instead the interaction results in fluctuations in the qubit frequency, which can be thought of as a spectral broadening $\delta\omega_{01}$ of the qubit frequency ω_{01}. At some time t the qubit should gain a phase $\phi(t) = \omega_{01}t$, but in the presence of a random fluctuation $\delta\omega_{01}$, the phase of the qubit is given by $\phi(t) = \omega_{01}t + \delta\phi(t)$, where $\delta\phi(t) = \int_0^t \delta\omega_{01}(t)\ dt$ is the random phase fluctuation.

The problem with this random phase accumulation (dephasing) is that in a qubit measurement the state vector can only be reconstructed after the averaging of many projective measurements ($\sim 10^3$). The xy-component of the Bloch vector is given by $M_{xy}(t) = e^{i\phi(t)}M_{xy}(0)$,

therefore the result of the averaging at time t contains the averaging over the random fluc-
tuation of the environment, $\langle M_{xy}(t) \rangle \propto \langle e^{i\delta\phi(t)} \rangle$, which results in an exponential decay enve-
lope [48]:

$$\langle e^{i\delta\phi(t)} \rangle = e^{-t/T_2^*}, \tag{2.3}$$

where T_2^* is the characteristic timescale for qubit dephasing, called the free induction decay
time.

An important result well known from NMR is that the dephasing rate $1/T_2^*$ is the sum of
the contributions from energy relaxation (energy loss is ultimately a dephasing event) and the
sum of the pure dephasing rate from others sources [12]:

$$\frac{1}{T_2^*} = \frac{1}{2T_1} + \sum_n \frac{1}{\tau_{\phi,n}} \tag{2.4}$$

2.2   Dephasing from critical current noise

The details of how fluctuations in the junction critical current appear as the spectral broadening
of the qubit frequency ω_{01} depends on the particular superconducting qubit architecture. In
the simplest form, the superconducting qubit can be thought of as a quantum LC circuit with
frequency $\omega_{01} = 1/\sqrt{LC}$, where in the case of a transmon [37, 29, 61] the inductance is provided
by the Josephson inductance L_J. The qubit frequency is thus:

$$\omega_{01} = \frac{1}{\sqrt{L_J C}} = \sqrt{8E_J E_C} \tag{2.5}$$

The spectral broadening due to I_c fluctuation is thus: $d\omega_{01}/dI_c = (\hbar/2e)\sqrt{2E_c/E_J}$. To quan-
tify the different I_c sensitivity in the various superconducting qubit architectures, the dimen-
sionless factor $\Lambda = (I_c/\omega_{01})|d\omega_{01}/dI_c|$ was introduced by Van Harlingen et. al. [67]. For

example the transmon sensitivity to critical current fluctuation is then given by:

$$\Lambda = \frac{I_c}{\omega_{01}} \left| \frac{d\omega_{01}}{dI_c} \right| = \frac{1}{2} \tag{2.6}$$

For other SC qubit architectures the sensitivity Λ in general cannot be found analytically, necessitating a numerical solution. For example in the flux qubit the Josephson energy E_J determines the tunnel coupling strength Δ_0 between the left and right circulating current states, where at degeneracy, $\omega_{01} \approx \Delta_0/\hbar$. The calculation in Van Harlingen et. al. [67] gives $\Lambda \approx 12.3$ for the 3-JJ flux qubit architecture.

2.3   State of the field and open questions in critical current noise

The problem of critical current noise used to be discussed in terms of its contribution to the pure dephasing of a qubit. The focus was the quantification of the $1/f$ noise magnitude at temperatures typical of the operating point for qubits, and the effect of this $1/f$ noise on the timescale for qubit dephasing. Ultimately measurements of the critical current noise at $T \approx 50$ mK (typical qubit operating temperatures) proved difficult as most measurements of the critical current noise involves some finite dissipation (chapter 5.2). With a wealth of pre-existing measurements in the temperature range $T \approx 1.4 - 4.2$ K [60, 67, 77], a number of experiments [18, 53] surfaced that focused on the functional form of the temperature dependence, which would then be used to infer the $1/f$ noise magnitude for the typical qubit operation.

One point of contention is the form of the temperature dependence for the power spectral density. There appeared to be evidence for two very different conclusions, a handful of experiments [77, 14, 67] observed and concluded a T^2 dependence, while another set of experiments concluded a linear T-dependence [53, 18]. The T^2 observing experiments were mostly from older experiments in the 1980s and 1990s which were available at the time of the survey of Van Harlingen et. al. [67], that found the critical current noise power spectral density to have

a nearly universal value described by:

$$\frac{S_{I_c}}{I_c^2} = 1.44 \times 10^{-10} \left(\frac{1}{f}\right) \left(\frac{1}{A/\mu m^2}\right) \left(\frac{T}{4.2 \text{ K}}\right)^2 \text{ Hz}^{-1} \tag{2.7}$$

The observation of the T^2 dependence was the most striking, as at low temperatures ($T \sim 1$ K) the noise power is expected to vary linearly in T, similar to that found in the low temperature specific heat capacity of glasses [51, 82]. At low temperatures the thermally activated rates of the TLSs should freeze-out, and the TLS dynamics are governed by the quantum tunneling through the double-well potential of the TLS [51]. This leaves only a linear T-factor coming from the thermodynamic selection of those TLSs with energies $E \lesssim kT$ (section 3.2). Yet, the T^2 dependence is not without precedent, the charge noise in single electron transistors (SETs) have previously been measured to have a T^2 dependence [6], and the noise power from thermally activated TLSs in the classic Dutta-Horn model is expected to have a T^2 dependence, although the assumption of thermally activated rates at low temperatures ($T \sim 1$ K) is problematic [74].

The T- and T^2-dependence discrepancy led to the development of the Kondo-like traps theory, primarily by Ioffe and Faoro [19, 20, 21], and Wilhelm [3]. These theories pointed out that measurements producing a T^2-dependence have been carried out when the metal electrodes are kept superconducting [14, 78], and observed a much higher noise magnitude (at $T = 4.2$ K). While the observation of a linear T-dependence was obtained on experiments measuring the tunneling resistance with the metal electrodes in the normal state [18], and the critical current noise was deduced assuming the equivalency of critical-current noise and tunneling resistance noise, $S_{I_c}/I_c^2 \equiv S_R/R^2$. This equivalency is justified via the Ambegaokar-Baratoff relationship, $I_0 R_n = \pi\Delta/2e$, but only when provided that there is no additional noise mechanism. Some electronic traps at the metal-dielectric interface can have a strong on-site repulsion that allows only single occupancy of the trap. It was then proposed that the interaction of these traps with the conduction electrons in the metal electrodes lead to the well known Kondo physics, where the trapped electron interact with the conduction electrons to form a spin zero singlet ground state, $|\psi_g\rangle = (|\uparrow\downarrow\rangle + |\downarrow\uparrow\rangle)/\sqrt{2}$, characterized by an energy scale T_K (the Kondo temperature).

When superconductivity develops in the metal electrodes, a superconducting ground state is formed with characteristic energy Δ, the superconducting energy gap. It was proposed that for these traps at the metal-dielectric interface, the competition between the Kondo interaction and superconductivity leads to the formation of additional localized trap states [3, 19, 20, 21], that can account for the T^2-dependence and the increased noise magnitude.

Critically however there exist contradictions on the available experimental data that would cast doubt on the necessity of a Kondo-traps theory. Rogers and Buhrman [54] reported in 1983 of measurements of the critical current noise in a shunted Nb-PbBi edge junction, and measurements of the tunneling resistance in the same junction by measuring above the superconducting energy gap. Their result supported the equivalency $S_{I_c}/I_c^2 = S_R/R^2$ which at the very least implies that the Kondo-traps contribution was negligible. More recently the measurements of Pottorf et. al. [53] of the critical current noise in shunted Nb/AlO$_x$/Nb junctions showed a linear T-dependence, with a magnitude consistent with other measurements of the tunneling resistance noise [18]. This result implies that the critical-current and tunneling resistance noise equivalency holds, $S_{I_c}/I_c^2 \equiv S_R/R^2$. Furthermore Pottorf et. al. [53] performed measurements of the tunneling resistance noise in their unshunted Nb/AlO$_x$/Nb junctions and observed the same linear T-dependence and noise magnitude as in their measurements of the critical current noise, supporting the S_{I_c} and S_R equivalency.

This contradictory state of the available experimental data led to our motivation for the measurements of the critical current and resistance noise in Al/AlO$_x$/Al junctions (first half of chapter 6). It should be added that our own measurements agreed with the linear T-dependence and confirms the equivalency of S_{I_c} and S_R.

2.3.1 I_c noise in zero-voltage and finite-voltage state

Another detail of critical current noise is the question of whether or not the fluctuations are identical in both the zero-voltage and finite-voltage states. In measurements of the critical current using the SQUID potentiometry method (section 5.2), the junction is biased out into

a non-zero voltage state, typically $V \approx 1 - 5~\mu$V. Qubit operations on the other leaves the junctions in the zero-voltage state, which raised the question of whether or not $1/f$ noise measurements in the finite voltage state are applicable to qubits. This question mirrors that from $1/f$ noise in resistors some four decades ago, over the question of whether or not the $1/f$ noise is an equilibrium fluctuation [74]. In that case Voss and Clarke [71] measured the resistance fluctuation at zero applied current by measuring fluctuations in the Johnson noise of a resistor. It was found that the resistance fluctuation at zero applied current is equal to that at finite currents.

The $1/f$ noise in tunnel junctions was also found to be an equilibrium fluctuation. Mück et. al. [44] measured the I_c noise in the zero voltage state by performing a dispersive readout of a rf-SQUID with a Nb-trilayer junction. The measured critical current noise was approximately $S_{I_c}/I_c^2 = 6.8 \times 10^{-11}$ Hz^{-1}, which is consistent with the old universal value $S_{I_c}/I_c^2 \approx 3.6 \times 10^{-11}$ Hz^{-1} (at $T = 4.2$ K) (equation 2.7).

More recent measurements by Murch et. al. [45] measured the critical current fluctuations in Al double angle junctions embedded in lumped-element microwave resonators. In this measurement the Josephson inductance $L_J(I_c) = \Phi_0/2\pi I_c$ contributes to the resonator total inductance $L(I_c) = L_0 + L_J(I_c)$, where L_0 is the lumped element inductance of the resonator. The resonant frequency of the resonator is then dependent on the critical current of the junction: $\omega_0(I_c) = 1/\sqrt{L(I_c)C}$, where C is the lumped-element capacitance forming the resonator. Fluctuations in the resonant frequency is therefore related to fluctuations in the critical current of the junction via: $S_\omega/\omega_0^2 = (p^2/4)S_{I_c}/I_c^2$, where $p = L_{J0}/L$ is the participation ratio of the Josephson inductance to the total resonator inductance. Interestingly their measurements at $T = 50$ mK were not able to measure the low frequency noise due to the junctions, above the level of the background noise. This places a limit of $S_{I_c}/I_c^2 < 1 \times 10^{-16}$ Hz^{-1} for the critical current noise at 50 mK, which is at least a factor of 400 lower than the value predicted by the old universal formula (equation 2.7)

There is potentially a contradiction between the results of Mück et.al. [44] and Murch et.

al. [45]. While Mück et. al. supported the equivalency of the zero-voltage and finite-voltage noise, the results of Murch. et. al. taken in isolation can be interpreted as a contradiction to that equivalency. The results of our own experiments in chapter 6 provides the final link to resolve this contradiction.

2.3.2   Nature of the fluctuator: electronic or atomic?

It has been known that the origin of the $1/f$ critical current noise is an ensemble of two level systems (TLSs) that modulate the transmissivity of the tunnel barrier [73, 72, 58]. What remains unresolved is a definite identification of the microscopic origin of the TLSs, though it is accepted that they are either fluctuating electrons or atoms.

The experiments of Wakai et. al. [72, 73] on PbInAu-In$_2$O$_3$-Pb junctions concluded that the fluctuator is the trapping and un-trapping of electrons at the junction metal-dielectric interfaces. Similar experiments by Rogers and Buhrman [56, 58] on Nb-Nb$_2$O$_5$-PbBi concluded that the TLS is a fluctuating atomic dipole. It may be important to resolve the microscopic nature of the TLSs, as different microscopic sources may suggest vastly different strategies for eliminating these TLSs.

More recent experiments, most notably in phase qubits [43], the energy spectroscopy of qubits typically contains a density of parasitic avoided level crossings caused by the coherent interaction with two level defects. It is not immediately clear if the two level systems coupling at qubit frequencies represent the same ensemble that produce the low frequency $1/f$ noise. But if they did, then it casts doubt on the electronic trapping model of Wakai et. al. [72], where the fluctuator is modelled as the trapping/emptying of an electronic trap by the tunneling of electrons from the degenerate metal electrodes. A TLS model involving the tunneling to a degenerate fermi sea, like a metallic electrode, is incompatible with the observation that the two level systems are coherent. Coherent dynamics is most readily obtained in a localized TLS model, such as the double-well potential model (tunneling TLS). Note that this includes the possibility for the fluctuator to be an electron, although we will argue that an atom fits the data

better. In fact Lisenfeld et. al [39] directly measured the coherence properties of a TLS coupled to a phase qubit, and measured a coherent TLS with $T_1 \approx 400$ ns and $T_2 \approx 800$ ns $\approx 2T_1$, which in fact exceeded the coherence times of the phase qubit used to measure the TLSs ($T_1^{\text{qubit}} \approx 100$ ns).

CHAPTER 3

THEORETICAL DESCRIPTION OF $1/F$ NOISE AND TWO LEVEL SYSTEMS

3.1 $1/f$ noise

The subject of low frequency $1/f$ noise has had a rich and extensive history. It turns out that the fluctuations in a wide range of physical systems can have a power spectral density that varies as $1/f^\alpha$, with the exponent typically $\alpha \sim 0.8 - 1.2$ [74]. For example carrier density fluctuations can lead to a $1/f$ resistance noise in MOSFETs [84], resistance fluctuations in CuMn thin films due to spin fluctuations [30], and magnetic flux noise in SQUIDs [63]. In non solid-state systems, Voss and Clarke [70] have showed that even the "loudness" (amplitude fluctuations) in speech and music can have a $1/f$ power spectrum, and even the historical levels of the Nile river from the year $662 - 1469$ has been shown to produce a $1/f$ power spectrum [41].

It was realized that a $1/f^\alpha$ spectrum can be constructed from the sum of Lorentzian power spectra with a widely distributed characteristic frequencies [83]. Each Lorentzian contributes a power spectral density given by:

$$S_i(\omega) \propto \frac{\tau_i}{1 + \omega^2 \tau_i^2},\tag{3.1}$$

with a characteristic lifetime τ_i. The total noise power due to a distribution of these Lorentzians is then:

$$S(\omega) \propto \int \frac{\tau}{1 + \omega^2 \tau^2} \, D(\tau) \, d\tau \tag{3.2}$$

Consequently if the characteristic times are distributed as, $D(\tau) \propto 1/\tau$, then the total noise

power density is $1/f$, $S(\omega) \propto 1/\omega$.

3.2   The Dutta-Horn Model
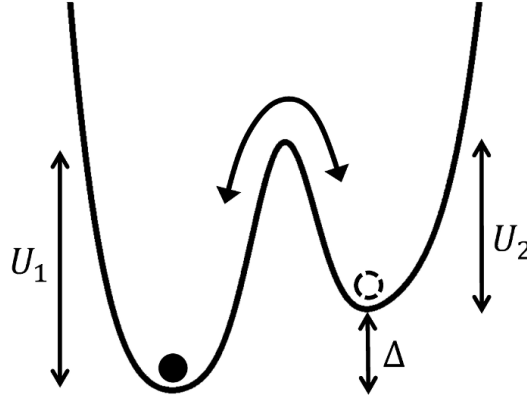
Figure 3.1: Thermally activated double-well two level system. A particle in the well can make a transition to the other well if there is sufficient thermal energy to overcome the potential barrier U_i.

In the Dutta-Horn model, the source of the Lorentzian is modeled as a thermally activated fluctuator in a double-well potential. The TLS can be described in terms of the average of the potential barrier in the left/right wells, $U = (U_1 + U_2)/2$, and the energy difference of the left/right wells (asymmetry) Δ, (figure 3.1). In this way the transition rates out of the wells are given by:

$$\omega_1 = \omega_0 \exp\left(-\frac{U + \Delta/2}{kT}\right) \tag{3.3}$$

$$\omega_2 = \omega_0 \exp\left(-\frac{U - \Delta/2}{kT}\right) \tag{3.4}$$

The TLS corner frequency is then given by:

$$\omega_c = \omega_1 + \omega_2 = \omega_0^* \exp\left(-\frac{U}{kT}\right) \cosh\left(\frac{\Delta}{2kT}\right), \tag{3.5}$$

where $\omega_0^* = 2\omega_0$, and as long as $\Delta < 2kT$, then we recover the Arrhenius thermally activated

rate for ω_c:

$$1/\tau = \omega_c \approx \omega_0^* \exp\left(-U/kT\right) \tag{3.6}$$

In a physical system there will be a distribution of these TLSs with respect to the energies U and Δ, where the typical starting assumption is the uniform (flat)joint distribution:

$$P(U,\Delta)\ dUd\Delta = P_0\ dUd\Delta, \tag{3.7}$$

however only those TLSs with $\Delta \lesssim 2kT$ will have enough variance to contribute to the total noise power.

If we label the TLS's probability to be in the left/right well as p_L and p_R respectively, then: $p_L + p_R = 1$ and $p_R/p_L = \exp\left(-\Delta/kT\right)$. If for example the TLS couples into the junction's tunneling resistance so that it changes by an amount δR between the TLS in the left/right wells, then the variance due to the TLS can be calculated as: $\sigma_R^2 = \langle R^2 \rangle - \langle R \rangle^2 = \delta R^2 p_R p_L = \delta R^2 \mathrm{sech}^2\left(\Delta/2kT\right)/4$. The Lorentzian spectral density contributed due to the i-th TLS is therefore weighted by this thermodynamic factor [74, 38]:

$$S_i(\omega) = (\delta R)^2 \mathrm{sech}^2(\Delta/2kT)\frac{\tau_i}{1+\omega^2\tau_i^2} \tag{3.8}$$

Thus only those TLSs with $\Delta \lesssim 2kT$ will have enough variance to contribute to the total noise power. The TLS distribution in the energy U can then be expressed as:

$$P(U) = \int_{-\infty}^{+\infty} P(U,\Delta)\mathrm{sech}^2(\Delta/2kT)\ d\Delta \approx 4kTP_0, \tag{3.9}$$

where the integral is essentially selecting only those TLSs that will thermodynamically contribute to the total noise power spectral density. Consequently the TLS lifetime distribution in the Dutta-Horn model is:

$$P(\tau)\ d\tau \approx 4(kT)^2 P_0 \frac{d\tau}{\tau}, \tag{3.10}$$

where the additional factor of kT comes from the Dutta-Horn activated kinetics. The integrated power spectral density for the ensemble of TLSs is then:

$$S(\omega) \propto \int \frac{\tau}{1 + \omega^2 \tau^2} \frac{4P_0 (kT)^2}{\tau} \, d\tau \tag{3.11}$$

$$S(\omega) \propto 4P_0 (kT)^2 \left(\frac{1}{\omega} \right), \tag{3.12}$$

which gives a $1/f$ power spectral density that varies with T^2. One T-factor comes from the Dutta-Horn activated kinetics, and the second T-factor comes from the $\operatorname{sech}^2(\Delta/2kT)$ thermodynamic factor.

In fact for the generic $1/f^\alpha$ noise with $0.8 < \alpha < 1.4$, it is only required that the density of states $P(E)$ is *slowly varying* compared to $k_B T$. Dutta and Horn [17] noted that for thermally activated processes the total power spectral density is obtained from the integral:

$$S(\omega, T) \propto \int \frac{\tau_0 \exp(E/kT)}{1 + \omega^2 \tau_0^2 \exp(2E/kT)} P(E) \, dE \tag{3.13}$$

If the integration is carried out after Taylor expanding $P(E)$, then retaining only the first term, the power spectral density is approximately:

$$S(\omega, T) \propto \frac{k_B T}{\omega} P(\tilde{E}), \tag{3.14}$$

where here only the Dutta-Horn activated kinetic T-factor has been explicitly shown, and $\tilde{E} = -k_B T \ln(\omega \tau_0)$ is the value of E where the distribution $P(E)$ is peaked at. A consequence of $P(E)$ to be only slowly varying, is that the shape of the power spectral density is a more complicated function of ω and T, summarized by the relationship [17]:

$$\alpha(\omega, T) = 1 - \frac{1}{\ln(\omega \tau_0)} \left[\frac{\partial \ln S(\omega, T)}{\partial \ln T} - 1 \right], \tag{3.15}$$

where $\alpha(\omega, T)$ is the slope (exponent) of the $1/f^\alpha$ power spectrum defined locally at frequency

ω and temperature T.

3.2.1   Tunneling TLSs
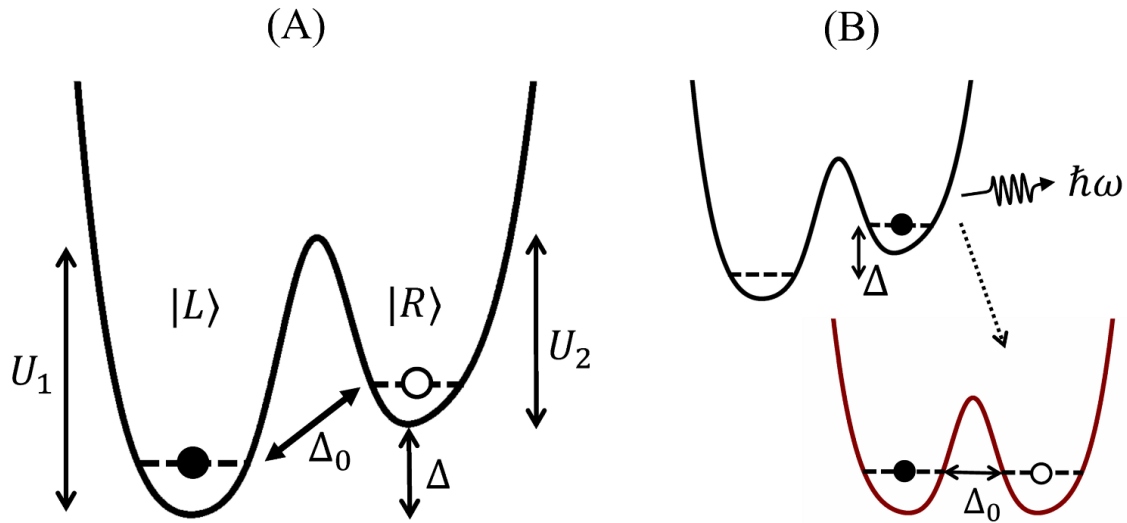
Figure 3.2: (A) Potential diagram of the tunneling TLS model. (B) Absorption/emission of a phonon modifies the TLS asymmetry energy Δ.

One concern with the thermal activation model is that at low temperatures there might not be enough thermal energy to drive the TLS transitions. However, for temperatures $kT < U$, the tunnel coupling between the two localized well states may become important. This tunneling TLS model was first proposed by Anderson, Halperin, and Varma [2], and independently by Phillips [50], in order to explain the anomalous thermal conductivity and heat capacity of insulating glasses. Subsequently it was realized that these tunneling TLSs can also give rise to a wide distribution of lifetimes τ, thus a $1/f$ power spectral density [81].

Figure 3.2 shows a schematic of the double-well potential annotated with the relevant energy scales in the tunneling regime. In insulating glasses TLS state transitions are driven by the absoprtion/emission of phonons, which couple to the TLS asymmetry energy Δ, (figure 3.2B). In metallic systems the transitions can also be driven by coupling to the electrons. As will be discussed in chapter 7, TLSs embedded in the dielectric of a tunnel junction may be driven by

both the phonon and electron excitations.

In the localized basis, $|L\rangle$ and $|R\rangle$, the model Hamiltonian for the tunneling TLS is:

$$\hat{H} = \frac{1}{2}\left(\Delta\hat{\sigma}_z + \Delta_0\hat{\sigma}_x\right), \tag{3.16}$$

Where Δ is the energy difference between the left and right wells, and Δ_0 is the tunnel coupling strength between the two wells. Δ_0 can be estimated via the WKB approximation:

$$\Delta_0 = \hbar\omega_0 \exp\left(-2d\sqrt{\frac{2mU}{\hbar^2}}\right), \tag{3.17}$$

where ω_0 is the attempt frequency of the particle in the potential well, m is the tunneling particle effective mass, U is the barrier height, and d is the tunneling distance.

By defining:

$$\tan\xi = \frac{\Delta_0}{\Delta}, \tag{3.18}$$

The TLS hamiltonian (equation 3.16) takes the form:

$$H = \frac{1}{2}\sqrt{\Delta^2 + \Delta_0^2}\begin{pmatrix} \cos\xi & \sin\xi \\ \sin\xi & -\cos\xi \end{pmatrix} \tag{3.19}$$

The TLS energy is then given by:

$$E = \sqrt{\Delta^2 + \Delta_0^2}, \tag{3.20}$$

and the eigenstates $|\psi_1\rangle$ and $|\psi_2\rangle$ of the TLS are:

$$|\psi_1\rangle = \cos\frac{\xi}{2}|L\rangle + \sin\frac{\xi}{2}|R\rangle \tag{3.21}$$

$$|\psi_2\rangle = \sin\frac{\xi}{2}|L\rangle - \cos\frac{\xi}{2}|R\rangle \tag{3.22}$$

At degeneracy, $\Delta = 0$ so that $\xi = \pi/2$, then the eigenstates are the usual symmetric/anti-

symmetric combinations:

$$|\psi_{1,2}\rangle = \frac{1}{\sqrt{2}}\Big(|L\rangle \pm |R\rangle\Big), \tag{3.23}$$

In the limit where the tunnel coupling is small $\Delta_0 \ll \Delta$ ($\xi \approx 0$), the TLS Hamiltonian is diagonal in the local representation, and the eigenstates are the localized states: $|\psi_1\rangle = |L\rangle$ and $|\psi_2\rangle = |R\rangle$.

In bulk (3D) dielectrics the TLS relaxation rate due to interaction with the strain field (phonons) can be shown to be [51]:

$$\Gamma_{ge} = \left(\sum_\alpha \frac{\gamma_\alpha^2}{v_\alpha^5}\right)\left(\frac{E\Delta_0^2}{2\pi\rho\hbar^4}\right)\frac{1}{\exp\left(E/k_BT\right)-1} \tag{3.24}$$

$$\Gamma_{eg} = \left(\sum_\alpha \frac{\gamma_\alpha^2}{v_\alpha^5}\right)\left(\frac{E\Delta_0^2}{2\pi\rho\hbar^4}\right)\frac{1}{1-\exp\left(-E/k_BT\right)}, \tag{3.25}$$

where γ_α and v_α are the elastic dipole and velocity of sound for the α polarization, and ρ is the mass density. The effective rate is then:

$$\tau^{-1}(E,\Delta_0) = \Gamma = \Gamma_{ge} + \Gamma_{eg} = \left(\sum_\alpha \frac{\gamma_\alpha^2}{v_\alpha^5}\right)\left(\frac{E\Delta_0^2}{2\pi\rho\hbar^4}\right)\coth\left(\frac{E}{2k_BT}\right) \tag{3.26}$$

In a typical physical system the TLSs are assumed to be uniformly distributed in the asymmetry energy Δ and the WKB tunneling parameter λ. Since $\Delta_0 \propto e^{-\lambda}$, the joint TLS distribution is then:

$$P(\Delta,\lambda)\, d\Delta\, d\lambda = P_0\, d\Delta\, d\lambda \tag{3.27}$$

$$P(\Delta,\Delta_0)\, d\Delta\, d\Delta_0 = \frac{P_0}{\Delta_0}\, d\Delta\, d\Delta_0 \tag{3.28}$$

The total power spectral density due to fluctuating tunneling TLSs can then be calculated from the integral:

$$S(\omega) \propto \int \frac{\tau(\Delta,\Delta_0)}{1+\omega^2\tau^2(\Delta,\Delta_0)}\, P(\Delta,\Delta_0)\, d\Delta\, d\Delta_0 \tag{3.29}$$

Note that in the tunneling TLS model, the T-dependence from the Dutta-Horn activated kinetic factor drops out, leaving only the T-dependence from the thermodynamic factor. The temperature dependence of the quantum tunneling rate is weak, thus the total noise scales linearly in temperature.

It can be shown that the tunneling TLS relaxation rate and the distribution in equation 3.28 lead to the $P \propto 1/\tau$ wide distribution of TLS lifetimes required to integrate out to a $1/f$ power spectral density [81]. Figure 3.3 shows a simulated distribution of tunneling TLS lifetimes τ, given the presumed distribution (equation 3.28). It shows clearly the wide distribution of lifetimes as $P \propto 1/\tau$, which yields a $1/f$ power spectral density.
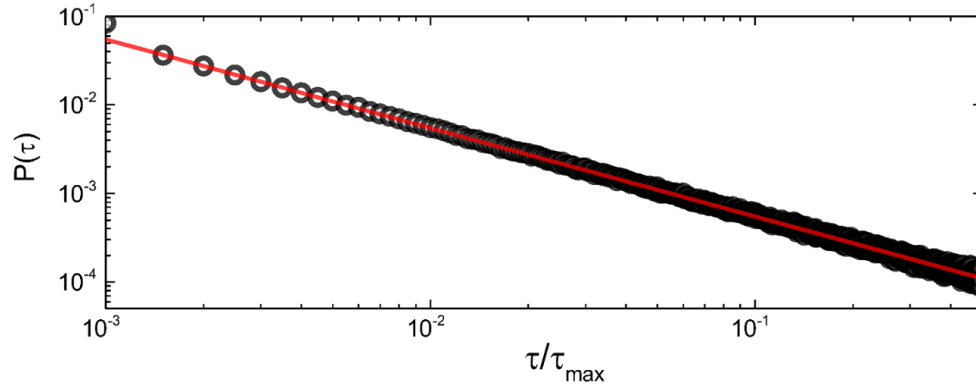
Figure 3.3: Simulated distribution of the tunneling TLS lifetimes. The tunneling TLS model results in a distribution $P(\tau) \propto 1/\tau$, which gives rise to $1/\omega$ noise

CHAPTER 4

DEVICE FABRICATION

4.1 Al shadow evaporated junctions

(A)

(B)

490 nm

120 nm
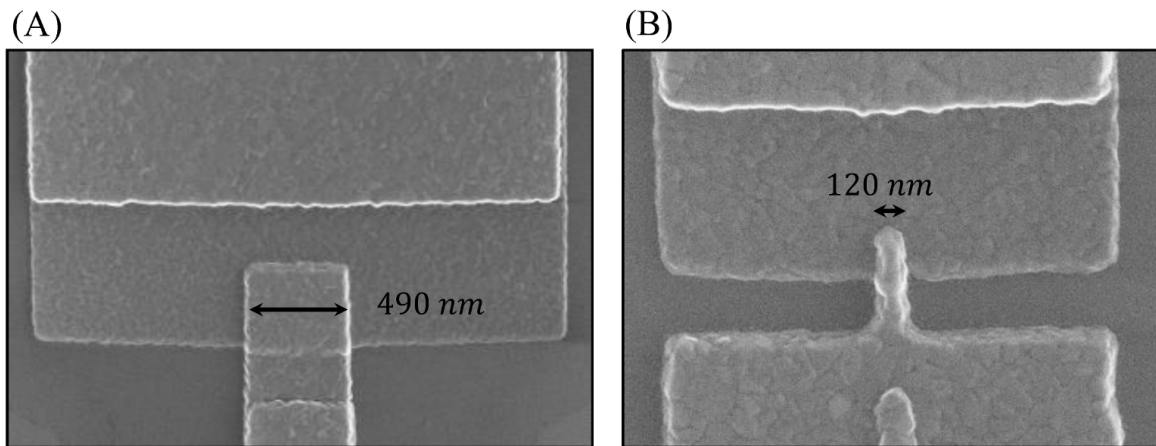
Figure 4.1: SEM images of the double angle evaporated aluminum Josephson junctions.

Our $Al/AlO_x/Al$ junctions were fabricated in the conventional double-angle shadow evaporation method. In contrast to the Nb-trilayer process, the Al double angle junctions have the advantage of requiring only one lithography step to fully define the junction. It is this simplicity that has made the double-angle evaporation method a popular standard in the superconducting devices community.

The junctions are defined via standard e-beam lithography at a 30 kV accelerating voltage. We used PMMA and MMA copolymer for our bi-layer resist stack. To maximize the undercut in the MMA layer, we typically pre-sensitize the MMA layer in a commercial EEPROM eraser unit, which is essentially a box with a timer controlled UV-lamp. The development was

performed in a 1:3 MIBK:IPA solution at room temperature.

The Al evaporation was performed in an ultra-high vacuum electron-beam evaporation cham-ber. The system is load-locked and can achieve a base pressure of $P_{base} \approx 3 \times 10^{-10}$ Torr. Prior to Al deposition the substrate is cleaned via a gentle Ar ion-milling to remove residual con-taminants. The typical Al evaporation rate is, $\approx 2 - 3$ Å/s.

Our standard process recipe is to define the Al-AlO$_x$-Al junctions with 40 nm of Al as the base electrode, followed by the tunnel barrier oxidation, and a 80 nm top electrode, for a total junction stack thickness of 120 nm. At the end of the top electrode evaporation, we typically flood the chamber to ~ 2 Torr of pure O$_2$ gas to cap the outer Al surfaces with a controlled native oxide.

4.1.1   Resistive shunt design

The resistive shunts were fabricated out of thin films of Palladium. The resistor lithography and deposition were done prior to the junction. We used e-beam lithography to define the resistor, and electron-beam evaporated palladium thin films, typically to a thickness $t \approx 60$ nm. An in-situ Ar ion-mill was performed immediately prior to the Al deposition, in order to ensure a good ohmic contact between the resistor and junction layers.

On each Pd evaporation we included a 4-terminal hall-bar test structure in parallel with the process chip. The test structure sits on the evaporation stage alongside the process chip, but on a separate substrate. The test structures were defined by a mechanical mask. This test structure allowed us to calibrate the sheet resistances of the Pd resistor layer on each evaporation run, allowing us to account for process variations. The Pd sheet resistance at $T = 4.2$ K is typically about 40% of the its value at room temperature.

In the overdamped RSJ most of the power is dissipated in the shunt resistors as long as $V_j < 2\Delta$. It is therefore important to design the shunting resistors to minimize the effects of electron heating. The basic principle is to create shunt resistors as thick and large as possible as to maximize the contact surface area to the substrate. In our resistively shunted junction

designs, we fabricated our shunting resistors with large cooling fins.

The hot electron effect in metals have been described by Wellstood [76, 68]. A uniform power, P, dissipated in a metallic thin film can raise the electron temperature T_e above the phonon temperature T_p of the thin film. The relationship is given by [76]:

$$T_e = \left(\frac{P}{\Sigma V} + T_p^5 \right)^{1/5} \tag{4.1}$$
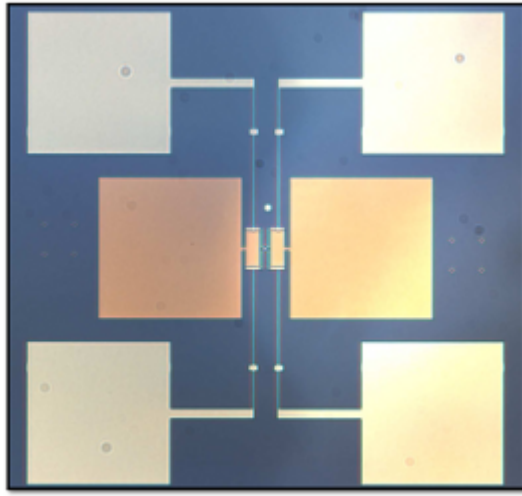
Figure 4.2: Optical microscope image showing the Pd resistive shunt design with large cooling fins.

In our typical measurement the junction is biased to approximately $V_j \approx 1 - 5 \ \mu\text{V}$, meaning the power dissipated in the shunts is approximately $1 - 25 \ \text{pW}/R_s$. Figure 4.2 shows an optical microscope picture of our AlO_x junction geometry. The lighter metallic traces are aluminum, while the darker gold colored metal traces are the palladium resistor and cooling fins. Note the size of the cooling fins, $A \approx (300 \ \mu\text{m})^2$, is the same size as the bonding pads.

4.2   SQUID Fabrication

As part of the IARPA collaboration we have performed low frequency noise measurements in SQUIDs to characterize the $1/f^\alpha$ low frequency magnetic flux noise. The SQUID measurements

were mainly performed by the group of John Clarke at the University of California, Berkeley, with SQUIDs fabricated by our group as an extension of this thesis work [4].

While this thesis will not cover the details of the work on SQUIDs performed in this IARPA collaboration, I will briefly cover the processes used to fabricate the SQUIDs.

(A)   (B)
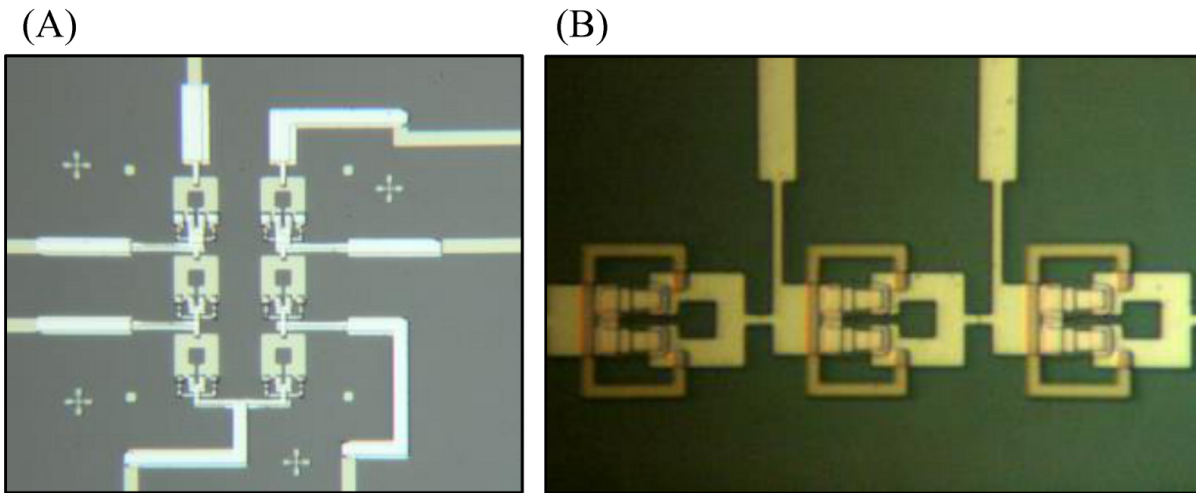
Figure 4.3: Optical microscope image of one side of the SQUID arrays. (A) Field view. (B) Higher magnification view.

We call this SQUID architecture the *hybrid-SQUID* design. The architecture was designed to allow the testing of a variety of metal growth and surface treatments of the SQUID loop superconductor, while the Josephson junctions are kept the same and made out of reliable double-angle evaporated Al junctions.

First the base layer is patterned. This is either a subtractive etch-down process in the case of epitaxially grown loop layer (such as epitaxial Nb or Al), or a simple lift-off process. Next the shunting resistors are defined via electron beam lithography, followed by a Pd electron beam evaporation and lift-off. We typically insert a 4-terminal test structure alongside the process chips in order to calibrate the sheet resistance of the shunt resistor layer. The resistance probe structures allow for small deviations of the sheet resistance to be adjusted in the subsequent layers to yield the designed resistance, as well as to provide quality control to our process flow.

The loop design was standardized to allow for one-to-one comparison between different

experiments. The loop design had dimensions $D = 4$ μm, $W = 3$ μm, giving a loop inductance, $L \approx 6.3$ pH. The screening parameter is approximately $\beta_L = I_c^{sq} L / \Phi_0 \approx 0.05$ for the design target $I_c^{sq} = 15$ μA. Each of the junctions are designed to have an area $A = 1.5 \times 0.5$ μm^2, with $J_c = 10$ $\mu A/\mu$m^2 so that $I_c^{sq} = 15$ μA.

Figure 4.3A is an optical microscope image showing a field view of the flux noise SQUID array. The SQUID loops and parts of the wiring traces appear slightly darker than the brighter sections of the Al junction and contact overlap sections. Figure 4.3B shows a higher magnification view showing the details of the SQUID architecture. The palladium resistor is clearly contrasted by the much darker color against the SQUID loop and junction layers.

4.3   Flux Qubit Fabrication
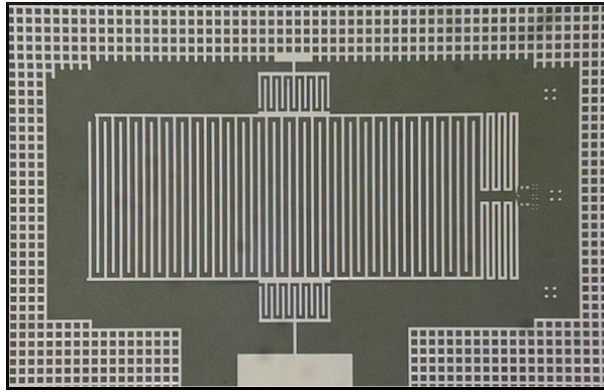
Figure 4.4: Optical microscope image of the lumped-element resonator layer. The qubit loop and junctions are to the right of the image. The qubit loop shares a trace with the resonator inductor. The current density determines the degree of flux coupling between the qubit and the resonator.

In the same spirit as the hybrid-SQUIDs used to test magnetic flux noise, we have fabricated hybrid flux qubits embedded in a lumped-element resonator. In the hybrid flux qubits the resonator and the qubit loop were fabricated from epitaxially grown Nb, while the qubit junctions were fabricated on a separate layer out of conventional aluminum double-angle evaporated junctions. Electrical contact between the junction and the base epitaxial layer was

ensured by performing a short ion mill prior to the junction deposition.

The following qubit measurements were performed by Jeffrey Birenbaum of John Clarke's group in UC Berkeley. In this section I will show some data to summarize our hybrid flux qubit effort.

The energy splitting of the flux qubit states is, $E_{01} = \sqrt{\Delta^2 - \epsilon^2}$, where at degeneracy $E_{01} = \hbar\omega_{01} = \Delta$. The fabrication parameters will determine the strength of the level splitting Δ, where a useful analytical approximation for the qubit energy splitting Δ is given by [27]:

$$\Delta \approx 4\sqrt{\frac{E_J E_c (2\alpha - 1)}{\alpha}} \exp\left[\sqrt{\frac{E_J(2\alpha + 1)}{\alpha E_c}}\left(\cos^{-1}\frac{1}{2\alpha} - \sqrt{4\alpha^2 - 1}\right)\right] \qquad (4.2)$$

Equation 4.2 above summarizes the difficulty in targeting fabrication parameters to yield a desired qubit frequency at degeneracy. Three of the major fabrication design parameters, the Josephson energy E_J, charging energy E_c, and the α-junction ratio α enters through the exponential term. Thus small variations in the fabrication can yield vastly different qubit characteristics.

We were never able to obtain hybrid flux qubits with good coherence properties. A typical energy spectroscopy of the hybrid qubit is given in figure 4.5. A large spectral broadening is already obvious from the energy spectroscopy and is typical of the results obtained from the hybrid architecture. Consequently the free-induction decay time, T_2^*, were usually very short making time-domain spectroscopy extremely difficult. Some possible problems in the hybrid architecture were: 1. Parasitic fourth junction. 2. Effect of ion-milling prior to junction deposition. 3. Very low Nb quality in the area of the inductor constriction which is shared with the qubit loop.

In contrast, our control device - all double-angle aluminum flux qubit - showed much higher coherence properties, typical of the best flux qubits at that time. Figure 4.6 shows an energy spectroscopy of a control all Al flux qubit, fabricated using the same process and instruments as those used in fabricating the hybrid flux qubits (with the exception of the all Al architecture).

Figure 4.7 shows a typical time-domain spectroscopy of the control all Al flux qubit, $T_1 \approx 2.6$ μs and $T_2^* \approx 1.4$ μs.
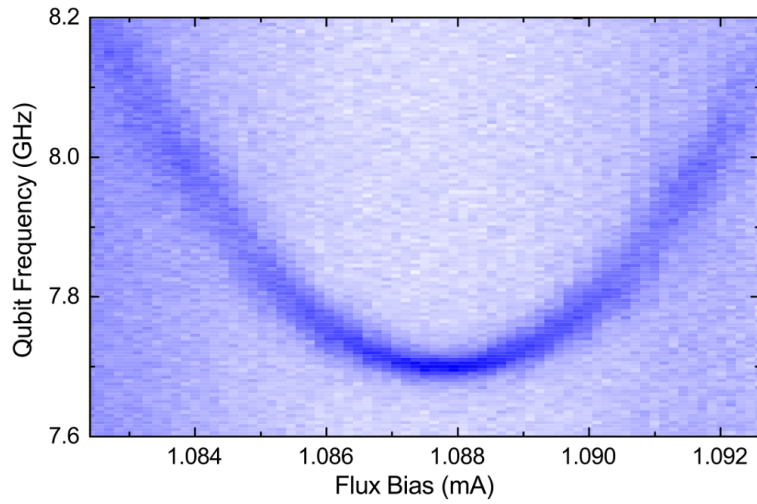
Figure 4.5:   Qubit spectroscopy of an epitaxial Nb hybrid flux qubit. Broad spectroscopic linewidth is apparent and reflected in the extremely short T_2^*.
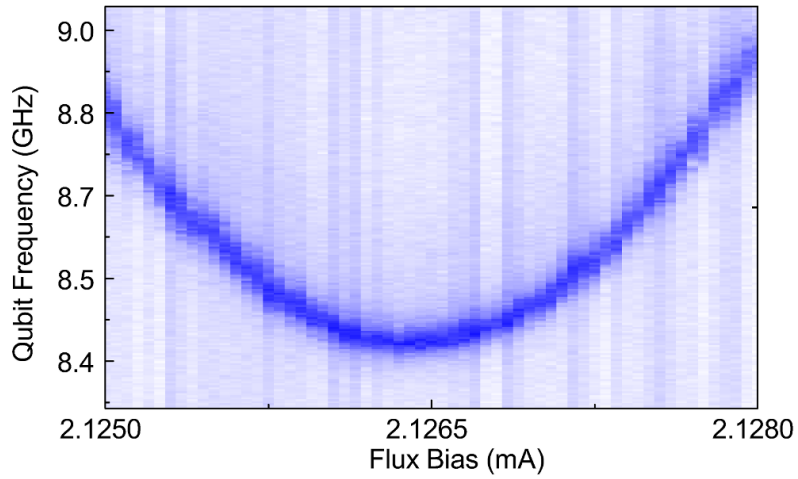
Figure 4.6:   Qubit spectroscopy of sample 5-ALA.
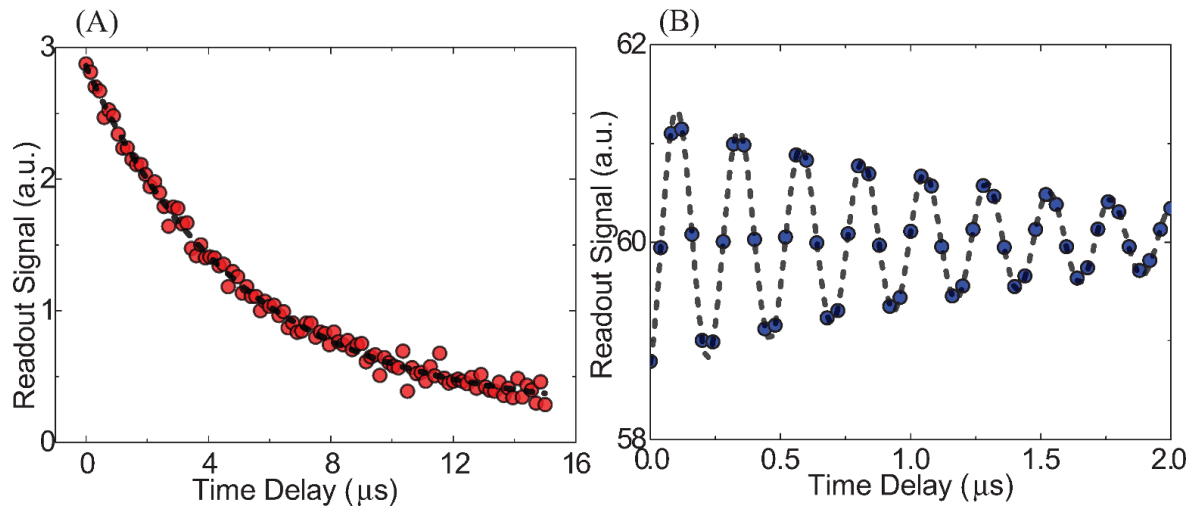
Figure 4.7: (A) T_1 energy relaxation spectroscopy. Dashed-line is an exponential decay time with $T_1 \approx 2.6$ μs. (B) Ramsey T_2^* spectroscopy. The Ramsey fringes are fitted to a decaying exponential enveloped (dashed-lines) with $T_2^* \approx 1.4$ μs.

CHAPTER 5

EXPERIMENTAL METHODS

5.1 dc-SQUID Amplifier

Figure 5.1: dc-SQUID sensor in a Nb-enclosure mounted on the 1K plate of the Oxford He-3 system.

We used a commercial SQUID sensor package purchased from Robin Cantor's STAR Cryo-electronics. The SQUID chip itself is embedded in a hermetically sealed carrier and installed inside a cylindrical Nb shielding enclosure. The SQUID used to perform the experiments in this thesis had an input coupling of 0.13 μA/Φ_0 and a flux locked loop voltage feedback response of 0.847 V_{FB}/Φ_0 at the $R_{FB} = 100$ kΩ feedback resistor setting.

5.1.1 Flux-locked loop

The basic physics of the SQUID has been covered in section 1.3, in this section we will briefly cover how the SQUID transfer function is linearized to operate it as an amplifier. We run our dc-SQUID amplifier in the flux-locked loop (FLL) mode, figure 5.3 shows the circuit schematic of the FLL operation. When the SQUID is biased into the voltage state, its voltage-flux
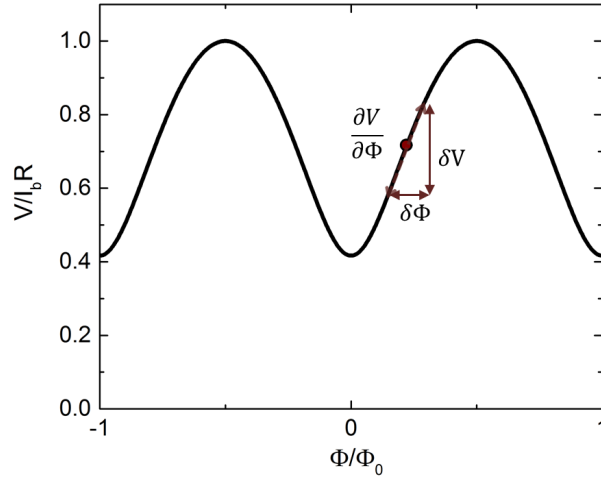
Figure 5.2: Voltage-Flux transfer function of a SQUID.

transfer function inherits the sinusoidal Φ_0 periodic structure of the critical current as shown in figure 5.2. The Voltage-Flux transfer coefficient is a maximum when the SQUID is biased near $\Phi \approx \Phi_0/4$. Small changes in flux $\delta\Phi$ about this operating point then translates to an approximately linear voltage change δV of the SQUID. In order to keep the SQUID operating linearly at this operating point even for large $\delta\Phi$, a flux-locked loop feedback circuit can be used. The FLL circuit feeds back a flux bias $\delta\Phi_{fb} = (V_{fb}/R_{fb})M_f$ which acts to cancel out the signal $\delta\Phi$ coupled into the SQUID loop, thus keeping the SQUID's operating point unmoved and remaining in the linear operating regime.

The SQUID is dc-current biased with a current I_b to some voltage state V_{sq}. Since the SQUID impedance is low, the voltage readout is achieved by modulating the SQUID voltage ($f_{mod} = 256$ kHz in our electronics) and impedance matching the SQUID through a cold $1:20$ transformer. At the room-temperature amplification chain, the signal is demodulated and passed through an integrator with an integrator capacitor, C_{int}. The signal is then fed back into the SQUID through a feedback resistor R_{fb}, appearing as a flux feedback signal $\delta\Phi_{fb}$, through a mutual inductance M_f. The product, $R_{fb}C_{int}$, defines the integration time constant. The input coil of the SQUID couples an input current signal, I_{sq}, through the mutual inductance M_i, so that I_{sq} is related to the flux feedback voltage V_{fb} as:
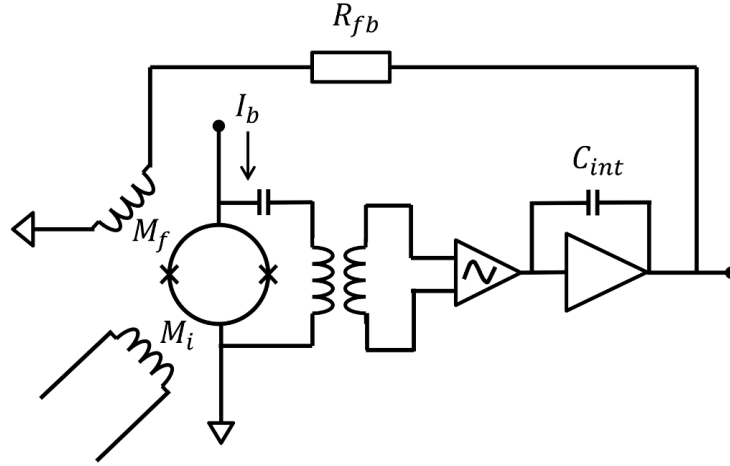
Figure 5.3: Flux-locked loop circuit schematic for the operation of a dc-SQUID.

$$V_{fb} = \left(\frac{M_i}{M_f}\right) I_{sq} R_{fb} \tag{5.1}$$

The parameters for the SQUID used in this thesis is given in the table below:

$1/M_i$	0.13 μA/Φ_0
$1/M_f$	8.47 μA/Φ_0

5.2   SQUID potentiometry circuit

To measure the critical current fluctuations of a Josephson junction, we used the SQUID as a low input impedance current amplifier in series with the test junction. The circuit is drawn in figure 5.4A. To make use of the SQUID potentiometry circuit we resistively shunt the Josephson junctions, typically $\beta_c \approx 0.3$, to avoid hysteresis. For critical current noise measurements, we bias the junctions to a very small voltage state, typically $1 - 5$ μV, such that the junction current is just above the critical current, $I_J \approx I_C$. Also the standard resistor R_{std} in the circuit is chosen so that $R_{std} \ll R_D$, where R_D is the dynamic resistance of the
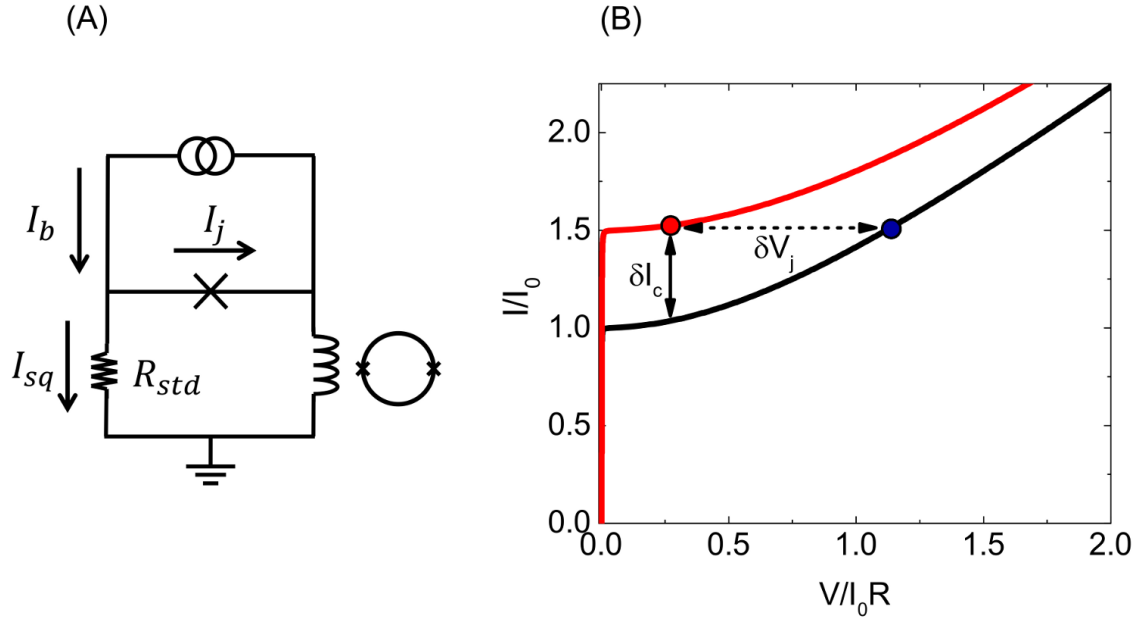
Figure 5.4: (A) Circuit schematic of the SQUID potentiometry circuit. (B) Illustration of the effect of δI_c fluctuations in the overdamped RCSJ model.

junction defined by:

$$R_D = \frac{\partial V_J}{\partial I_J} \tag{5.2}$$

Under the above circuit parameters and biasing conditions, the relationship between the critical current noise power spectral density and the noise power spectral density of the current I_{sq} detected through the SQUID is simply:

$$S_{I_{sq}} = S_{I_c} \tag{5.3}$$

The above result follows from a simple circuit consideration. The equipotential condition dictates that:

$$V_J = I_{sq}R_{std}, \tag{5.4}$$

and the current conservation forces:

$$I_b = I_J + I_{std} \tag{5.5}$$

We are interested in finding an expression for the fluctuation in I_{sq} with respect to fluctuations in I_c of the junction, so from equation 5.4 above:

$$\frac{dI_{sq}}{dI_c} = \frac{1}{R_{std}} \frac{dV_J}{dI_c} = \frac{1}{R_{std}} \left[\frac{\partial V_J}{\partial I_J} \frac{dI_J}{dI_c} + \frac{\partial I_J}{\partial I_c} \right] \tag{5.6}$$

From the current conservation condition, and using the fact that the bias current I_b is a constant, we have $dI_J/dI_c = -dI_{sq}/dI_c$, which implies:

$$\frac{dI_{sq}}{dI_c} = \frac{\partial V_J/\partial I_c}{R_{std} + R_D}, \tag{5.7}$$

We may use the ideal RSJ IV characteristics to simplify the above expression, from $V_J = R\sqrt{I_J^2 - I_c^2}$, we can show that:

$$\frac{\partial V_J}{\partial I_c} = \frac{-I_c R}{\sqrt{I_J^2 - I_c^2}} = -\left(\frac{I_c}{I_J} \right) R_D \tag{5.8}$$

It follows then the noise spectral densities $S_{I_{sq}}$ and S_{I_c} are related as:

$$S_{I_{sq}} = \frac{R_D^2}{(R_{std} + R_D)^2} \left(\frac{I_c}{I_J} \right)^2 S_{I_c} \tag{5.9}$$

At the chosen circuit parameters, $R_{std} \ll R_D$, and $I_J \approx I_c$, then we can see that this reduces to $S_{I_{sq}} = S_{I_c}$. For the standard resistors we thermally evaporated a thin film of Au/Cu alloy on 10×10 mm^2 sapphire substrates, followed by a Au evaporation to form the bonding pads. The Au bonding pads were not necessary but facilitates faster and more reliable wire bonds. The Au/Cu thin film resistor can be mechanically trimmed to adjust for the desired resistance, R_{std}, which is typically ≈ 1 Ω

How SQUID potentiometry measures changes in the critical current can be visualized as in figure 5.4. The voltage across an overdamped Josephson junction biased just above its critical current is very sensitive to the junction's critical current. To detect changes in the voltage

δV_j using a SQUID, we turn the voltage signal δV_j into a current signal I_{sq} by the use of a standard resistor R_{std}. For small values of R_{std} the current gain is large and ideally suited for SQUID amplification.

5.2.1   Extraction of junction IV
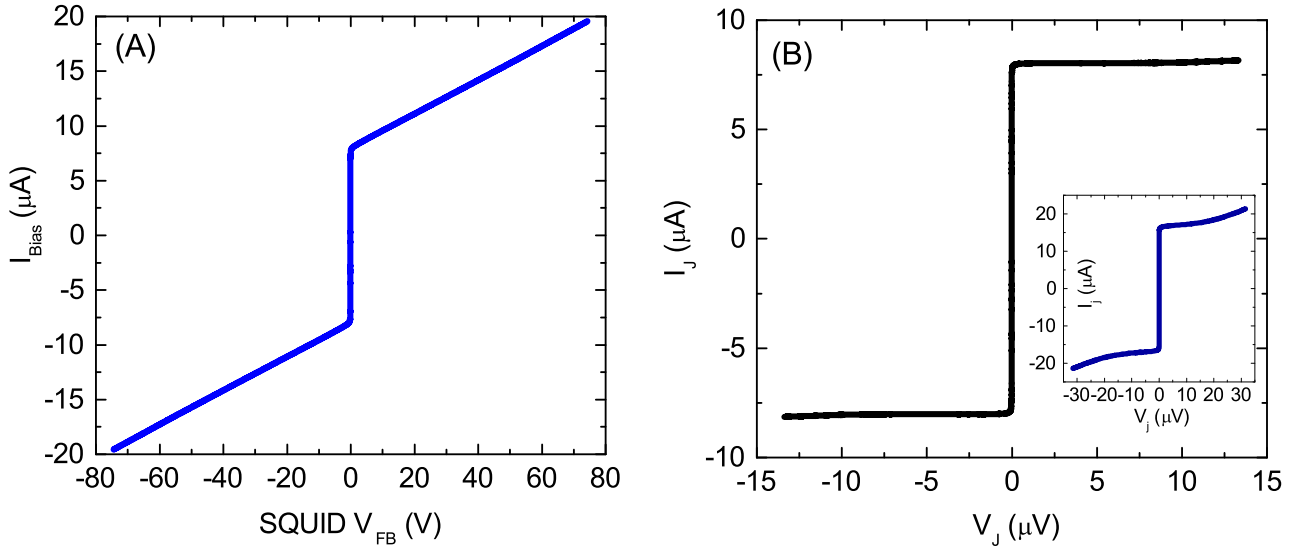
Figure 5.5: Measurement of Al-junctions at $T = 320$ mK. (A) SQUID response vs I_b. (B) Raw data converted into the junction IV parameters, I_j and V_j. In this case the bias range was not large enough, so that only the RCSJ IV range around the switching region was explored.

The use of the circuit in figure 5.4A permits the extraction of the junction IV characteristics after some mathematical transformation of the measured variables. The potentiometry circuit is biased by a known input current I_b, and the measurement output is the SQUID feedback voltage which is directly related to the current in the SQUID branch, I_{sq}. The junction current is then simply $I_J = I_b - I_{sq}$. The junction voltage is $V_J = I_{sq}R_{std}$, which requires a knowledge of the value of the standard resistor, R_{std}, and can be immediately calibrated by performing a Johnson-Nyquist noise spectroscopy at zero bias current.

At zero-bias current the junction loop total resistance is given by the sum of the standard resistor and other parasitic resistances such as the wirebond contact resistance and the copper

lines of the printed circuit boards. Typically however the standard resistor, R_{std}, is the dominant contribution, such that the Johnson-Nyquist noise seen by the SQUID at zero junction bias is given by:

$$S_I = \frac{4k_BT}{R_{std}} + c, \tag{5.10}$$

5.3 External biasing noise and temperature fluctuations

One difficulty in measuring small noise signals is the necessity to differentiate between trivial noise sources and the actual noise signal. Two common problems are the injection of current noise present through the biasing circuitry and temperature fluctuations due to poor cryostat stability. Low levels of $1/f$ low frequency noise are especially difficult to measure as they often necessitate long measurements, requiring system stability over 100s of seconds ($f \approx 0.01$ Hz).

In this work, external biasing noise is minimized by using an isolated battery to avoid the $1/f$ noise present in solid state amplifiers, especially in the active semiconductor amplifiers that are typically used in current source circuits. We used large capacity (8 Ah*capacity*) Pb-acid batteries in series with a large biasing resistor R, as our current bias source which is typically in the range $I_b = 10 - 100$ μA. We typically find a detectable battery drift in the first $1 - 2$ hrs after a re-charge, followed by a long period of stability. The battery would start to drift again once it has been discharged far enough, which is typically after approximately 1 month in our typical experiment run.

Temperature fluctuations of the cryostat can have an excess low frequency component and mimic a $1/f^\alpha$-like spectral density due to fluctuations in the temperature PID control loop. Often these instabilities appear as drifts which manifest as a $1/f^2$ power spectral component, therefore high values of α may (but not necessarily) indicate temperature instability. In the case of pressure oscillations in the 1 K plate pumping lines, the temperature instability appear as long period oscillations. In collaboration with Steven Anton at UC Berkeley, we have

investigated the manifestation of temperature induced fluctuations in the junction critical current [5]. The junction critical current is a temperature dependent quantity, given by the Ambegaokar-Baratoff relation:

$$I_c(T)R_n = \frac{\pi \Delta(T)}{2e} \tanh\left(\frac{\Delta(T)}{2k_B T}\right) \tag{5.11}$$

We find that the following approximate analytical form for $\Delta(T)$ is a good fit to our actual junctions [66]:

$$\frac{\Delta(T)}{\Delta_0} = \tanh\left(\frac{T_c}{T} \frac{\Delta}{\Delta_0}\right) \tag{5.12}$$

Unfortunately equation 5.12 above is transcendental in $\Delta(T)/\Delta_0$, hence we cannot explicitly solve for $\Delta(T)/\Delta_0$, however we can gain powerful insights from a numerical solution. The circles in figure 5.6A show the measured critical current of an Al/AlO$_x$/Al shunted junction at several temperature points, and fitted to the approximate theoretical temperature dependence (equations 5.11 and 5.12). The figure has been plotted in dimensionless units $i_c = I_c/I_0$ and $\tau = T/T_c$, the normalization for the measured data are $I_0 = 2.34$ μA and $T_c = 1.27$ K. The green triangles are data point from a second junction with normalization factors $I_0 = 10.8$ μA and $T_c = 1.27$ K. From the temperature dependence of the junction critical currents, we see that the AlO$_x$ junctions we fabricated follow the ideal SIS behavior. Figure 5.6B is a numerical differentiation of the theoretical dependence in figure 5.6A, showing the sensitivity of the critical current to temperature, $di_c/d\tau$. For the theoretical curves we have used the BCS result $\Delta_0 = 1.764$ $k_B T_c$.

For $T > \approx 0.3$ T_c, $di_c/d\tau \neq 0$ and one must be careful to exclude thermal fluctuations from measurements of the junction critical current. The temperature induced critical current noise, $S_{I_c}^T$, can be related to the noise power spectral density of the temperature instability (S_T):

$$\frac{S_{I_c}^T}{I_c^2} = \left(\frac{di_c}{d\tau}\right)^2 \frac{S_T}{T^2} \tag{5.13}$$
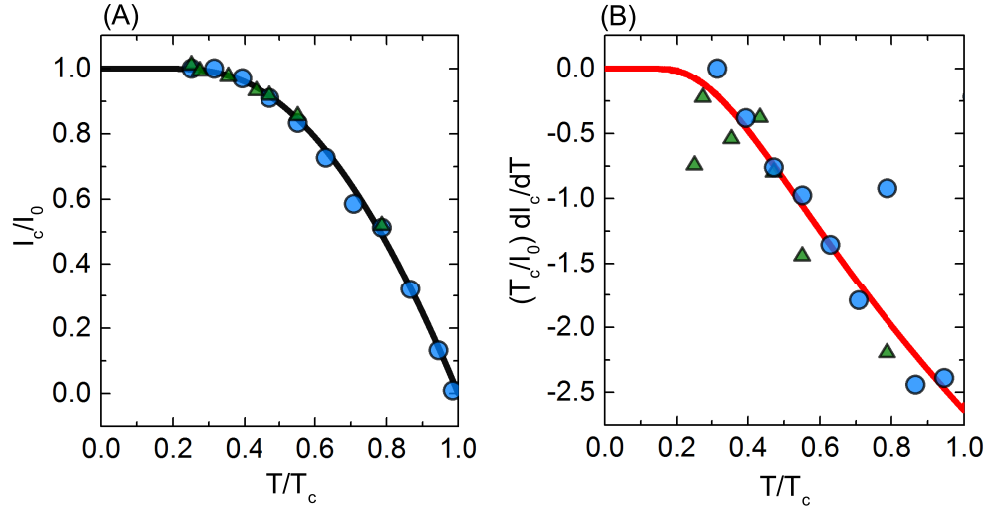
Figure 5.6: (A) I_c vs Temperature. In dimensionless units $i_c = I_c/I_0$ and $\tau = T/T_c$. (B) The dimensionless sensitivity $di_c/d\tau$ vs τ.

Note that the dimensionless transfer coefficient $di_c/d\tau$ can be significant as plotted in figure 5.6B. That is, bath temperature variation is of no concern in Nb junctions due to its high $T_c \approx 9.2$ K, implying $di_c/d\tau \approx 0$ for temperatures $T <\approx 3$ K. On the other hand measurements involving Al junctions are susceptible to bath temperature fluctuations due to the low T_c of Al. This necessitates a good control of the temperature in order to minimize S_T, and/or as we shall discuss in the next section, a method that removes this sensitivity. Fortunately the problems of external noise and bath temperature fluctuations polluting the noise signal to be measured are not unique to the case of Josephson junctions. A wealth of knowledge has been accumulated from experiments looking at low frequency noise in metallic thin films. In particular, Scofield [62] has reviewed in 1987 a measurement circuit utilizing an ac-bridge with a center-tapped four probe geometry in order to measure the low frequency resistance noise in metal films, while rejecting contact noise and bath temperature fluctuations. In this same spirit, we adapted our SQUID potentiometry circuit into a version of the bridge circuit in order to exploit similar protection against external noise.

5.4 Bridge SQUID potentiometry circuit
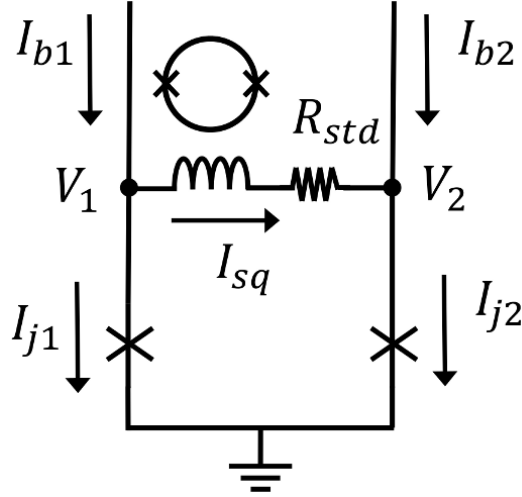
Figure 5.7: Electrical schematic of the SQUID bridge circuit.

Motivated by the center-tapped four probe resistance bridge circuit [62], we adapted a similar geometry to work with the dc-SQUID amplifier. Instead of the high-impedance amplifiers used in the traditional bridge circuits to measure voltage fluctuations, we used the dc-SQUID as a low-impedance and ultra low-noise current amplifier to measure current fluctuations. In place of the center tapped four-probe resistance structure, we fabricated on a single chip two matched resistively shunted Josephson junctions to be placed in each arm of the bridge circuit. Figure 5.8 shows a SEM image of junctions used in the bridge circuit. The two matched junctions in essence act to replicate the role of the center-tapped resistor. The circuit is also essentially the RSJ equivalent of the bridge circuit we used to measure resistance fluctuations in unshunted junctions at voltages above the superconducting gap [18] (section 5.7). The matched junctions are fabricated in the same lithographic step and are only spatially separated by 15 μm. The close spatial proximity reduces spatial variations in the fabrication process, thereby achieving high degree of matching. The bridge circuit is sensitive to the *uncorrelated* critical current fluctuations of the two Josephson junctions, while at the same time insensitive to *correlated* external noise sources such as the bias current noise and bath temperature fluctuations.
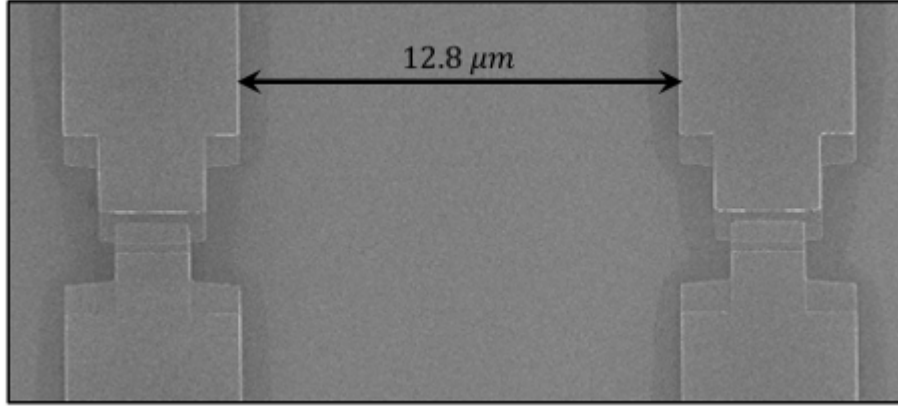
Figure 5.8: SEM image of the on-chip and matched Josephson junctions for the SQUID bridge measurement.

The electrical schematic of this SQUID bridge circuit is shown in figure 5.7. We used potentiometers at room temperature to perform coarse and fine adjustment of the bias currents I_{b1} and I_{b2}. In the *zeroth order* operation of the circuit, we current bias the two junctions such that they are at equal potential, $V_{j1} = V_{j2}$. The equipotential operating point is indicated by zero current flowing through the standard resistor, $I_{std} = 0$, which can be precisely monitored by tracking the dc-SQUID response to the biasing currents. While we most often use the equipotential operating point, $I_{std} = 0$, especially when the two junctions are well matched, we have also operated the circuit with small voltage offsets, $\Delta V = V_{j1} - V_{j2} = I_{sq}R_{std}$. Though rarely operated in this way due to the added complexity in tuning the circuit, non-zero voltage offsets can be used to compensate small junction I_c mismatches, to regain the equality of the junction voltage sensitivity with respect to temperature fluctuations, $dV_{j1}/dT = dV_{j2}/dT$. This procedure can be used to maximize the rejection of the correlated bath temperature fluctuations.

In the zero-voltage state the only resistance in the loop is R_{std}, therefore the value of R_{std} can be calibrated via Johnson-Nyquist spectroscopy (section 5.5). The standard resistor is chosen such that the dynamic resistance R_d of the junctions at the measurement biasing point is much larger than the standard resistor R_{std}. This is chosen to maximize the sensitivity of the SQUID to I_c fluctuations in the junctions. In practice we have implemented the circuit
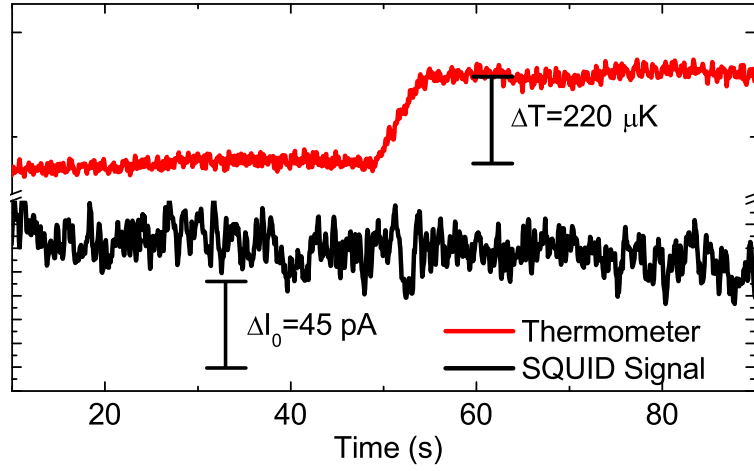
Figure 5.9: dc-SQUID response to a bath temperature step. The dc-SQUID signal and fridge cold finger thermometer are simultaneously sampled. The temperature of the He-3 fridge was increased in an abrupt step by $\Delta T \approx 220~\mu$K. The effect of this temperature step is not discernible in the dc-SQUID response.

with $R_{std} \approx 0.3 - 0.5~\Omega$.

Similar to the single JJ SQUID potentiometry circuit, it is possible to obtain the full IV characteristics of each of the two junctions. For example the full IV characteristics of J1 can be obtained by ramping the bias current I_{b1}, while the current bias I_{b2} is set to null out the current flowing through J2 to keep J2 in the zero voltage state. This is done by setting $I_{b2} = -I_{sq}$, which forces $I_{j2} = 0$ from current conservation. With this biasing procedure the current and voltage through J1 can be obtained in a similar manner as in section 5.2.1. The junction current is, $I_{j1} = I_{b1} - I_{sq}$, and the voltage, $V_{j1} = I_{sq}R_{std}$.

It is also possible to obtain the IV characteristics very near to the voltage state transition by following a simpler procedure where I_{b2} is kept at zero (for the IV of J1, and vice versa). In this manner the IV characteristics in the voltage range $V_{j1} = 0$ to $V_{j1} = I_{c2}R_{std}$ can be mapped out. For $V_{j1} > I_{c2}R_{std}$, J2 is driven into the voltage state and the extraction of V_{j1} is no longer straightforward. Figure 5.10 shows an example of the IV curves at $T = 315$ mK obtained in this manner. The region around the voltage state transition is clearly mapped, a sharp turn-on at approximately $V_j \approx 20~\mu$V is related to the turn-on of the second junction.
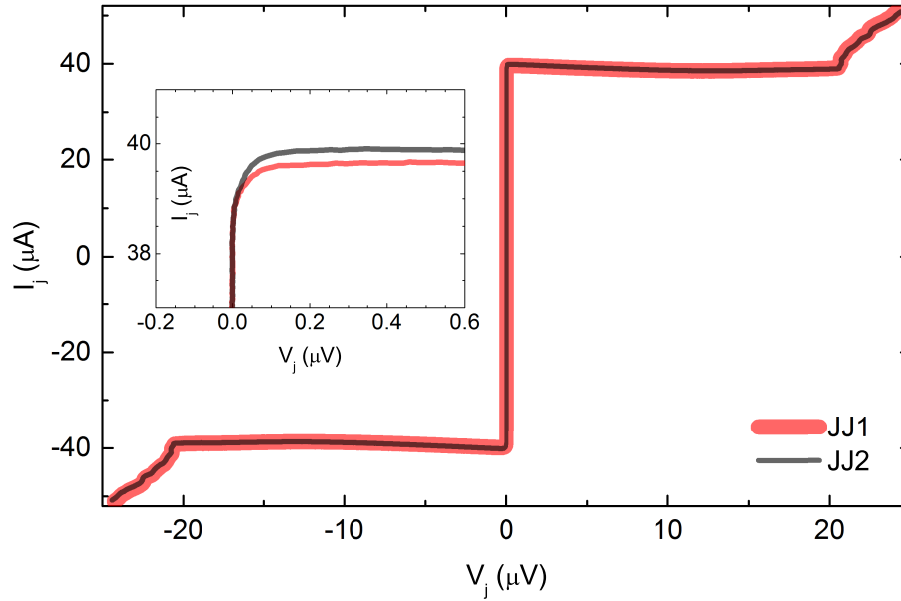
Figure 5.10: IV characteristics of two junctions in the SQUID bridge circuit at $T = 315$ mK. (red solid line) IV curve of JJ1, $I_c \approx 39.7$ μA. (black solid line) IV curve of JJ2, $I_c \approx 39.9$ μA. The two junctions are matched to within 99.5% (inset) Zoomed-in view around the voltage-state transition region.

The inset of figure 5.10 is a zoomed-in view showing the high degree of I_c matching across the two junctions, $I_c^{\text{J1}} \approx 39.7$ μA and $I_c^{\text{JJ2}} \approx 39.9$ μA, giving $\alpha \approx 0.995$ (99.5% matching).

5.4.1   Non-zero finite bias

Here the full RSJ behavior of the junctions need to be taken into account. This is where we get sensitivity to critical-current fluctuations. We assume that the junctions follow RSJ behavior:

$$V_j = R_s \sqrt{I_j^2 - I_c^2} \tag{5.14}$$

The dynamic resistance R_D is given by:

$$R_D = \frac{\partial V_j}{\partial I_j} = \frac{I_j R}{\sqrt{I_j^2 - I_c^2}} \tag{5.15}$$

A related quantity is the partial derivative $\partial V_j / \partial I_c$, which is given by:

$$\frac{\partial V_j}{\partial I_c} = -\frac{I_c R}{\sqrt{I_j^2 - I_c^2}} = -R_D \left(\frac{I_c}{I_j} \right) \tag{5.16}$$

In the bridge circuit let us label I_1 and I_2 to be the current flowing through the junctions. Such that:

$$I_1 = I_A + I_{sq} \tag{5.17}$$

$$I_2 = I_B - I_{sq}, \tag{5.18}$$

where I_A and I_B are the constant bias currents in junctions 1 and 2 respectively. Next, the voltage equality condition holds that:

$$V_2 - V_1 = I_{sq} R_{std} \tag{5.19}$$

Without loss of generality, let us first assume that JJ1 is fluctuation-less. That is $S_{Ic,1} = 0$. We will solve the signal sensitivity to fluctuations in I_{c2}:

$$R_{std} \frac{dI_{sq}}{dI_{c2}} = \frac{dV_2}{dI_{c2}} - \frac{dV_1}{dI_{c2}} \tag{5.20}$$

Now, taking care to take the *full* derivative:

$$\frac{dV_2}{dI_{c2}} = \frac{\partial V_2}{\partial I_{c2}} + \frac{\partial V_2}{\partial I_2} \frac{dI_2}{dI_{c2}} \tag{5.21}$$

$$= -R_{D2} \left(\frac{I_{c2}}{I_2} \right) + R_{D2} \frac{dI_2}{dI_{c2}} \tag{5.22}$$

Likewise the full derivative for the second term dV_1 / dI_{c2} can be evaluated as follows:

$$\frac{dV_1}{dI_{c2}} = \frac{\partial V_1}{\partial I_1} \frac{dI_1}{dI_{c2}} + \frac{\partial V_1}{\partial I_{c1}} \frac{dI_{c1}}{dI_{c2}} \tag{5.23}$$

$$= R_{D1} \frac{dI_1}{dI_{c2}} \tag{5.24}$$

Putting these two terms together, this time observing that the current conservation condition imposes the condition, $dI_2 = -dI_{sq}$ and $dI_1 = dI_{sq}$:

$$R_{std}\frac{dI_{sq}}{dI_{c2}} = -R_{D2}\frac{I_{c2}}{I_2} - R_{D2}\frac{dI_{sq}}{dI_{c2}} - R_{D1}\frac{dI_{sq}}{dI_{c2}} \tag{5.25}$$

$$(R_{std} + R_{D1} + R_{D2})\frac{dI_{sq}}{dI_{c2}} = -R_{D2}\left(\frac{I_{c2}}{I_2}\right) \tag{5.26}$$

$$\frac{dI_{sq}}{dI_{c2}} = -\frac{R_{D2}}{R_{std} + R_{D1} + R_{D2}}\left(\frac{I_{c2}}{I_2}\right) \tag{5.27}$$

We find that the noise power due to fluctuations in I_{c2} is given by:

$$S_{I_{c2}}^{sq} = \frac{R_{D2}^2}{(R_{std} + R_{D1} + R_{D2})^2}\left(\frac{I_{c2}}{I_2}\right)^2 S_{I_{c2}} \tag{5.28}$$

By symmetry the noise power due to fluctuations in I_{c1} is given by:

$$S_{I_{c1}}^{sq} = \frac{R_{D1}^2}{(R_{std} + R_{D1} + R_{D2})^2}\left(\frac{I_{c1}}{I_1}\right)^2 S_{I_{c1}} \tag{5.29}$$

We note that since the critical-current noise in the two junctions are *uncorrelated*, then their noise power *adds* to give the total noise power density. So that the total noise power density at the SQUID is:

$$S_I^{sq} = \frac{R_{D1}^2}{(R_{std} + R_{D1} + R_{D2})^2}\left(\frac{I_{c1}}{I_1}\right)^2 S_{I_{c1}} + \frac{R_{D2}^2}{(R_{std} + R_{D1} + R_{D2})^2}\left(\frac{I_{c2}}{I_2}\right)^2 S_{I_{c2}} \tag{5.30}$$

The above equation simplifies greatly if we now take into account that the two junctions are very well matched such that $R_D = R_{D1} = R_{D2}$, and we operate the circuit in the regime $I_{c1}/I_1 = I_{c2}/I_2 \approx 1$. Furthermore we design the circuit such that $R_{std} << R_D$. Figuring all of these factors:

$$S_I^{sq} = \frac{1}{4}\left(S_{I_{c1}} + S_{I_{c2}}\right) \tag{5.31}$$

Defining the average critical-current noise power to be, $S_{I_c} = \frac{1}{2}(S_{I_{c1}} + S_{I_{c2}})$, we have our

final relationship:

$$S_I^{sq} = \frac{1}{2} S_{I_c} \tag{5.32}$$

The signal visibility at the SQUID is only *half* of the full critical-current noise power. Compare this with the sensitivity of the non-bridge 1-JJ SQUID potentiometry circuit which is $S_I^{sq} = S_{I_c}$. However this *small* reduction in sensitivity is greatly offset by the common-mode noise rejection offered by the bridge configuration. The immunity to common-mode noise is critical in rejecting spurious temperature instabilities of the fridge, and allows us to isolate the fundamental critical-current noise of the Josephson junctions.

5.4.2   Common-mode rejection

Making the standard simplification for the operating circuit:

$$\frac{dI_{sq}}{dI_{c1}} = \frac{1}{2} \tag{5.33}$$

$$\frac{dI_{sq}}{dI_{c2}} = -\frac{1}{2} \tag{5.34}$$

$$\frac{dI_{sq}}{dT} = \frac{dI_{sq}}{dI_{c1}} \frac{dI_{c1}}{dT} + \frac{dI_{sq}}{dI_{c2}} \frac{dI_{c2}}{dT} \tag{5.35}$$

$$\frac{dI_{sq}}{dT} = \frac{1}{2} \left(\frac{dI_{c1}}{dT} - \frac{dI_{c2}}{dT} \right) \tag{5.36}$$

The Ambegaokar-Baratoff relationship provides a functional form of the temperature dependence:

$$I_c = \frac{\pi \Delta(T)}{2eR_n} \tanh \left(\frac{\Delta(T)}{2k_B T} \right) \tag{5.37}$$

Since both junctions are metallized at the same step, it is reasonable to assume that superconducting energy gap $\Delta(T)$, which depends only on the superconductor quality, are identical across both junctions. The temperature dependence is therefore parameterized in the normal-state resistance of the junctions which may differ due to local oxidation variations. Suppose

the two junctions are matched so that:

$$\frac{I_{c1}(T)}{I_{c2}(T)} = \frac{R_{n2}}{R_{n1}} = \alpha \tag{5.38}$$

Then,

$$\frac{dI_{c1}}{dT} = \alpha \frac{dI_{c2}}{dT} \tag{5.39}$$

So that the common-mode signal seen at the SQUID is given by:

$$\frac{dI_{sq}}{dT} = \frac{1}{2}(1 - \alpha)\frac{dI_c}{dT} \tag{5.40}$$

$$S_{I,sq}^T = \frac{1}{4}(1 - \alpha)^2 (dI_c/dT)^2 S_T \tag{5.41}$$

Compare this to the un-attenuated (non-bridge) signal sensitivity to temperature fluctuations, $S_{I,sq}^{T,*} = (dI_c/dT)^2 S_T$, the common-mode attenuation is given by:

$$\eta = \frac{1}{4}(1 - \alpha)^2 \tag{5.42}$$

For junctions with 99% matching, we have an attenuation of over $\eta \approx 4 \times 10^4$. Note that this achieves the required attenuation of spurious temperature-noise even at 1 K ($T/T_c = 0.77$).

5.5   Johnson-Nyquist noise calibration of R_{std}

Precise value of the standard resistor R_{std} can be obtained by performing a Johnson-Nyquist noise spectrometry. At zero bias, $I_b = 0$, the junctions are in the superconducting state and the white noise component at high frequencies, typically in the range $f = 10 - 10$ kHz, is then dominate by the thermal Johnson-Nyquist noise of the standard resistor:

$$S_I = \frac{4k_B T}{R_{std}} + S_I^{\text{bgnd}} \tag{5.43}$$
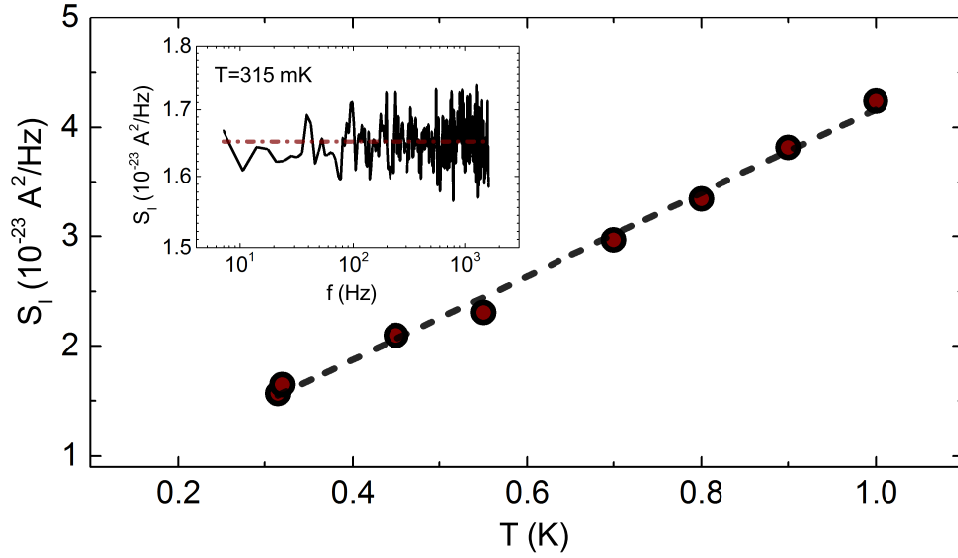
Figure 5.11: Johnson noise spectroscopy of the white noise background at high frequencies. The dark dashed line is a fit to $S_I = 4k_BT/R_{std} + c$, where the slope can be used to extract the value of the standard resistor. (inset) Example of the power spectral density at high frequencies, showing a white spectrum dominated by the thermal noise of R_{std}

Where in general there can be a constant white background noise term S_I^{bgnd}, which will flatten the temperature dependence at low temperatures. Therefore an accurate noise spectroscopy will have to be taken at several different temperature points at fitted to equation 5.43, where the slope is then related to R_{std}. However for small values of R_{std}, the Johnson-Nyquist noise is large enough to overwhelm this background noise, as seen in figure 5.11. In this trace the fitting yields $R_{std} \approx 1.4\ \Omega$, and the limiting background noise term is small compared to the Johnson-Nyquist term.

5.6   Calibration of the measurement SQUID background noise

As part of the measurement qualification work, we have characterized the background low frequency noise of the measurement SQUID. State of the art SQUIDs are known to have a background magnetic flux noise in the few $\mu\Phi_0\text{s}/\sqrt{Hz}$. Characterization of our measurement SQUID's background noise can be performed at zero bias current, where the noise seen by the
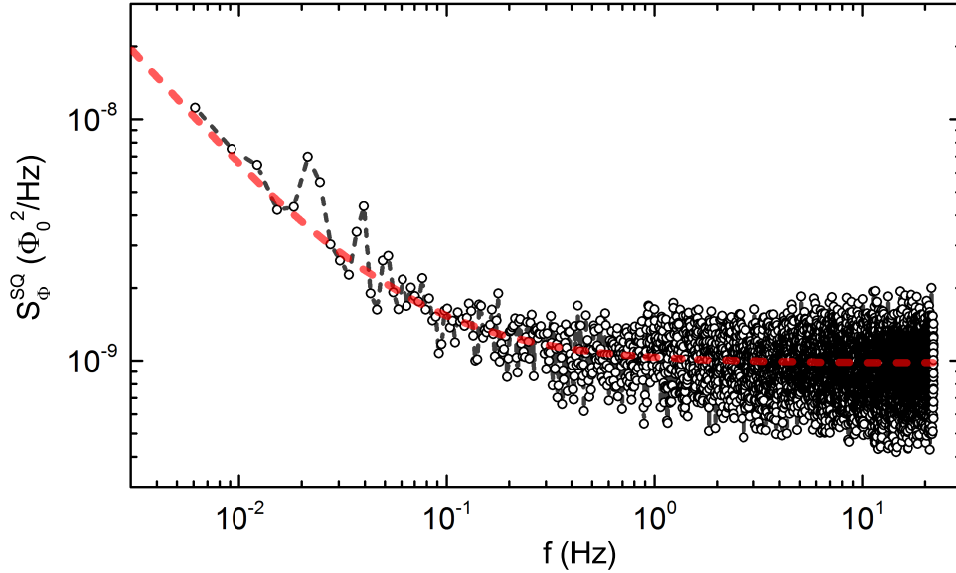
Figure 5.12: Power spectral density of the background noise, including the measurement SQUID's low frequency flux noise and the amplification chain. The dashed red line is a fit to $S_\Phi = A/f^\alpha + C$, with $A \approx (7.46~\mu\Phi_0)^2$, $\alpha = 1$, and $C = 9.76 \times 10^{-10}~\Phi_0^2$

SQUID is given by:

$$S_\Phi = \frac{A}{f^\alpha} + C \tag{5.44}$$

Where C is the white noise contribution due to the standard resistor R_{std} being present in the loop. The first term reflects the background low frequency noise present in our SQUID and measurement chain. Figure 5.12 plots the low frequency spectra of the SQUID and the amplification chain. We find that we can best fit the background low frequency to $\alpha \approx 1$ and $A \approx (7.46~\mu\Phi_0)^2$.

5.7   Resistance fluctuation measurement setup

For measurements of the tunneling resistance noise S_{R_n}/R_n^2 we have used several different circuits. For measurements of large area junctions where the noise is well described by the a featureless $1/f$ spectrum, we have used the bridge circuit as shown in figure 5.13A, adapted
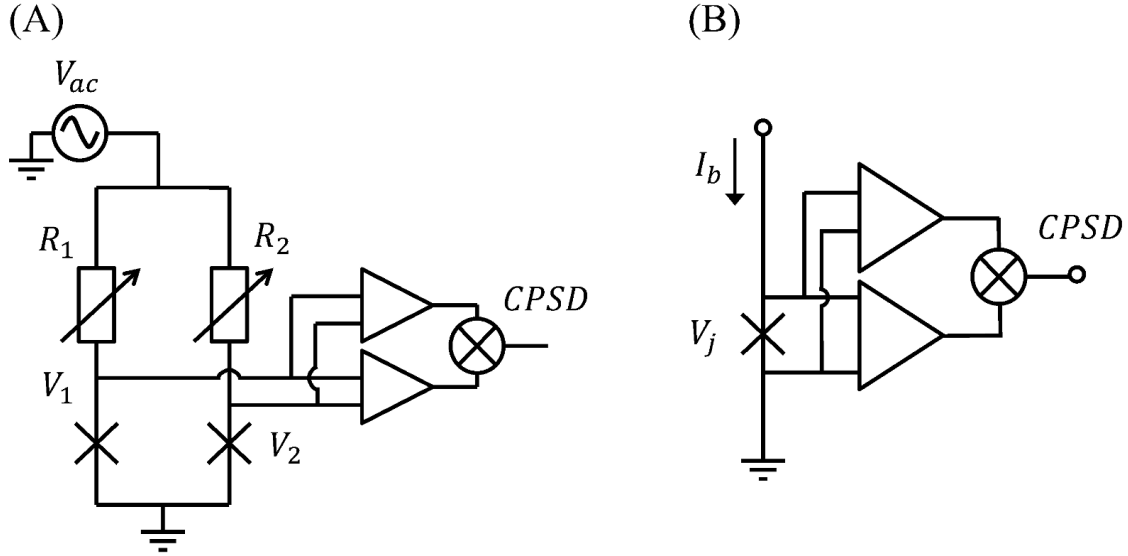
Figure 5.13: (A) Resistance wheatstone bridge circuit. (B) Single JJ cross-correlated resistance measurement setup.

from Eroms. et. al. [18]. In our implementation, we have always picked two junctions with the same area and transmissivity. The bridge circuit can be operated with either ac- or dc-excitation. With ac current bias we used a lock-in amplifier to demodulate the signal. To improve our noise signal's visibility well above the background low frequency noise of the amplifiers, we typically amplify the signal using two or more amplifiers. We then compute the cross power spectral density (CPSD) of the two amplifier signals. The junction voltage is a correlated quantity across the amplifiers, while the amplifier's voltage noise are uncorrelated.

By shifting the measurement frequency to a higher frequency, f_{ac}, we can avoid picking up the low-frequency noise of the amplifier itself.

5.8 Time Capture

We used a National Instruments PCIe-6251 data acquisition card to digitize and sample the voltage signal. The DAQ card used did not have the capability to perform true simultaneous sampling, however it is capable of sampling up to 1.25 MS/s across all sampled channels.
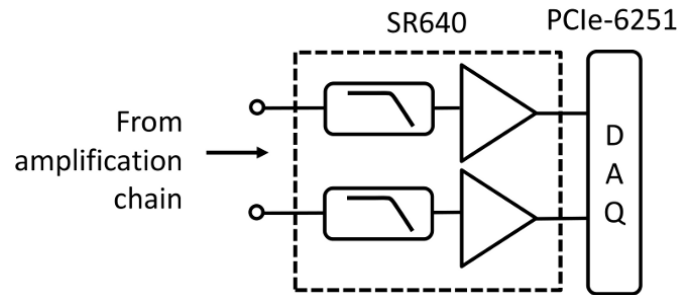
Figure 5.14: Circuit schematic of the signal digitization end. The SR640 is used as an anti-aliasing low pass filter, and provides the final gain before being digitized by a National Instruments PCIe-6251 DAQ card.

Therefore for our typical two channel cross correlation measurement we have a theoretical maximum sampling frequency of 625 kHz for each channel. However our system bandwidth, set by filtering and line impedances of the He3 fridge, is limited to around 10 kHz, therefore the sampling of the two channels is practically simultaneous (figure 5.15A).

We used a Stanford Research Systems SR640 programmable filter to perform a low-pass anti-aliasing filtering prior to sampling. The filter cut off frequency is determined by the bandwidth of the signal of interest, and the sampling frequency is set to at least twice the filter cut off frequency per the Nyquist-Shannon sampling theorem. In figure 5.15 the signal was sampled at $f_s = 400$ Hz and a low-pass cutoff frequency at $f_c = 185$ Hz was used. Figure 5.15B shows the computed cross power spectral density of the sampled signals in fig. 5.15A, where a sharp dip at $f = 185$ Hz is an artifact of the anti-aliasing low-pass filter cutoff.

The power spectral density (PSD) or the cross power spectral density (CPSD) of the digitally sampled time series were computed using standard MATLAB libraries.
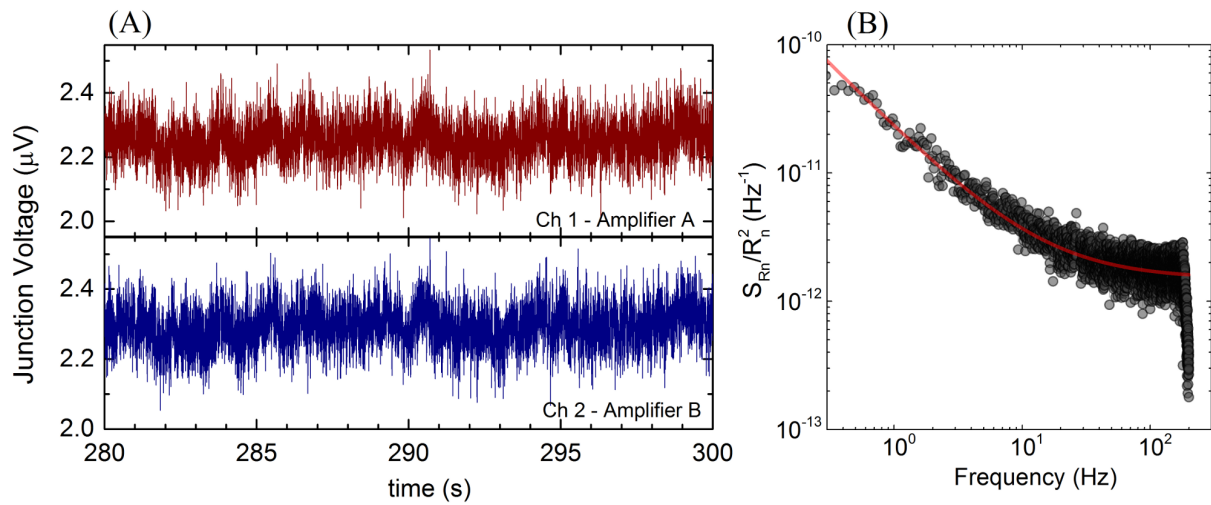
Figure 5.15: (A) Two independent channel sampling of two amplifier outputs. Uncorrelated noise between the two channels are the amplifier's intrinsic noise and can be rejected to improve the signal-to-noise ratio. (B) Cross-spectral density of the two time traces. (red dash) Fit to $1/f^\alpha$. Example traces from an $Al/AlO_x/Al$ tunnel junction at $T = 45$ K biased at $V_b = 0.5$ mV.

CHAPTER 6

CRITICAL CURRENT NOISE IN AL-ALO$_X$-AL JUNCTIONS

6.1   Introduction

In this chapter we will present our measurements of the critical current noise S_{I_c}/I_c^2 and tunneling resistance noise S_R/R^2 in Al-AlO$_x$-Al junctions. The measurements were done in both resistively shunted and unshunted junctions. For the shunted junctions we will present measurements of S_{I_c}/I_c^2 for $T < T_c$ and S_R/R^2 for $T > T_c$. We have made only measurements of S_R/R^2 in our unshunted junctions, but traversed a wider range of temperatures and junction areas.

At the start of this project it was suggested that the critical current noise in Josephson junctions follows a universal formula [67]:

$$\frac{S_{I_c}}{I_c^2} = 1.44 \times 10^{-10} \left(\frac{1}{f}\right) \left(\frac{1}{A/\mu m^2}\right) \left(\frac{T}{4.2 \ K}\right)^2 \ Hz^{-1} \tag{6.1}$$

However some more recent measurements seem to violate this proposed universal formula [18, 53], most notably with a linear T-dependence instead of the T^2 of the universal formula. A more detailed background review and a discussion on the state of the field is given in chapter 2. On the face of this contradictory body of experimental evidence, our motivation was therefore to better understand the properties of the low frequency $1/f$ critical current noise in Al-AlO$_x$-Al junctions, the junction architecture that has emerged to be widely implemented in various quantum coherent circuits. Other junction architectures, most notably the epitaxial trilayer junction architectures of Nb-AlO$_x$-Nb [11] and Re-AlO$_x$-Re [36], have been explored but have

yet provided the improvements to justify the added fabrication complexity over the simplicity of the double-angle evaporated Al-AlO$_x$-Al junctions.

As will be detailed in this chapter, our measurements of the $1/f$ noise in Al-AlO$_x$-Al junctions are consistent with other measurements by Eroms et. al. [18] and Pottorf et. al. [53]. In particular the measurements of Pottorf et. al. [53] and our own (section 6.4.4) in Nb-AlO$_x$-Nb junctions observed similar noise properties with other measurements in Al-AlO$_x$-Al junctions. This consistency suggests that the noise is a property of the common element, the amorphous diffused AlO$_x$ tunneling dielectric. Therefore we find that the $1/f$ noise magnitude and temperature dependence for tunnel junctions with a diffused amorphous AlO$_x$ barrier is well predicted by the formula:

$$\frac{S_R}{R^2} \equiv \frac{S_{I_c}}{I_c^2} \approx 1 \times 10^{-13} \left(\frac{T}{A/\mu\mathrm{m}^2} \right) \left(\frac{1}{f} \right) \ \mathrm{Hz}^{-1}, \tag{6.2}$$

where T is the temperature and A is the junction area in units of $\mu\mathrm{m}^2$.

From investigating the area dependence of the low frequency noise we have found an area and temperature (AT) threshold at which non-Gaussian effects become pronounced due to small number of activated TLSs, in other words a threshold for the breakdown of Gaussianity in the low frequency noise. This non-Gaussianity threshold and the magnitude of the $1/f$ power spectral density give an estimated TLS density of, $\sigma_0 \approx 4 \times 10^{13} \ \mathrm{m}^{-2}\mathrm{K}^{-1} \approx 40 \ \mu\mathrm{m}^{-2}\mathrm{K}^{-1}$.

6.2 Noise due to independent uncorrelated fluctuators

The $S_{I_c} \propto 1/A$ and $S_{I_c} \propto I_c^2$ dependence of the critical current noise is consistent and follows from the assumption of independent uncorrelated fluctuators that modulate the tunneling probability. In this model, each fluctuator contributes to a fractional change in the critical current, $\delta I_c/I_c$, which defines an *effective* fractional area of the fluctuator, $\delta A/A = \delta I_c/I_c$, such that $\delta A = (\delta I_c/I_c)A$, where A is the total area of the junction.

The partial noise power density due to a single fluctuator, k, is then given by, $S_{I_{c,k}} =$

$I_c^2(\delta A/A)^2$. The assumption that the fluctuators are uncorrelated means that the total noise power density is the sum of the individual partial noise power density contributions, $S_{I_c} = \sum_k S_{I_{c,k}} = \sum_k (\delta A/A)^2 I_c^2 = (N_{TLS}A)(\delta A/A)^2 I_c^2$, which gives:

$$S_{I_c} \propto I_c^2/A \tag{6.3}$$

Because of the $\propto I_c^2/A$ dependence, it is convenient to characterize the noise power spectral density in terms of the fractional power spectral density S_{I_c}/I_c^2 and normalizing them to an area $A = 1~\mu\text{m}^2$. This procedure effectively normalizes the extrinsic properties of the junctions (I_c and A), and allows the intrinsic properties of the $1/f$ low frequency noise to be compared between two junctions with dissimilar critical currents and areas.

6.3   Critical-current noise in shunted Al-AlO$_x$-Al junctions

6.3.1   Experimental setup

The resistively shunted Al-AlO$_x$-Al Josephson junctions were fabricated using the double-angle shadow evaporation technique, the junction electrodes and barrier oxidation are completed in one step without breaking vacuum. The evaporation was performed in a chamber with a base pressure of $\approx 3 \times 10^{-10}$ Torr. The shunt resistors, R_s, were fabricated by the electron-beam evaporation of Pd to a thickness, $t \approx 60$ nm. The resistor's sheet resistance was calibrated using auxiliary calibration structures processed in parallel with the junctions on each evaporation run. The typical low temperature ($T \approx 4.2$ K) sheet resistance is $R_s \approx 1.3~\Omega/\text{sq}$. The shunt resistors are patterned with large, $300 \times 300~\mu\text{m}^2$, cooling fins to minimize hot-electron effects [68]. More details of the fabrication procedures are given in chapter 4

Measurements of the critical current noise, S_{I_c}/I_c^2 were performed in the SQUID bridge circuit. Figure 6.1A shows the circuit schematic of the SQUID bridge potentiometry technique. A detailed discussion on the circuit operation is given in chapter 5.4. The SQUID bridge circuit
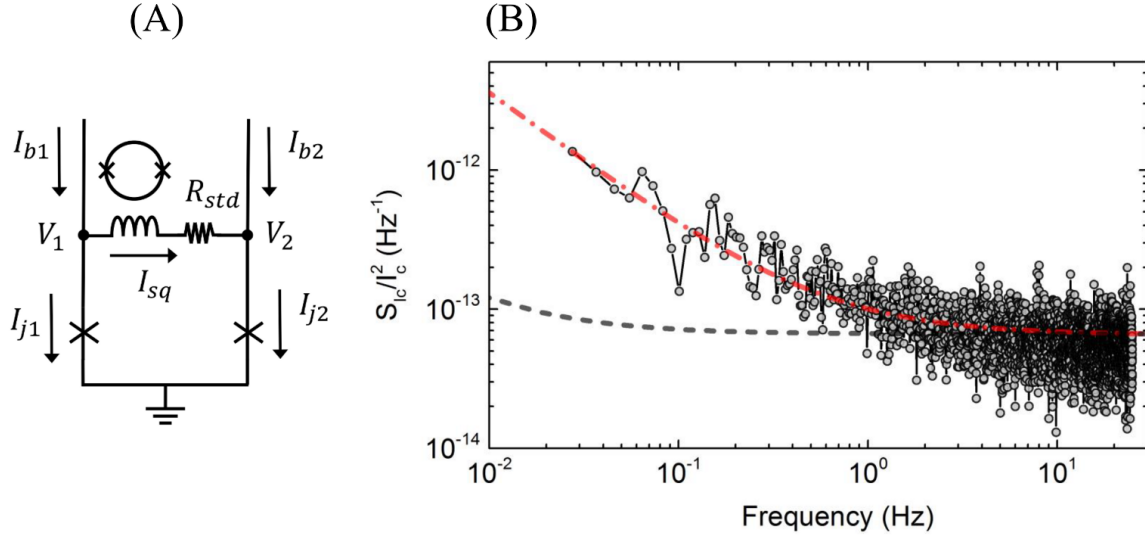
Figure 6.1: (A) Circuit schematic of the SQUID bridge circuit (see section 5.4 for operational details). (B) Example of the computed power spectral density. (circles) S_{I_c}/I_c^2 area normalized to 1 μm^2 for sample S3, $I_b/I_c \approx 1.005$. (red dash-dot) Fit to $S_{I_c}/I_c^2 = A/f + B$. Data is shown for four of the samples measured, S1, S2, S3, and S4. (grey dashed line) The background low frequency noise characteristics of the measuring SQUID.

uses a dc-SQUID sensor to monitor the current fluctuations in the Josephson junctions placed on the two opposite sides of the bridge circuit. A small standard resistor, $R_{std} \approx 0.5\,\Omega$, is placed in series with the SQUID pickup loop. The two shunted junctions in the bridge are matched and fabricated on-chip in the same lithography step. Potentiometers at room-temperature are used to adjust the currents through the junctions, while the dc-SQUID monitored the voltage imbalance, which is typically kept at zero. The current noise detected at the SQUID input is related to the critical current noise of the junctions by:

$$S_I^{sq} = \frac{1}{2} S_{I_c}, \tag{6.4}$$

a more detailed analysis is given in chapter 5.4. The reduction by a factor of two in the noise power sensitivity compared to the standard SQUID potentiometry technique is compensated by the large attenuation of common-mode noise sources, such as spurious temperature fluctuations and external biasing noise.

Following the analysis in chapter 5.4, the power attenuation factor of common-mode noise sources is given by: $\eta = \frac{1}{4}(1-\alpha)^2$, where α is the matching ratio of the junction critical currents, $\alpha = \min(I_{c1}, I_{c2})/\max(I_{c1}, I_{c2})$. In our on-chip *matched* junctions we are able to match the critical currents to within 1%, allowing for a high attenuation of small temperature fluctuations $\sim$ 100s μK.

The system background noise was determined by monitoring the SQUID output while keeping the junctions in the superconducting state (zero bias). The grey dashed line in figure 6.1B shows the system background noise, which has a base $1/f$ equivalent flux noise of $S_\Phi^{1/2}(1\ \text{Hz}) \sim 6\ \mu\Phi_o/\sqrt{\text{Hz}}$, consistent with the calibration data of the SQUID sensor. The background $1/f$ noise is subtracted from the measured data and the remainder is attributed to fluctuations in the junctions. The grey circles in figure 6.1B are data representative of the critical current measurements. In this case the data were taken from sample S3 at $T \approx 315$ mK with a current bias $I_b/I_c \approx 1.005$. The red dash-dot line shows a fitting curve to the form $S_{I_c}/I_c^2 = A/f^\alpha + B$, where $\alpha \approx 1$, A gives the power spectral density at 1 Hz, and B is the Johnson noise background related to the shunting resistor.

6.3.2 Measurements of S_{I_c}/I_c^2 in the superconducting state

We present here data from four of the samples measured, labelled as samples S1, S2, S3, and S4 with the following parameters:

Sample ID	I_0 (μA)	Area (μm^2)
S1	11	1.1
S2	10	0.3
S3	40	1.2
S4	2.9	0.15

Figure 6.2A shows the area dependence of the fractional critical current power spectral density (S_{I_c}/I_c^2) at 1 Hz. In this graph the fractional PSD has not been area normalized
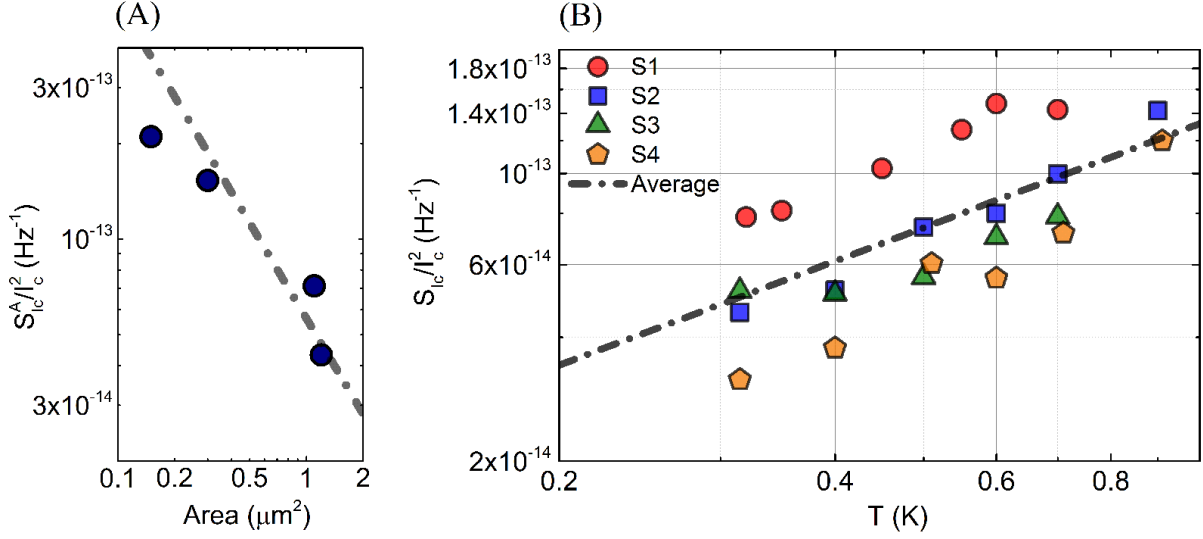
Figure 6.2: (A) Area dependence of the critical current fractional noise power spectral density, S_{I_c}/I_c^2. The gray dash-dot line is a fit to $\propto 1/A$ dependence. (B) Summary of the fractional noise PSD S_{I_c}/I_c^2 at 1 Hz and area normalized to 1 μm^2. The gray dash-dot line is a fit to a linear T-dependence.

to $A = 1$ μm^2 to explicitly observe the area dependence. The inverse area scaling $(1/A)$ of the fractional power spectral density is consistent with noise resulting from an ensemble of uncorrelated fluctuators. More importantly the observation of a $1/A$ dependence implies that the measured signal comes from fluctuations intrinsic to the junction, and not from fluctuations induced by bath temperature instabilities. The temperature induced fluctuation is independent of the junction area, given by (chapter 5.4):

$$\frac{S_{I_c}^T}{I_c^2} = \left(\frac{di_c}{d\tau}\right)^2 \frac{S_T}{T^2} = \kappa(T)\frac{S_T}{T^2}, \tag{6.5}$$

where $S_{I_c}^T/I_c^2$ is the fractional critical current noise PSD induced by temperature fluctuations having a PSD S_T/T^2, and $di_c/d\tau$ is a dimensionless sensitivity factor described by the Ambegaokar-Baratoff relationship (figure 5.6). On the other hand the noise originating from an ensemble of uncorrelated fluctuator modulating the junction I_c is expected to scale as $S_{I_c}/I_c^2 \propto 1/A$.

The measured critical current noise from all the samples are plotted in figure 6.2B. In this plot the fractional PSD S_{I_c}/I_c^2 have been normalized to $A = 1$ μm^2, in order to compare the intrinsic noise properties independent of the parameters of the junctions. The fractional PSD are observed to increase linearly with temperature, with the average T-dependence given by $S_{I_c}/I_c^2 \approx 1.3 \times 10^{-13}$ $(T/1$ K$)$ Hz^{-1} (figure 6.2B, grey dash-dot line).

6.3.3 Measurement extension into the normal state, S_R/R^2
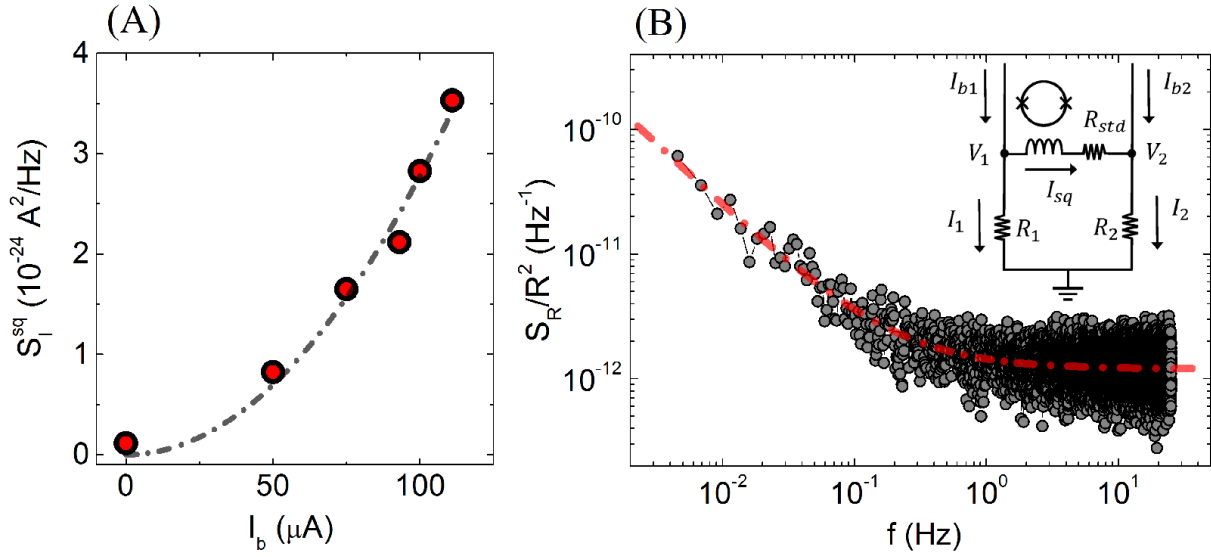
Figure 6.3: (A) I_b^2 bias dependence of the raw SQUID input current noise, S_I^{sq} for sample S3 at $T = 1.6$ K. Dashed line is a fit to $S_I^{sq} = AI_b^2$. (B) Noise power spectral density for sample S3 at $T = 1.6$ K and $I_b = 75$ μA. (Gray dashed-line) Fit to $S_R/R^2 = A/f + B$, where A and B are the fitting parameters. (inset) Electrical schematic of the SQUID bridge circuit where the Josephson junctions now act as a tunneling resistance in parallel with the shunt resistance.

Resistively shunted junctions are well suited for measuring critical current fluctuations in the superconducting state, while the parallel shunting resistance makes them less suited for the measurement of the tunneling resistance noise. Despite the presence of the shunting resistor we find that it is still possible to extract the tunneling resistance noise, if the effect of the shunting resistance is taken into account. We note that the tunneling resistance noise can be measured

by measuring at voltages higher than the superconducting gap, $V > 2\Delta$, or by measuring above the critical temperature of the superconductor $T > T_c$, additionally an external magnetic field can be applied to suppress both T_c and Δ. In this section we performed measurements of the tunneling resistance noise by measuring at temperatures above the T_c of our aluminum at zero field, ($T_c \approx 1.3$ K). Note that Rogers and Buhrman [54] have performed a similar measurement in resistively shunted Nb-PbBi edge junctions.

We performed measurements of the tunneling resistance noise in the SQUID-bridge samples S3 and S4. Recall that the SQUID-bridge circuit detects voltage fluctuations across the two junctions under test. In this case, for a resistive fluctuation δR, the resulting voltage fluctuation depends on the magnitude of the bias current I_b, $\delta V = I_b \delta R$. The current signal coupling into the SQUID input coil is then, $\delta I_{sq} \propto \delta V / R_{std} = I_b \delta R / R_{std}$. Thus we were able to compensate the small effective resistance fluctuation δR by using relatively large biasing currents I_b (when compared to the bias currents used in measuring in the superconducting state). We find that hot-electron effects are of no concern considering the significantly higher bath temperatures involved in measuring in the normal state, $T \approx 2 - 12$ K. We verify that the junctions are in temperature equilibrium by confirming that the noise signal scales quadratically with the biasing current, $S_{I_{sq}} \propto I_b^2$, as shown in figure 6.3A.

At $T > T_c$ the resistively shunted junction is simply a parallel network of two resistances, the junction tunneling resistance R_n and the shunting resistance R_s. The equivalent RSJ resistance is then:

$$R_{eq} = \frac{R_n R_s}{R_n + R_s}, \tag{6.6}$$

Fluctuations in R_n are reflected as fluctuations in R_{eq} according to the sensitivity:

$$\frac{dR_{eq}}{dR_n} = \left(\frac{R_s}{R_n + R_s}\right)^2 \tag{6.7}$$

Fluctuations of the tunneling resistance δR_n as reflected in the equivalent resistance δR_{eq} is heavily attenuated depending on the relative values of R_n and R_s. Nevertheless we found that

in some of our samples the values of R_s and R_n still allowed for enough sensitivity to detect the fluctuations in R_n.

The circuit analysis is identical to the case where the junctions are superconducting as detailed in section 5.4. The inset in figure 6.3B shows the schematic of the SQUID bridge circuit with the junctions explicitly represented as a resistor. In this case, we may explicitly recast the sensitivity of the SQUID current I_{sq} with respect to fluctuations in the normal state resistance of the tunnel junction:

$$\frac{dI_{sq}}{dR_n} = \frac{I_{b1}}{R_\Sigma} \frac{dR_{eq}}{dR_n},$$
(6.8)

where R_Σ is the total resistance in the SQUID loop.

The fractional power spectral density of the SQUID input current is then related to the fractional power spectral density of the tunneling resistance as:

$$\frac{S_{R_n}}{R_n^2} = \frac{1}{2} \left(\frac{R_\Sigma}{R_n} \right)^2 \frac{1}{(dR_{eq}/dR_n)^2} \frac{S_{I_{sq}}}{I_b^2}$$
(6.9)

To perform the measurement we current bias the junctions so that they are biased at the same potential. Since the two junctions have been highly matched, this equipotential condition is achieved when the two biasing currents are approximately equal, $I_{b1} \approx I_{b2}$. Following from the equipotential biasing condition, the quiescent current through the SQUID is zero, $I_{sq} = (V_1 - V_2)/R_{std} \approx 0$, so that we are measuring fluctuations in the SQUID current about the point $I_{sq} = 0$.

Figure 6.3B shows a typical measurement of the normal state resistance in shunted junctions. In this case the gray dots are data from sample S3 taken at $T = 1.6$ K at a bias current $I_b = 75$ μA. The red dash-dot line shows a fit to the usual $1/f$ form, $S_R/R^2 = A/f + B$.

Figure 6.4 summarizes both measurements of S_{I_c}/I_c^2 for S1 to S4, and S_R/R^2 for S3 and S4. In the normal state S_{R_n}/R_n^2 is found to vary linearly with temperature similar to the dependence in S_{I_c}/I_c^2, and with a power spectral density consistent with the equivalence $S_{I_c}/I_c^2 \equiv S_{R_n}/R_n^2$ as expected from the Ambegaokar-Baratoff relation. The dashed lines
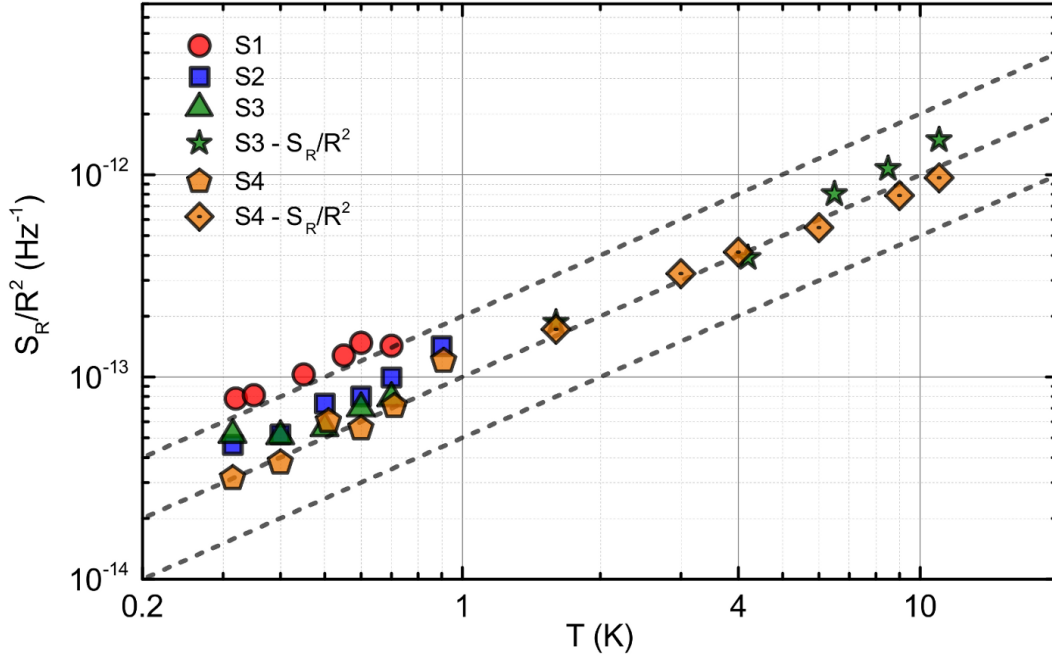
Figure 6.4: Temperature dependence of S_{I_c}/I_c^2 and S_R/R^2. Data point at $T < 1.3$ K are measurements of S_{I_c}/I_c^2 from samples S1 to S4, the data points at $T > 1.3$ K are measurements of S_R/R^2 for samples S3 and S4. The dashed lines are the average and upper/lower bounds of the resistance noise S_R/R^2 measured in unshunted junctions, shown here for comparison purposes.

in figure 6.4 are the average, lower, and upper bounds of the resistance noise measured in unshunted junctions, shown here for comparison purposes. Measurements of unshunted junctions will be discussed in the next section. We conclude that the noise magnitude and temperature dependence of S_{I_c}/I_c^2 and S_R/R^2 are consistent with each other, and reinforces the picture that critical current fluctuations arise from fluctuations of the tunneling resistance.

The data do not support the existence of excess critical current noise above the contribution from the tunneling resistance noise. Therefore we did not observe the additional contribution as proposed in Kondo-traps theories [19, 3].

6.4 Tunneling resistance noise, S_R/R^2, in unshunted Al-AlO$_x$-Al junctions

6.4.1 Experimental setup
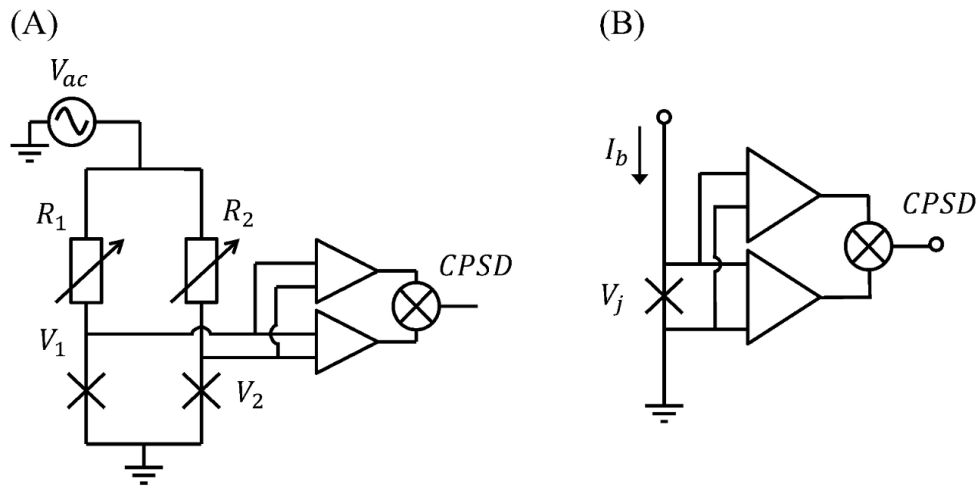
Figure 6.5: Electronic circuit for the measurement of S_R/R^2 in unshunted tunnel junctions.

Figure 6.5 shows schematics of the circuits used to measure the resistance noise S_R/R^2 in the unshunted tunnel junctions. A more detailed discussion on the circuit operation is given in chapter 5.7. The resistance noise in unshunted junctions have been measured using several variants of the measurement circuit represented in figure 6.5, although all of the circuits perform in essentially the identical manner, by current biasing the junction and amplifying the junction voltage.

The resistance bridge in figure 6.5A is identical to that used in Eroms et. al. [18] and detailed in Scofield [62] specifically for measuring the low frequency noise in resistors. For measurements in the ac-bridge geometry we fabricated two matched junctions with nominally identical tunneling resistances R and areas A. So that measurements in the bridge configuration represent an average of the two junctions having identical R and A. While the parameter matching of the junctions is not strictly necessary, the interpretation and comparison of the data is a little more complicated. The junctions are ac-biased to avoid the low frequency

noise of the voltage amplifiers. We used two lock-in amplifiers to demodulate and amplify the voltage signals, and compute the cross power spectral density (CPSD) to further reject the uncorrelated noise from the amplifiers. The modulation frequency is dictated by the sample and line impedances, but is typically in the range $1 - 3$ kHz. Measurements below the critical temperature T_c of Al were done by suppressing the superconductivity with an applied magnetic field, $B_\perp > 100$ mT.

While the ac-bridge technique allows for much more sensitive measurements of the low frequency noise, we find that in some samples with large low frequency noise (the smaller junction areas), it is sufficient to perform a single-JJ measurement as in figure 6.5B. An added benefit is that a matching junction is not required, simplifying the measurement and increasing throughput. We still ac-biased the junction to avoid the low frequency noise of the amplifier, and compute the CPSD. We have also used a dc-biasing scheme when looking at two level systems and when the bias voltage dependence of the TLS dynamics is relevant. In the case of time-domain analysis we averaged the time series traces of the two amplifiers instead of computing their CPSD.

6.4.2   Temperature dependence of the resistance noise, S_R/R^2

Figure 6.6A shows the temperature dependence of the resistance noise S_{R_n}/R_n^2 in a range of unshunted junctions, containing a range of junction areas A and resistances R. In the plot the fractional PSD has been area normalized to $A = 1$ μm^2 to allow for the comparison of a range of junction areas. In figure 6.6A only those junctions with areas large enough to produce featureless $1/f^\alpha$, $\alpha \approx 0.8 - 1.2$ have been included. These are the junctions for which the inverse area scaling holds ($S_R/R^2 \propto 1/A$), plotted in figure 6.9 and will be discussed in detail in section 6.5

The typical power spectral densities are given in figure 6.6B for $T = 1.4$ K and figure 6.6C for $T = 189$ K. The red line shows a fit to the $1/f$ functional form: $S_R/R^2 = A/f^\alpha + B$, where the fitting parameter A is used to extract the power spectral density at 1 Hz.
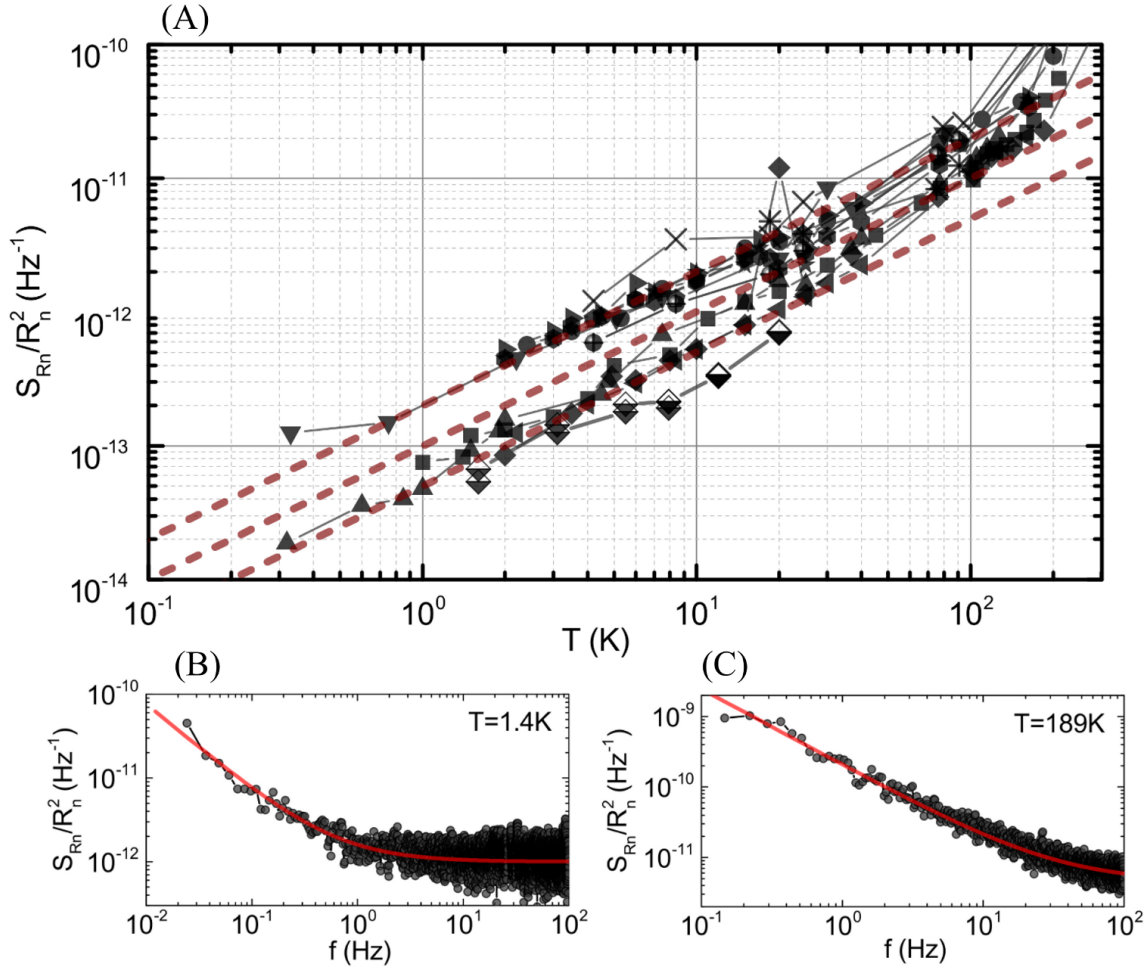
Figure 6.6: Measurement summary of tunneling resistance noise S_{R_n}/R_n^2 in unshunted double-angle evaporated Al/AlO$_x$/Al junctions.

The three dashed lines in figure 6.6A represent the average magnitude of the power spectral density, and its upper/lower bounds. We find that the average noise magnitude over all of the junctions is well described by the line:

$$\frac{S_R^{\text{av}}}{R^2} = 1 \times 10^{-13} \left(\frac{T/\text{K}}{A/\mu\text{m}^2} \right) \frac{1}{f} \ \text{Hz}^{-1}, \tag{6.10}$$

while the upper and lower bounds differ by a factor of two from this value. Part of the spread can be explained by the uncertainty in the junction sizes. We conclude that the tunneling resistance noise in unshunted junctions is consistent with the critical current and resistance

noise measured in shunted junctions (plotted in figure 6.4). The data from both shunted and unshunted junctions confirm the equivalence of critical current and resistance noise:

$$\frac{S_{I_c}}{I_c^2} \equiv \frac{S_R}{R^2} \tag{6.11}$$

6.4.3 S_R/R^2 scaling at high temperatures

We observed that at a relatively high temperature, $T \approx 150 - 200$ K, the $S_R/R^2 \propto T$ dependence is violated and the spectral density becomes a much stronger function of the temperature. This effect has also been observed in Eroms et. al. [18] and Julin et. al. [31], but has never been analyzed and discussed.

Figure 6.7A plots the temperature dependence of S_R/R^2 for two different Al-AlO$_x$-Al junctions, in the range $T \approx 1$ K to room temperature. Figure 6.7B plots the corresponding $1/f^\alpha$ exponent as a function of temperature. Note that in the range where the power spectral density is linear in T, $\alpha(T)$ is approximately, $\alpha \approx 1$. The region of hyper linear temperature dependence is accompanied by a similar increase in α.

In the Dutta-Horn model the assumption of a uniform TLS energy distribution results in a $S(\omega) \propto 1/\omega^\alpha$ power spectrum with $\alpha = 1$. In fact in most experiments the generic $1/\omega^\alpha$ noise refers to a range of the exponent, typically $\alpha \approx 0.8 - 1.4$. In this case, the Dutta-Horn model actually only requires the TLS distribution $P(E)$ to be *slowly varying* compared to $k_B T$. This leads to a relationship linking the exponent α to the temperature dependence of the power spectral density [17, 16]:

$$\alpha(\omega, T) = 1 - \frac{1}{\ln(\omega\tau_0)} \left[\frac{\partial \ln S(\omega, T)}{\partial \ln T} - 1 \right], \tag{6.12}$$

where $1/\tau_0 \sim 10^{14}$ s^{-1}, is the attempt frequency. The black line in figure 6.7 plots the shape of $\alpha(T)$ (at $\omega = 2\pi$ s^{-1}) predicted by the Dutta-Horn relation above, given the temperature dependence of the power spectral density in figure 6.7A.
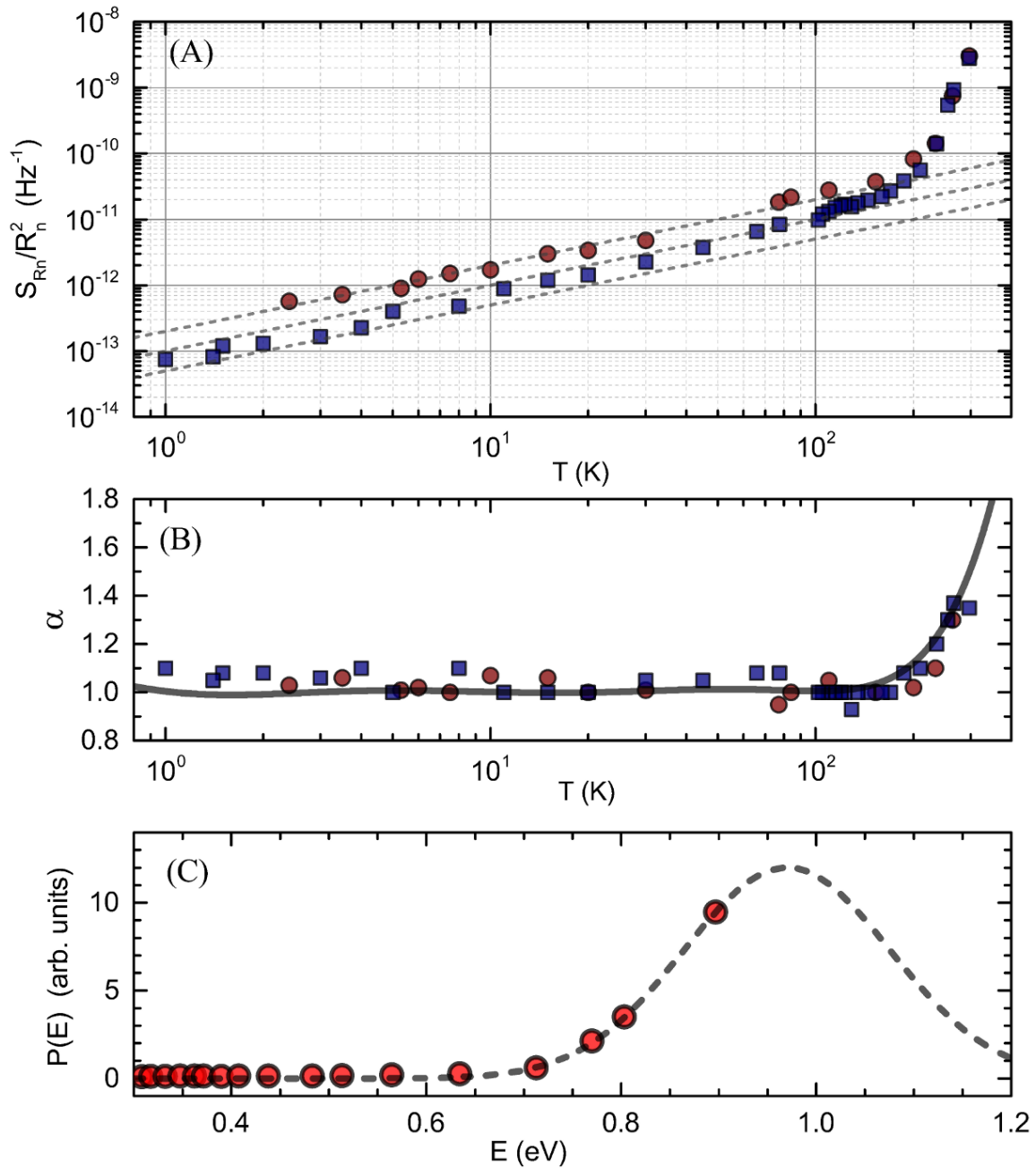
Figure 6.7: (A) Tunneling resistance noise $S_{R_n}/R_n^2(1$ Hz$)$ including the dependence at higher temperatures. A steep increase of the low frequency noise at $T \approx 150 - 200$ K. The dashed lines are the average and lower/upper bounds from measurements of the tunneling resistance noise. (B) Temperature dependence of the $1/f^\alpha$ exponent. The solid black line is the value of $\alpha(T)$ predicted by the Dutta-Horn model. (C) Red dots are the TLS energy distribution given the data in part A. The gray dashed line is a Gaussian energy distribution peaked at $E_p \approx 0.97$ eV and $2\sigma \approx 0.2$ eV, typically seen in Bi, Ag, and Cu films [16].

Note that at the high temperature range, $T \sim 100$ K it is quite likely that the junction's low frequency noise is well described by the Dutta-Horn model, which assumes thermally activated TLSs.

In the case where we have relaxed the requirement that the TLS energy distribution is strictly flat, then the power spectral density is given by the more general expression [17]:

$$S(\omega, T) \propto \frac{kT}{\omega} P(\tilde{E}),\qquad(6.13)$$

where $\tilde{E} = -kT \ln(\omega \tau_0)$, and only the Dutta-Horn kT factor has been explicitly shown. This means that the detailed dependence of the power spectral density on the frequency ω and temperature T, can reveal the energy distribution of the TLSs that cause the fluctuations. Note that the frequency range probed in the typical experiment is often limited to a few decades at most, and that the frequency only logarithmically samples the TLS energy space, thus the temperature dependence of the power spectral density gives us the most insight in this case.

In figure 6.7C, the red dots are the TLS energy distribution $P(E)$ calculated from the data in figure 6.7A. We observed an increased defect density $P(E)$, which gives clues to, and *could* be consistent with it being the tail of a peaked distribution of TLSs. The energy range in the data is obviously insufficient to positively conclude the existence, yet alone the location of a distribution peak, although it could be argued that it is unphysical for the distribution $P(E)$ to diverge, thus there has to be a peak somewhere. For comparison purposes, the gray dashed line is a Gaussian TLS energy distribution peaked at $E_p \approx 0.97$ eV with $2\sigma \approx 0.2$ eV, typically seen in Bi, Ag, and Cu films [16, 17]. Future measurements of Al-AlO$_x$-Al tunnel resistance noise should include measurements at higher temperatures to see if there is a similar peaked TLS energy distribution.

As found by Dutta and Horn [16], the energy scale $E_p \sim 1$ eV is in the order of the atomic cohesive energies, ~ 1 eV/atom. So that if the data on the noise in Al-AlO$_x$-Al junctions can support the existence of a peaked TLS distribution around $E_p \sim 1$ eV, then this could be

another indicator that the low frequency noise is caused by an atomic defect fluctuating in a disordered crystal lattice background. At low temperatures, $T \sim 1$ K, thermal activation is unlikely and the tunneling dynamics will become important in governing the properties of the low frequency noise, however the physical origin of the disorder does not have to be different from that at high temperatures.

6.4.4 Resistance noise in Nb-AlO$_x$-Nb trilayer junctions
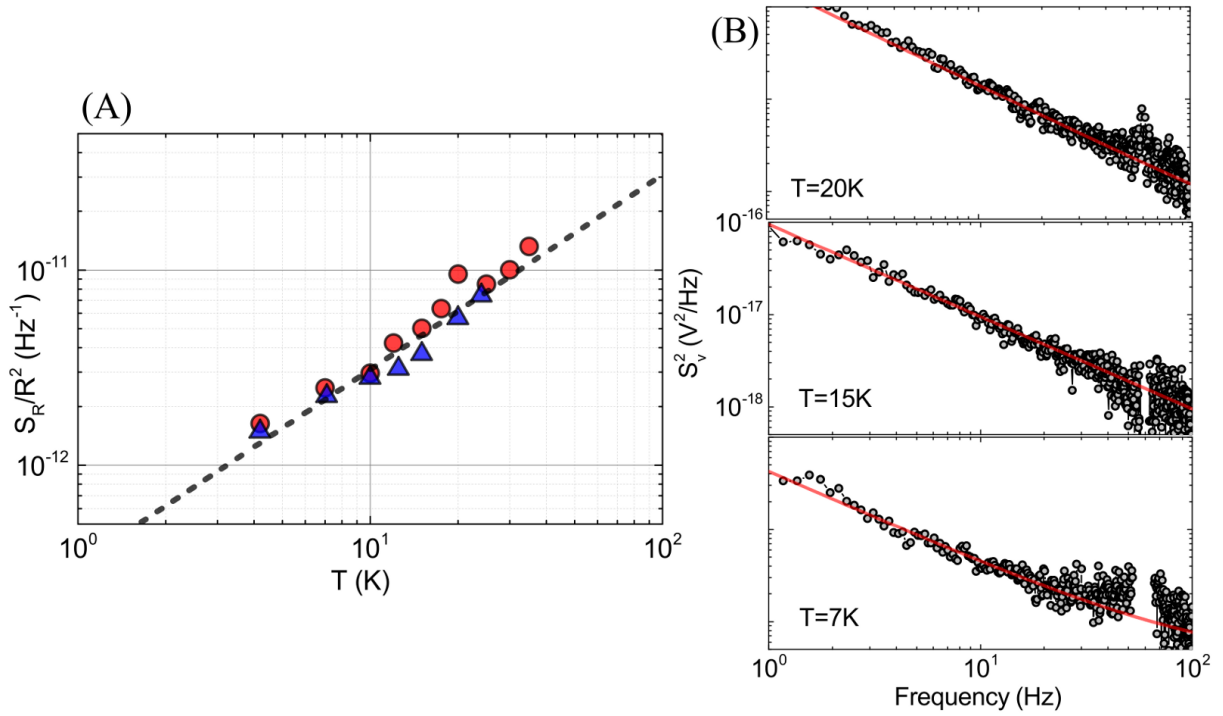
Figure 6.8: (A) Tunneling resistance noise S_R/R^2 in Nb-AlO$_x$-Nb trilayer junctions. (Red dots) J1, $A = 0.85$ μm^2. (Blue triangles) J2, $A = 0.62$ μm^2. (Dashed line) is the line $S_R/R^2 = (3 \times 10^{-13})T$ Hz^{-1}. (B) Representative power spectral densities of the tunneling resistance noise at several temperatures.

In addition to the in-house fabricated Al-AlO$_x$-Al junctions we have measured a selection of Nb-AlO$_x$-Nb trilayer junctions fabricated the group of Will Oliver at MIT Lincoln Laboratory. The measurements were done at a voltage bias of $V = 4$ mV, above the superconducting energy gap of niobium, $V > 2\Delta \approx 2.8$ meV. We measured the junctions in the single-JJ configuration

of figure 6.5B. The power spectral densities at $T = 7$, 15, and 20 K are given in figure 6.8B.

The temperature dependence of the area normalized noise power spectral density, S_R/R^2, is plotted in figure 6.8A. The red dots are measurements from Nb-J1 with $A = 0.85$ μm^2 and blue triangles are data from Nb-J2 with $A = 0.62$ μm^2. The black dotted line approximates the measured temperature dependence, given by:

$$\frac{S_R}{R^2} \approx 3 \times 10^{-13} \left(\frac{T/\text{K}}{A/\mu\text{m}^2} \right) \frac{1}{f} \ \text{Hz}^{-1} \tag{6.14}$$

While the measured noise in these Nb-junctions are on the higher end of the value previously measured in a wide range of Al-AlO$_x$-Al junctions ($S_R/R^2 \approx 1 \times 10^{-13}$ Hz^{-1} at 1 Hz, 1 K, and 1 μm^2), it is still consistent within the data scatter. Combined with the measurements of Pottorf et. al. [53] which yielded an average value of the low frequency noise in Nb-AlO$_x$-Nb junctions consistent with our measurements in Al-AlO$_x$-Al, we conjecture that the noise property is inherent to the AlO$_x$ tunnel barrier and is independent of the properties of the metal electrodes.

6.5 Breakdown of Gaussianity

6.5.1 Area scaling breakdown

Figure 6.9 plots the measured tunneling resistance power spectral density (S_R/R^2) at 1 Hz and $T = 2$ K, as a function of the junction area. At large junction areas ($A > 0.1$ μm^2) the power spectral density is proportional to $1/A$: $S_R/R^2 \propto 1/A$. At just under $A \lesssim 0.08$ μm^2, the $1/A$ scaling breaks down, reflecting a threshold at which the number of activated TLSs is no longer sufficient to integrate out a featureless $1/f^\alpha$ power spectral density. More importantly this threshold is tied to and can be used to the deduce the TLS density, which we will numerically simulate in section 6.6.2, and has been treated analytically by Garfunkel, Restle, and Weissman [22].
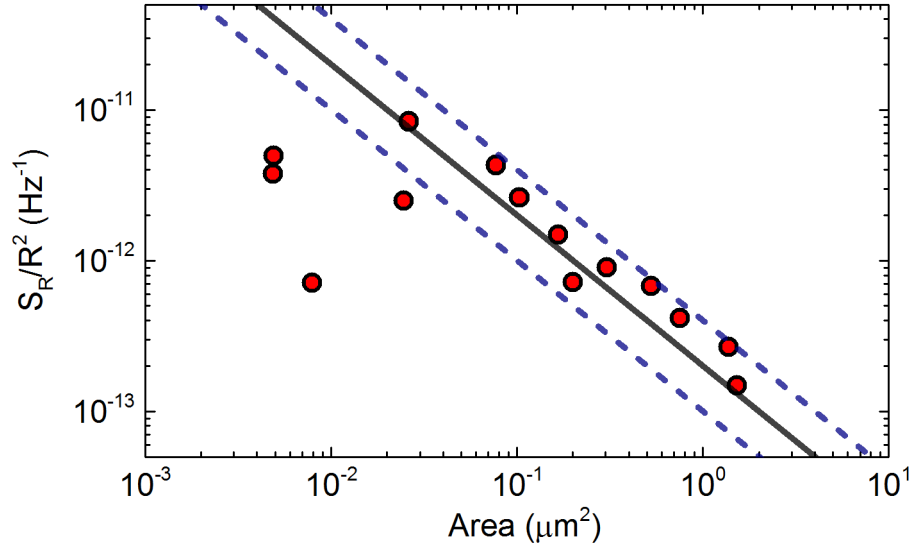
Figure 6.9: Area scaling of the tunneling resistance noise S_R/R^2. The power spectral density has not been area normalized.

At large junction areas where the power spectral density has a $1/f$ dependence, the information contained in the power spectral density is fully described by specifying only the spectral density magnitude at a single frequency, of which $f = 1$ Hz is a typical convenient choice. The breakdown of the scaling as plotted in figure 6.9 is a reflection of the noise properties from having very few activated TLSs, and the inadequacy of using the spectral density at a single frequency when the power spectral density is no longer a featureless $1/f^\alpha$.

6.5.2 Temperature dependence on the threshold of Gaussianity

In previous experiments fluctuators were often observed to have an anomalously large fractional resistance $\delta R/R$, on top of a background $1/f^\alpha$ noise [55, 57, 14]. An immediate question is to wonder if these fluctuators are representative of the ensemble that forms the $1/f^\alpha$ power spectrum, or do they represent a different noise mechanism?

In figure 6.10 we have plotted the temperature dependence of the power spectral density at $f = 1$ Hz, for a small junction $A \approx 0.008$ μm^2, and a large junction $A \approx 0.28$ μm^2 for reference. The black line plots the predicted noise line given by equation 6.2. The resistance fluctuation
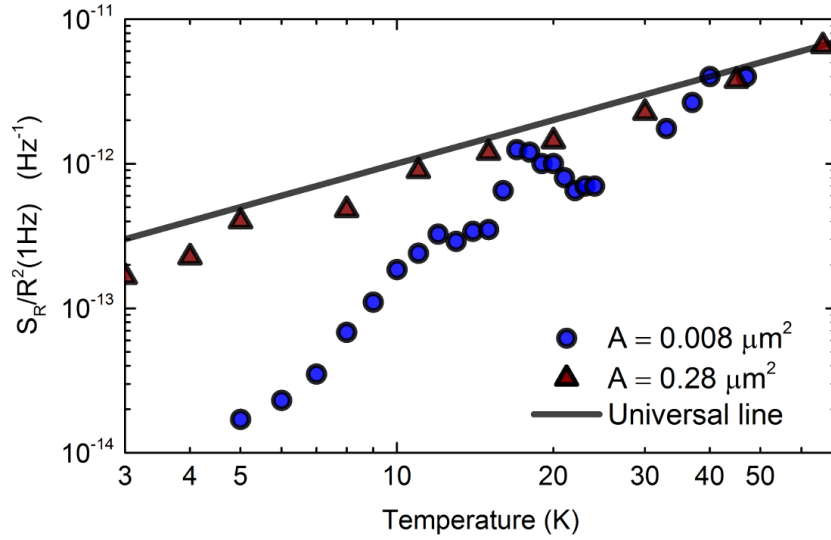
Figure 6.10: The noise spectral density at $f = 1$ Hz plotted as a function of temperature for two junctions. (Dark-red triangles) Larger junction with area $A \approx 0.28$ μm^2, the noise scaling follows the predicted universal $1/f$ temperature dependence. (Blue circles) The smaller junction with area $A \approx 0.008$ μm^2, at high temperatures the power spectral density at 1 Hz is seen to agree with the predicted universal line, however at lower temperatures the noise power spectral content drops out significantly.

of the large area junction is well described by a $1/f^\alpha$ power spectral density and follows the expected temperature dependence, $S_R/R^2 \propto T$.

For the small junction in figure 6.10 the power spectral density at low temperatures is characterized by only a few isolated Lorentzians. This loss of Gaussianity results in the loss of the generic $1/f^\alpha$ behavior described by $S \propto T/A$ (equation 6.2). Instead, in order to fully describe the temperature evolution of the PSD we are required to know the specific instances of the randomly distributed TLSs. We observed that at high temperatures the power spectral density is well predicted by the universal line, however it diminishes rapidly as the temperature is lowered following a more complicated temperature evolution. This strongly suggests that the Lorentzians observed at low temperatures are the remainder of the ensemble that form the $1/f$ noise at higher temperatures, and that they are not unrelated TLS species that became activated.

Figure 6.11A plots the temperature evolution of the fractional power spectral density for the
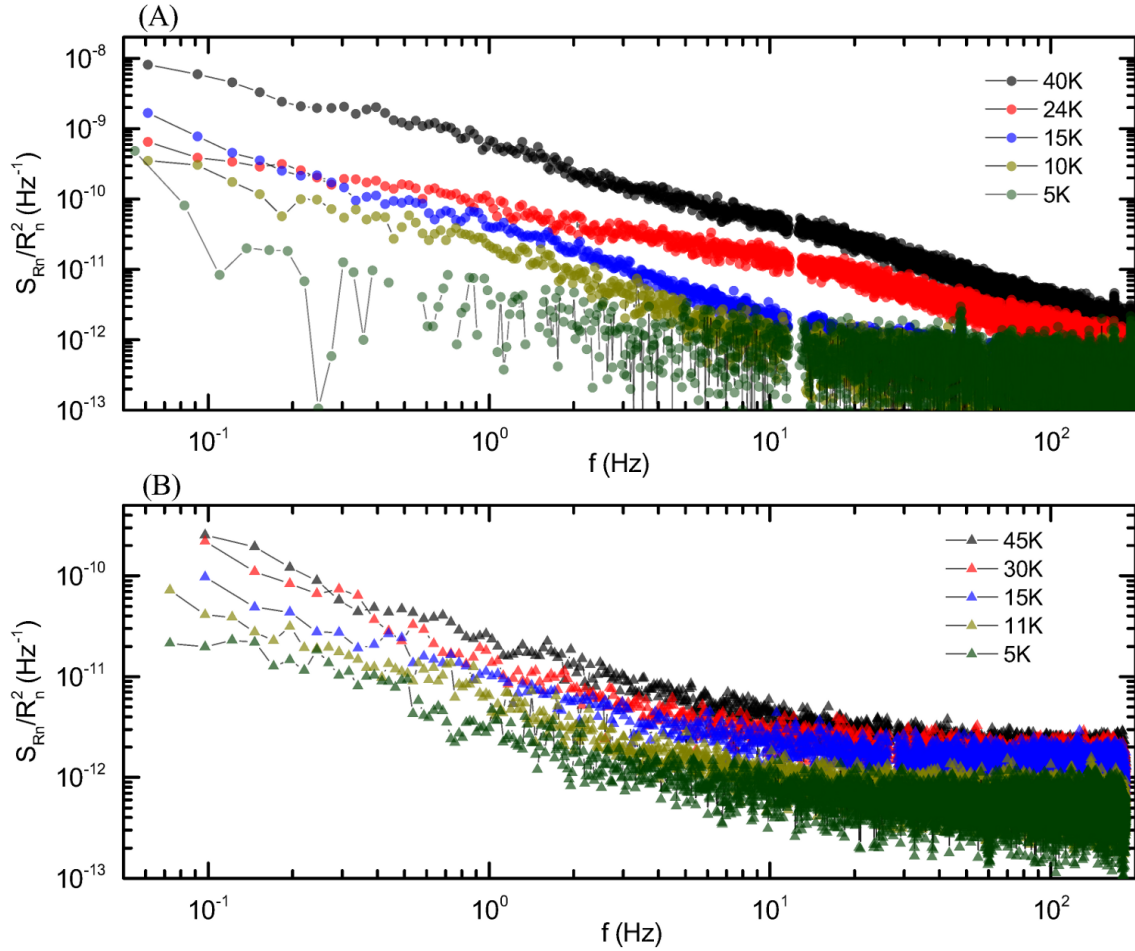
Figure 6.11: The tunneling resistance noise power spectral density, S_R/R^2 for (A) A small $A \approx 0.008$ μm^2 junction. (B) Large junction $A \approx 0.28$ μm^2

small junction with $A \approx 0.008$ μm^2. The temperature evolution of the power spectral density is much more complex in comparison to the temperature evolution of the large junction given in figure 6.11B with $A \approx 0.28$ μm^2. An even more complex temperature evolution can be seen in the power spectral density of a different junction, also with $A \approx 0.008$ μm^2, shown in figure 7.2.

The large ($A \approx 0.28$ μm^2), junction has a featureless $1/f^\alpha$ power spectral density for the temperature ranges shown, and the temperature evolution is predictable following a linear T-dependence, $S_R/R^2 \propto T$. More importantly the linear T-dependence does not depend on the

frequency ω. On the other hand the small junction temperature dependence follows a much more complex $\partial S(\omega, T)/\partial T$ evolution that explicitly depends on the frequency ω.

6.5.3   TLS activation and deactivation
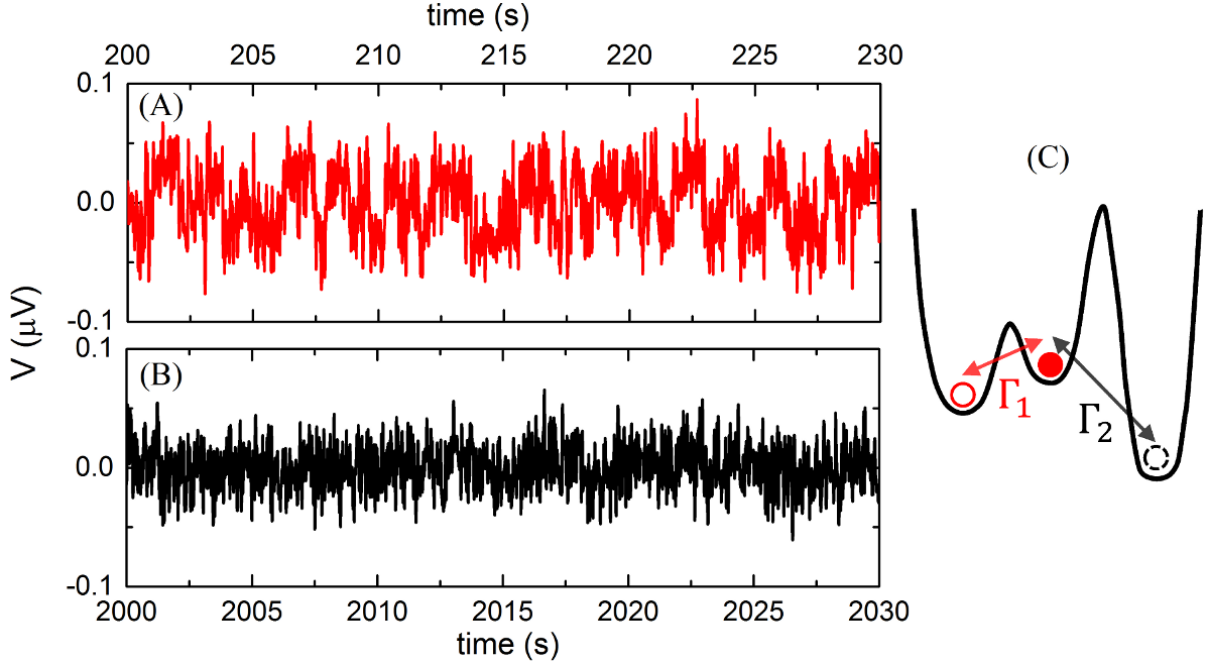
Figure 6.12: (A-B) Freezing out of an active TLS. The freeze-out event occurred spontaneously while in the middle of a long (2hr+) time trace at a constant voltage bias, $V_b = 3$ mV, $T = 6$ K. (C) Effective three-well potential with a third isolated ground state creating a rare switching event with effective rate Γ_2.

We have also occasionally observed the freezing out of TLSs that leaves the junction with very low residual noise. Figure 6.12A shows a time trace at $T = 6$ K at a bias voltage $V_b = 3$ mV. Early in the trace the junction's tunneling resistance is characterized by an activated two level system (figure 6.12A). However later at some time $t \approx 2000$ s, the fluctuator spontaneously disappears (figure 6.12B), which occurred during a single time capture event, with the temperature and voltage bias kept constant.

We conjecture that this freeze-out event reflects the fact that the fluctuators are actually located within a much more complex potential energy landscape that is only *effectively* a local
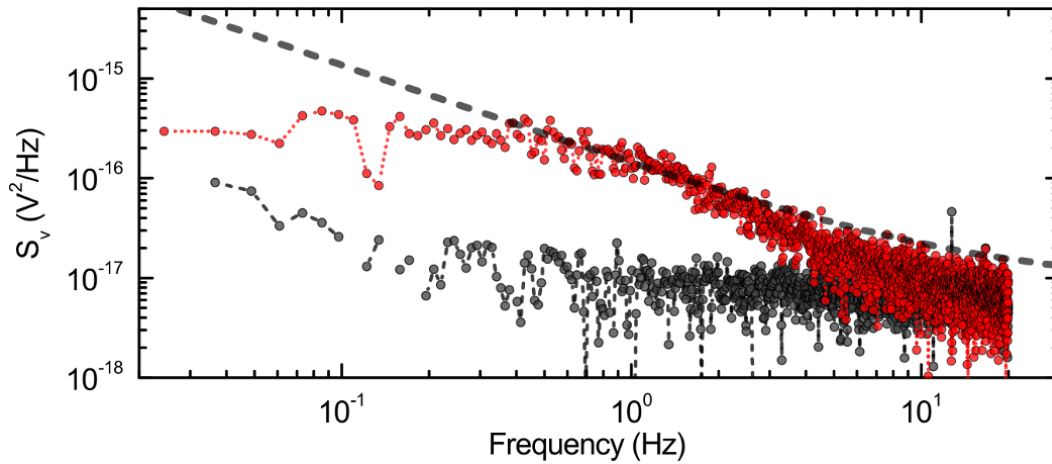
Figure 6.13: Freezing out of an active TLS. The freezing out even occurred spontaneously while in the middle of a long (2hr+) time trace at a constant voltage bias.

double-well potential. There may exist a third (or more) localized potential well separated by a large potential barrier, such that a tunneling event into this third ground state is rare. One such conjecture is sketched in figure 6.12C. Note that Garfunkel and Weissmann [22, 23] have observed similar non-two-state behavior in the atomic motion in amorphous C-Cu and Si-Au

Figure 6.13 shows the power spectral density of the tunneling resistance (S_{R_n}/R_n^2). The red dots show the PSD of the active fluctuator, note that the dashed gray line plots out the universal noise line predicted for this particular junction which accurately predicted the power spectral density at the corner frequency of the TLS. The gray dots are the power spectral density with the fluctuator frozen-out. Note that the result is that the noise is at least one order of magnitude lower than that predicted by the universal noise formula.

6.6   Defect density estimation

The TLS density can be estimated from two independent sources: 1. The $1/f$ noise power magnitude in large junctions, and 2. The deviations from featureless $1/f$ power spectral density in smaller junctions. As will be shown, the $1/f$ noise power magnitude depends on both the TLS density σ_0 and the effective strengths δA. However the 'bumpiness' of the power spectrum

depends only on the TLS density, thus combining these two information sources we are able to give an estimate for both the TLS density and the effective strengths.

6.6.1   Defect density from $1/f^\alpha$ noise

The spectrum due to a single TLS with a variance σ^2 is given by [38, 40]:

$$S_i = 4\sigma^2 \ \frac{\tau_i}{1+\omega^2\tau_i^2} \tag{6.15}$$

In the tunneling TLS model, the variance of the TLS is $\sigma^2 = (1/4)(\delta R)^2\text{sech}^2(E/2kT)$, where $E = \sqrt{\Delta^2 + \Delta_0^2}$ is the energy level splitting, and δR is the signal difference between the two TLS configurations (section 3.2). The total noise power can thus be evaluated through the integral:

$$S(\omega) = (\delta R)^2 \int \ \frac{\tau(\Delta,\Delta_0)}{1+\omega^2\tau^2(\Delta,\Delta_0)} \ \text{sech}^2(E/2kT) \ AP(\Delta,\Delta_0) \ d\Delta \ d\Delta_0, \tag{6.16}$$

where the joint TLS distribution $P(\Delta,\Delta_0)$ is assumed to be uniformly distributed in the asymmetry energies Δ and the tunneling parameter λ, $(\Delta_0 = \hbar\omega_0 e^{-\lambda})$ [81]:

$$P(\Delta,\lambda) \ d\Delta \ d\lambda = P_0 \ d\Delta \ d\lambda, \tag{6.17}$$

$$P(\Delta,\Delta_0) \ d\Delta \ d\Delta_0 = \frac{P_0}{\Delta_0} \ d\Delta \ d\Delta_0, \tag{6.18}$$

and the one-phonon relaxation rate in the tunneling TLS model is given by [49, 51, 81]:

$$\Gamma = \frac{1}{\tau} = \left(\sum_\alpha \frac{\gamma_\alpha^2}{v_\alpha^5}\right) \left(\frac{E\Delta_0^2}{2\pi\rho\hbar^4}\right) \coth\left(\frac{E}{2k_BT}\right), \tag{6.19}$$

where $E = \sqrt{\Delta^2 + \Delta_0^2}$. The TLS distribution can also be expressed in terms of more useful

quantities, E and τ, which has the form [13]:

$$P(E, \tau) = \frac{P_0}{2\tau} \frac{1}{\sqrt{1 - \tau_{\min}(E)/\tau}}, \tag{6.20}$$

where $\tau_{\min}(E)$ is the minimum relaxation time at energy $E = \Delta_0$ corresponding to the degenerate TLS double-well configuration, at the given energy E. The total noise power can thus be estimated [13]:

$$S(\omega) \approx \frac{(\delta I)^2 A P_0}{2} \int_0^\infty dE \ \text{sech}^2(E/2kT) \int_0^\infty \frac{d\tau}{1 + \omega^2 \tau^2} \tag{6.21}$$

$$\approx \frac{\pi}{2} (\delta I)^2 A P_0 kT \frac{1}{\omega} \tag{6.22}$$

$$S(f) \approx \frac{1}{4} (\delta I)^2 A P_0 kT \ \frac{1}{f}, \tag{6.23}$$

where the factor $\sqrt{1 - \tau_{\min(E)}/\tau}$ has been ignored because $\tau_{\min}/\tau \ll 1$ in the relevant integration region, following Constantin and Yu [13]. Note also that this leaves the TLS distribution with the approximate form $P(\tau) \propto 1/\tau$ which is the required form to produce a $1/\omega$ spectrum. The one kT factor comes from the $\text{sech}^2(E/2kT)$ integration, which selects the TLS energies with thermodynamically allowed transitions.

Using the definition of the TLS distribution in equation 6.20, the TLS density, n, per μm^2 in the junction area, per Kelvin spread in the TLS energy E per factor e in the TLS rates τ, is given by:

$$n = \frac{P_0}{2} \int_0^{1\text{K}} dE \int_{\tau_0}^{e\tau_0} \frac{d\tau}{\tau} = \frac{P_0}{2}, \tag{6.24}$$

here the relationship $P_0 \equiv 2n$ is a result of the definition of the distribution, $P(E, \tau) \approx P_0/2\tau$. We have retained this definition to be consistent with the notation in the literature of glassy insulators [51, 49, 13]. It is sometimes useful to integrate out the distribution over the TLS lifetimes τ to obtain the TLS density over all TLS lifetimes:

$$\sigma_0 = \frac{P_0}{2} \int_{\tau_{\min}}^{\tau_{\max}} \frac{d\tau}{\tau} = (12 \ln 10)n \tag{6.25}$$

where we have used the notation n to mean the TLS density per μm^2 in the junction area, per Kelvin spread in the TLS energy E, per factor e in the TLS rates τ, and σ_0 denotes the TLS density n integrated over the range of TLS lifetimes, $\{\tau_{\min}, \tau_{\max}\}$. Here we have used 12 decades of TLS lifetimes as the integration limits, which covers the frequency cutoffs: $f = 1$ mHz to $f = 1$ GHz. It is unclear what the appropriate frequency cutoffs should be, because in a typical measurement the upper frequency cutoff is typically obscured by the Johnson-Nyquist noise floor or by the noise floor of the instrumentation. While the lower cutoff is typically limited by the constraint of a finite experiment duration. However the logarithmic dependence in equation 6.25 makes it a very weak function of the choice of cutoff frequencies.

It follows that the number of thermally active TLSs, N^*_{TLS} is given by:

$$N^*_{TLS} = \int P(E, \tau) \, d(E, \tau) = \frac{P_0}{2} \int_0^\infty \mathrm{sech}^2(E/2kT) \, dE \int_{\tau_{\min}}^{\tau_{\max}} \frac{d\tau}{\tau} = (12 \ln 10) P_0 kT \quad (6.26)$$

Finally, using the relationship $\delta I = (\delta A/A)I$, where δA is a parameter describing the coupling strength between the TLS and the junction's critical current, the fractional noise PSD can be estimated as:

$$\frac{S_{I_c}}{I_c^2} \approx \frac{1}{4} (\delta A)^2 P_0 \frac{kT}{A} \frac{1}{f}, \quad (6.27)$$

where here the TLS strength $(\delta A)^2$ represents the averaged value $\langle (\delta A)^2 \rangle$ of some underlying distribution. While the detail of the distribution is not important in this $1/f$ ensemble averaged case, we will assume a Gaussian distribution later in our simulation of the TLSs.

Comparing to our inferred universal noise formula for the $1/f$ noise in Al/AlO$_x$/Al junction (equation 6.2):

$$\frac{S_{I_c}}{I_c^2} = 1 \times 10^{-13} \frac{(T/\mathrm{K})}{(A/\mu\mathrm{m}^2)} \frac{1}{f} \mathrm{Hz}^{-1}, \quad (6.28)$$

we obtain an estimate of the TLS density and strengths:

$$\langle (\delta A)^2 \rangle P_0 \approx 4 \times 10^{-13}, \quad (6.29)$$

where $P_0 \equiv 2n$ is twice the TLS density per μm^2 in junction area, per factor e in TLS rate, per 1 K in TLS energy spread, and $\langle (\delta A)^2 \rangle$ is given in units of $(\mu m^2)^2$.

As will be detailed in the next section, we are able to obtain an estimate for the density $P_0 \equiv 2n$ from the breakdown of the featureless $1/f$ spectral shape due to a finite TLS ensemble size. The estimated TLS density is:

$$n \approx 2.53 \ \mu m^{-2} K^{-1} e^{-1}, \tag{6.30}$$

Using this estimated density, we deduce a value for the average TLS strength:

$$\langle \delta A^2 \rangle \approx (0.30 \ nm^2)^2, \tag{6.31}$$

that is a root-mean-square value, $\delta A_{RMS} \approx 0.30 \ nm^2$.

6.6.2 The few TLSs limit

Analytical result for the analysis of the spectral variance

We have detailed in previous sections the experimental observation that at small junction areas and low temperatures, the relatively few activated TLSs fail to integrate out a featureless $1/f$ spectral shape. Instead the power spectral density is characterized by several overlapping Lorentzians giving rise to a 'bumpy' $1/f$-like spectral shape. Weissman et. al. [22, 23] showed that the TLS density can be deduced by quantifying the variations in the spectral shape. In this section we will show the TLS density estimation following the analytical result of Weissman et. al. [22, 23], as well as the results from directly simulating the TLS ensembles.

For noise processes connected to the $1/f$ power spectral density, it is often convenient to evaluate the quantity $\omega S(\omega)$, where $S(\omega)$ is the noise power spectral density of the system and ω is the angular frequency. For a pure $1/f$ noise, $S(\omega) = A/\omega$, therefore the quantity $\omega S((\omega) = A$, is a constant and appears as a horizontal line in plots as a function of the

frequency ω.

More generally for spectral shapes $S(\omega)$ that deviate from the pure $1/\omega$, we can compute the averaged quantity $\langle \omega S \rangle$, which represents a fit to a pure $1/\omega$ spectral shape. The spectral variation from this average can thus be defined by the quantity:

$$\omega \delta S = \omega S(\omega) - \langle \omega S \rangle, \tag{6.32}$$

and the spectral variance $\langle (\omega \delta S)^2 \rangle$ can thus be calculated as:

$$\langle (\omega \delta S)^2 \rangle = \langle (\omega S)^2 \rangle - \langle \omega S \rangle^2 \tag{6.33}$$

Weissman et. al. [22, 23] showed that the fractional spectral variance is related to the TLS density as:

$$\frac{\langle (\omega \delta S)^2 \rangle}{\langle \omega S \rangle^2} = \frac{1}{\pi^2 n}, \tag{6.34}$$

where n is the TLS density per factor e in rate per kT in energy per junction area A. At large TLS densities, the spectral variance is small and the power spectrum approaches that of a featureless $1/\omega$ spectrum.

Note that the averaging $\langle \ \rangle$ is strictly over the entire range of TLS lifetimes τ, which typically spans about 12 decades in frequency. However in our typical experiment the observable range typically spans only about 2 to 3 decades in frequency, which inevitably leads to some estimation errors. Therefore in our estimation we averaged the results from spectra taken at several different temperatures in order to average out some of the effects of a narrow observation bandwidth. The averaging was also performed so that each frequency octave is weighted equally (logarithmic), as opposed to equal weighting per frequency window (linear).

We have calculated the spectral variations from a small junction shown in figure 7.2, and averaged over spectra taken at several different temperatures. Using the analytical result in equation 6.34, we find an averaged TLS density, $n \approx 2.0$ per μm^2 in the junction area, per Kelvin in the TLS energy E, per factor e in the TLS rate τ, or $\sigma_0 \approx 55.2$ μm^{-2} K^{-1}.
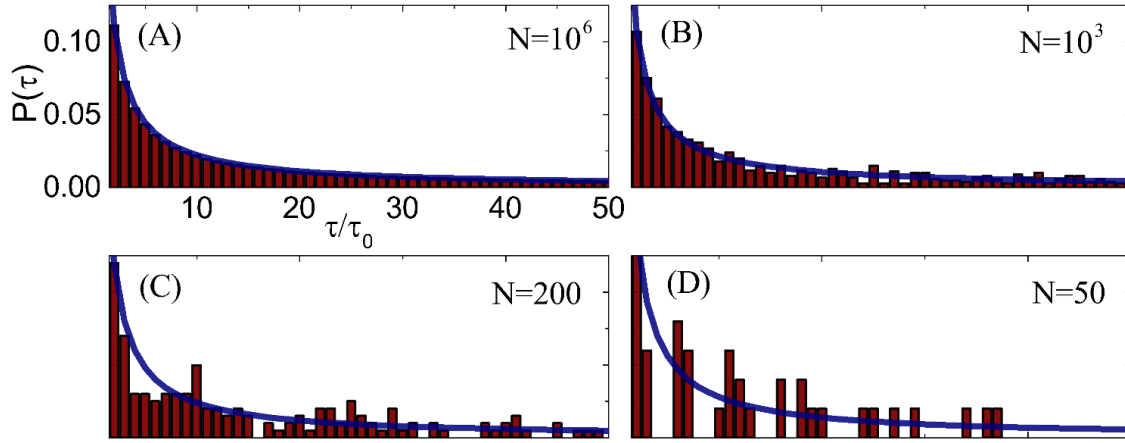
Figure 6.14: Simulated discrete distribution of TLS lifetimes τ_i for sample sizes: (A) $N = 10^6$. (B) $N = 10^3$. (C) $N = 200$. (D) $N = 50$. The blue solid line is the continuous distribution function $P(\tau) \propto 1/\tau$.

Simulated TLS ensembles

We now seek to directly simulate the TLS ensembles in order to verify the analytical result of equation 6.34 and replicate the data on the observed $1/A$ area scaling breakdown in the small junction limit (section 6.5). The data plotted in figure 6.9 shows an on-set of the $1/A$ area scaling breakdown in the approximate region $A \approx 0.04 - 0.08~\mu\mathrm{m}^2$ at $T \approx 2~K$. We will now show by simulating the TLS ensembles, that the deduced TLS density is consistent with this threshold for the breakdown of the $1/A$ scaling.

The TLS ensemble is simulated by summing the Lorentzian contribution of each TLS:

$$S_I(f) = \sum_n (\delta I_n)^2 \mathrm{sech}^2(E_n/2kT) \frac{\tau_n}{1 + 4\pi^2 f^2 \tau_n^2}, \tag{6.35}$$

where the TLSs are distributed in energy E_n and lifetime τ_n according to the distribution: $P(E, \tau) = P_0/2\tau$. The amplitudes δI_n depends on the area of the junction, $\delta I_n = (\delta A_n/A)I$, so that the fractional noise S_I/I^2 can be expressed as:

$$\frac{S_I}{I^2} = \frac{1}{2\pi A^2} \sum_n (\delta A_n)^2 \mathrm{sech}^2(E_n/2kT) \frac{f_{c,n}}{f_{c,n}^2 + f^2}, \tag{6.36}$$

where δA_n is the characteristic area of the TLS which we will approximate to have a Gaussian distribution, A is the junction area, and $f_{c,n}$ is the corner frequency, $f_c = 1/2\pi\tau$, of the $n-$th TLS. We can then simulate an ensemble of TLSs having a collection of lifetimes $\{\tau_n\}$ distributed as $P(\tau) \approx P_0/2\tau$ and construct the ensemble total power spectral density through the summation in equation 6.36.

For the simulation it is assumed that the TLS lifetimes are distributed over 12 decades in $\{\tau_{\min}, \tau_{\max}\}$, and a TLS energy range $\{0, 6kT\}$. For TLSs with energies $E > 6kT$, the thermodynamic factor is $\text{sech}^2(E/2kT) < 0.01$, therefore those TLSs with $E > 6kT$ contributes very little to the total noise and can be left out from the simulation. In fact the integration $\left[\int_0^{6kT} \text{sech}^2(E/2kT)\ dE\right] / \left[\int_0^\infty \text{sech}^2(E/2kT)\ dE\right] \approx 0.995$, thus simulating only those TLSs with $E < 6kT$ gives at most a 0.5% error.

The number of TLSs with, $0 < E < 6kT$ and $\tau_{\min} < \tau < \tau_{\max}$ is given by: $N_{TLS} = (12\ln 10)(6T)An$, where n is the TLS density per μm^2 per Kelvin spread in E per factor e in τ. In the simulation each of these TLSs are then assigned a lifetime τ distributed as in figure 6.14 and an energy E uniformly distributed over $\{0, 6kT\}$. The fractional quantity in N_{TLS} is taken to be the probability of having an active TLS. For example an ensemble with $N_{TLS} = 100.78$ is taken to have 100 active TLSs with a 0.78 probability of having an additional active TLS. Similarly, a small ensemble with $N_{TLS} = 0.1$ is interpreted as having a 0.1 probability of having an active TLS (0.9 probability of having none).

Figure 6.14 shows a histogram of the TLS lifetimes τ_n for a simulated collection of N TLSs. The solid blue line is the continuous probability distribution function, $P(\tau) \propto 1/\tau$. In figure 6.14A, in the limit of large N the discrete probability density approaches that of the continuous case. Figures 6.14B, C, and D shows an instance of the $\{\tau_n\}$ discrete distribution for a finite sample size $N = 1000,\ 200,\ \text{and}\ 50$, respectively.

The fluctuator strengths δA_n describes the coupling of the fluctuator to the junction tunneling resistance. The most likely mechanism is that the fluctuator couples through its dipole moment $\mathbf{P}$ to produce fluctuations in the tunneling potential of the AlO$_x$ dielectric, following

the fluctuating dipole theory of Yu et. al. [13]. Consequently δA is randomly distributed according to a distribution of the dipole strengths $|\mathbf{P}|$ and orientations θ. The most reasonable approximation is to distribute δA to a central Gaussian distribution with a variance $\sigma_{\delta A}^2$. The second-moment of the central Gaussian distribution gives, $\langle(\delta A)^2\rangle = \sigma_{\delta A}^2$.

Figure 6.15 shows an example of the simulated total ensemble power spectral density for several junction areas. The PSDs were calculated at $T = 2$ K, with a TLS density of $n = 2.53$ μm$^{-2}K^{-1}e^{-1}$ ($\sigma_0 \approx 69.7$ μm^{-2}K^{-1}), and a Gaussian distribution of δA with $\sigma_{\delta A} = 0.3$ nm^2. For large area junctions the ensemble power spectral density is well described by a featureless $1/f^\alpha$ spectrum with $\alpha \approx 1$. The appearance of Lorentzian bumps and evolution towards the power spectrum of only a few Lorentzians are clearly seen as the junction area is made smaller.

In figure 6.16 the power spectral density at $f = 1$ Hz is plotted as a function of the junction area A at $T = 2$ K, $n = 2.53$ μm^{-2}K$^{-1}e^{-1}$, and a Gaussian distribution of the TLS strengths δA with $\sigma_{\delta A} = 0.3$ nm^2. The blue circles and dark yellow triangles in figure 6.16 represent two separate trial runs. For large area junctions the simulation reproduces the expected $S \propto 1/A$ area dependence. Somewhere in the approximate region of $A \approx 0.04-0.08$ μm^2, the $1/A$ scaling breaks down due to the insufficient number of TLSs failing to sum out to a $1/f^\alpha$ spectrum. As a guide, the red dashed line plots out the line $S_R/R^2 \propto 1/A$. This simulated area scaling breakdown, with the onset in the approximate region, $A \approx 0.04 - 0.08$ μm^2, is consistent with the experimental observation shown in figure 6.9.

Figure 6.17 shows examples of the simulated power spectral densities for several junction areas, $A = 0.05$, 0.5, 5, and 50 μm^2. The simulation was performed at $T = 2$ K, $n = 2.53$ μm^{-2}K$^{-1}e^{-1}$, and a central Gaussian distributed fluctuator strengths δA with $\sigma_{\delta A} = 0.3$ nm^2. The simulated power spectral densities are plotted in terms of $fS_R(f)/R^2$ as a function of f. In this plot a pure $1/f$ power spectral density appears as a horizontal line. The left and right panels in figure 6.17 represent two separate trial runs with identical simulation parameters. The black lines are the simulated power spectral densities, while the dashed red
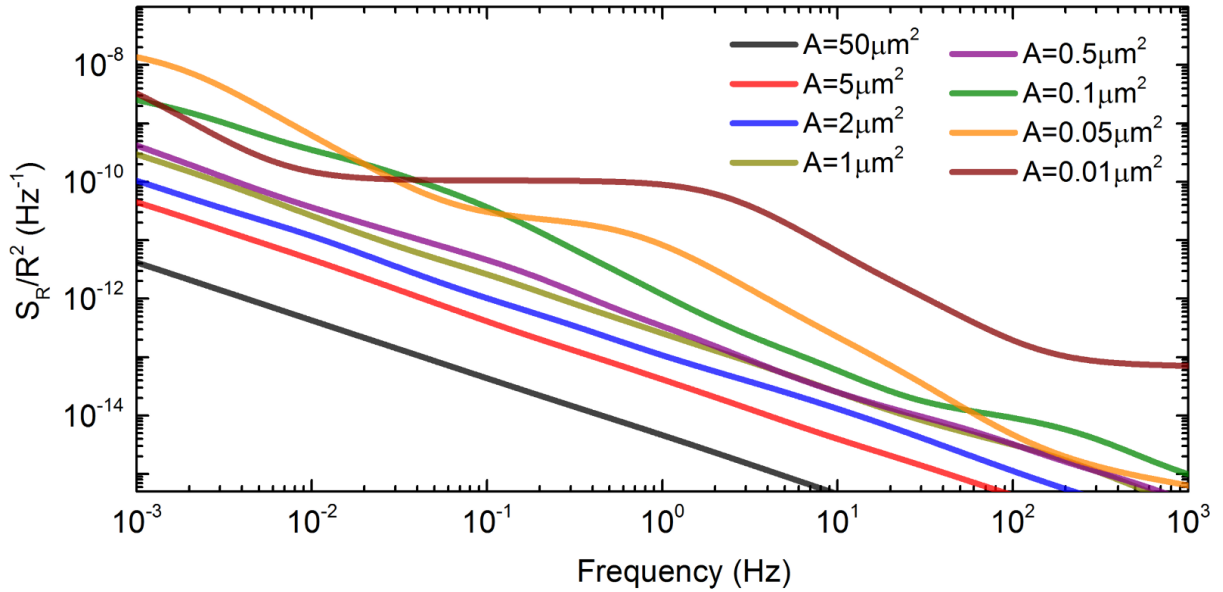
Figure 6.15: Simulated noise power spectral density S_R/R^2 , for an ensemble of TLSs with density $n = 2.53 \ \mu m^{-2}K^{-1}e^{-1}$ at $T = 2$ K, shown for several different junction areas $A = 50, \ 5, \ 2, \ 1, \ 0.5, \ 0.1, \ 0.05, \ \& \ 0.01 \ \mu m^2$. The ensemble averaged PSD is a featureless $1/f^\alpha$ noise with $\alpha \approx 1$ at 'large' junction areas, but decompose into distinct Lorentzians in the small area limit.

lines are the averaged value $\langle f S_R(f)/R^2 \rangle$, which represents the fit to a pure $1/f$ spectral shape. Note that at large junction areas (many TLSs), the simulated spectral shape is well described by a pure $1/f$ spectral shape. At smaller junction areas (few TLSs), the variation from the pure $1/f$ spectral shape is more pronounced, as well as a more pronounced sample-to-sample variation.

Figure 6.18 shows the simulated fractional PSD variance, $\langle (\omega \delta S)^2 \rangle / \langle \omega S \rangle^2$, as a function of the TLS density n per kT spread in E per factor e in the lifetimes τ. As long as the TLS density is not too small, we recover a relationship close to the analytical result of equation 6.34:

$$\frac{\langle (\omega \delta S)^2 \rangle}{\langle \omega S \rangle^2} \approx \frac{1.3}{\pi^2 n}, \tag{6.37}$$

which differs from the analytical result by a factor of 1.3. Each simulated data point in figure 6.18 is a result of $N = 500$ averaging. The tapering at low TLS densities correspond to
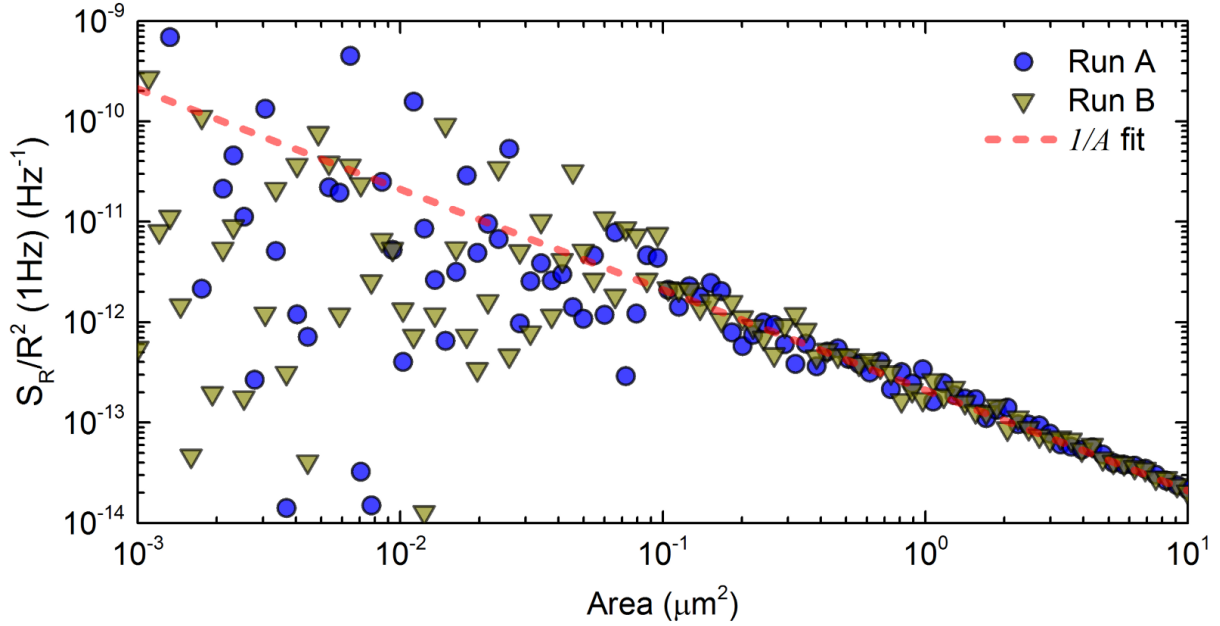
Figure 6.16: Area scaling of the simulated power spectral density at $f = 1$ Hz, simulated at $T = 2$ K, $n = 2.53$ μm$^{-2}K^{-1}e^{-1}$. The result is consistent with experimental data in figure 6.9, which shows a breakdown in the $\propto 1/A$ area scaling in the vicinity of $A \approx 0.04 - 0.08$ μm^2. The red dashed line shows a $S \propto 1/A$ scaling.
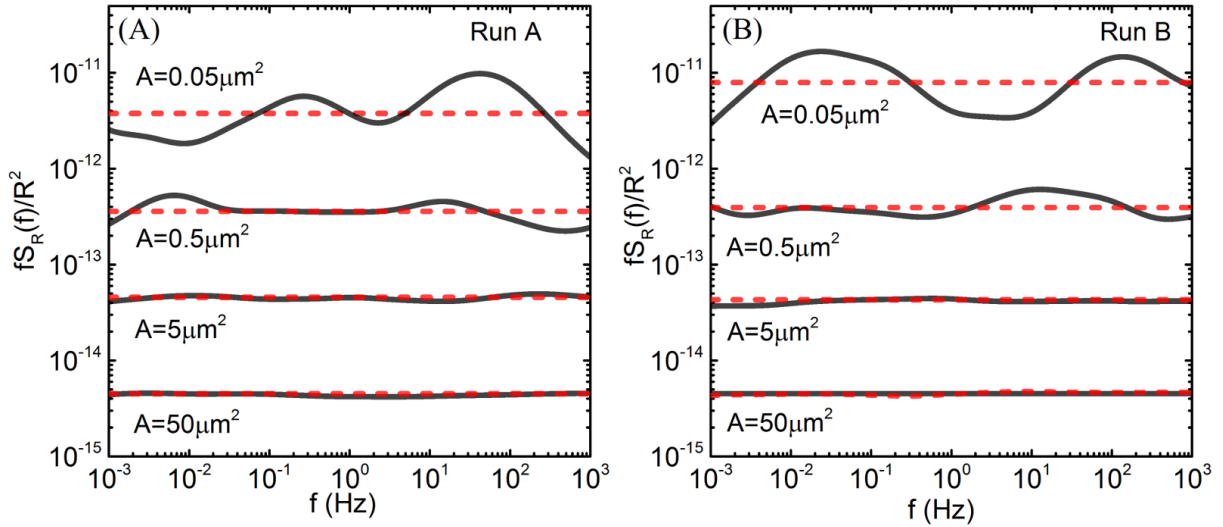
Figure 6.17: The simulated power spectral density at $T = 2$ K, $n = 2.53$ μm$^{-2}K^{-1}e^{-1}$, $\sigma_{\delta A} = 0.3$ nm^2, and shown for several junction areas, $A = 0.05, 0.5, 5,$ and 50 μm^2. The black lines plot the simulated fractional power spectral densities, $fS_R(f)/R^2$, while the dashed red lines plot the averaged value $\langle fS_R(f)/R^2 \rangle$, representing a fit to a pure $1/f$ power spectral shape. The left and right panels are two different simulation runs with identical parameters, (A) Simulation Run A (B) Simulation Run B.
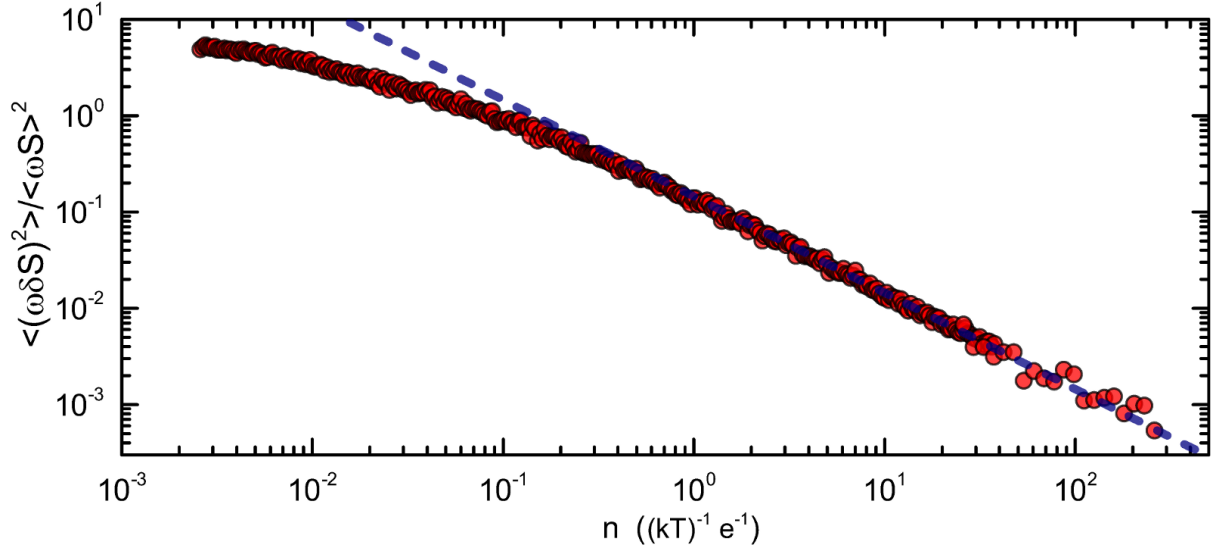
Figure 6.18: The simulated PSD fractional variance, $\langle(\omega\delta S)^2\rangle/\langle\omega S\rangle^2$, as a function of the TLS density n per kT spread in E per factor e in the lifetimes τ.

the threshold where there is less than one thermally active TLS per octave in frequency, which corresponds to $n \approx 0.7$.

Using the result of the simulation, we deduce a slightly higher value of the TLS density, $n \approx 2.53$ μm^{-2}K$^{-1}e^{-1}$, or $\sigma_0 \approx 69.7$ μm^{-2}K^{-1}. In figure 6.16 it has been shown that a Gaussian distribution of the fluctuator strength δA with a variance $\sigma_{\delta A}^2 \approx (0.3 \text{ nm}^2)^2$ reproduces the correct $1/f$ noise power magnitude, $S_R/R^2 \approx 1 \times 10^{-13}$ Hz^{-1} for a junction area 1 μm^2 at $T = 1$ K.

6.7 Implication of the TLS density

6.7.1 Comparison of n to other systems

Glassy insulators

The tunneling two level system model was originally proposed to explain the anomalous low temperature heat capacity of glassy insulators [2, 50]. It was found that at low temperatures the

heat capacity in glassy insulators vary linearly with temperature as opposed to the expected $C \propto T^3$ from the Debye specific heat. It was found that the anomalous low temperature specific heat in these amorphous solids can be explained by a distribution of tunneling two level systems, $P(E, \tau) \approx P_0/2\tau$, with $P_0 \approx 1 \times 10^{45}$ J^{-1}m^{-3} [10, 51]. In comparison, our estimated TLS density from junction noise, assuming a dielectric thickness $t \approx 1$ nm, corresponds to $P_0 \approx 3.7 \times 10^{44}$ J^{-1}m^{-3}, consistent with the value from the anomalous specific heat in glasses.

Avoided level crossings at the qubit frequency

Avoided level crossings have been observed in the energy spectroscopy of various qubit systems [43, 65, 46, 52], these are due to the coherent coupling of the qubit to spurious two level systems at the qubit frequency.

Analysis of the density of these avoided level crossings yielded a TLS density, $\sigma \approx 0.5\ \mu$m^{-2}GHz^{-1} $\approx 10.4\ \mu$m^{-2}K^{-1} [43, 65], which is consistent with our estimated density of TLSs from the low frequency noise in tunnel junctions, $\sigma_0 \approx 69.7\ \mu$m^{-2}K^{-1}, to about a factor of 6. The consistency of these two TLS densities reinforce the idea that the TLSs coupling coherently at the qubit frequency and the TLSs causing low frequency noise in the tunnel junction are in fact the same TLS species.

TLS losses in superconducting resonators and SiN$_x$ dielectrics

In superconducting resonators, TLSs in the amorphous dielectrics are known to cause losses and even excess low frequency noise. One main source of TLS losses is the amorphous dielectric in the parallel-plate capacitor structure [43]. However even in resonators without the parallel-plate capacitor geometry, it has been shown that TLSs in the amorphous native oxide of the metal surfaces contribute to the loss [85].

Losses in superconducting resonators are often characterized through the resonator quality factor Q ,which is related to the loss tangent through, $\tan \delta = 1/Q$. The intrinsic loss tangent due to TLS losses is given by: $\tan \delta_0 = \pi P_0 p^2/(3\epsilon)$, where P_0 is the TLS density, p is the TLS

electric dipole moment, and ϵ is the permittivity of the dielectric. In the standard resonator Q measurement, the TLS density P_0 cannot be deconvoluted from the dipole strength p. However Khalil et. al. [35] using a voltage-biased resonator geometry, was able to deduce for a SiN$_x$ dielectric, a TLS dipole moment of $p \approx 7.9$ D and a TLS density $P_0 \approx 4.9 \times 10^{43}$ J^{-1}m^{-3}. Again, this density is comparable to our estimated density from the low frequency noise in tunnel junctions ($P_0 \approx 3.7 \times 10^{44}$ J^{-1}m^{-3}). The slightly lower P_0 estimate of Khalil et. al. [35] may be due to differences between the SiN$_x$ and AlO$_x$ dielectrics, but it may also be due to their slightly higher estimate of the TLS dipole moment.

6.7.2 Implication for qubit dephasing due to critical current noise

Our deduced TLS density, $\sigma_0 \approx 69.7$ μm^{-2}K$^{-1} \approx 3.7 \times 10^{44}$ J^{-1}m^{-3}, is consistent with the TLS density observed from the anomalous heat capacity of insulating glasses [10, 51]. This implies that our preparation of diffused amorphous AlO$_x$ is quite *ordinary*. It suggests that the preparation of fully crystalline tunnel barriers can reduce the number of these TLS defects, but what kind of improvements can we expect from a further reduction of the TLS density?

We have discussed that the typical qubit is operated well below the threshold for $1/f$ noise. That is qubit dephasing due to low frequency critical current noise is highly unlikely, although there remains a finite probability for encountering isolated activated TLSs. In current qubit architectures the typical junction areas are, $A \approx 0.03$ μm^2 [8, 80], and using our deduced density, contains not more than ~ 0.1 TLSs per GHz in qubit frequency space. That is the TLS density is likely too sparse to affect qubit operation, with the exception of perhaps in large N-qubit systems. But at the moment it seems that the problem of spurious TLS coupling common in large area junction ($A \approx 70$ μm^2) phase qubits [43] can be effectively mitigated by using much smaller junctions.

It would seem that the area where these TLS defects remain a performance bottleneck, is in limiting the quality factor of the superconducting resonators. This is simply due to the much larger surface areas spanned by the resonators, and that it is not possible to simply reduce the

area of the resonators.

CHAPTER 7

TIME DOMAIN DYNAMICS

7.1 Experimental setup
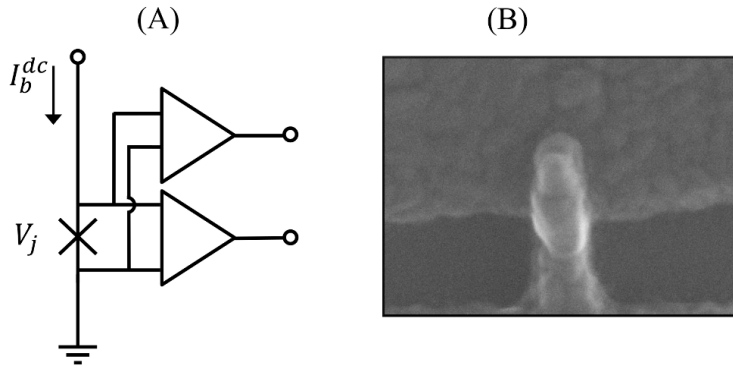
Figure 7.1: (A) Circuit schematic. Two amplifiers are used, the time series capture are then averaged to decrease amplifier noise contribution. (B) SEM image of the Al/AlO$_x$/Al junctions measured.

We fabricated conventional double angle shadow evaporated Al/AlO$_x$/Al junctions (section 4.1 with an ultra-small area. SEM image of the junction taken after the completion of measurements shows junction dimensions, $A \approx 90$ nm $\times$ 60 nm. The aluminum is electron beam evaporated in an ultra high vacuum chamber with base pressure, $P \approx 3 \times 10^{-10}$ Torr. The junction barrier is oxidized in an Ar/O$_2$ mixture, to give a tunneling resistance $R \approx 40$ kΩ. The junctions are dc current biased using a battery and a biasing resistor ($R_B \approx 400$ kΩ). Note that at our lowest biasing point, $V_B = 3$ mV, the typical dc bias current is, $I_B \approx 75$ nA.

The junction voltage is read out using two Ithaco low-noise voltage preamplifiers, then passed through an anti-aliasing low pass filter and a final gain stage where the dc offset is

removed to allow for a large gain prior to signal sampling. The amplified signal is then digitally sampled, with the choice of sampling frequency dictated by the bandwidth of the fluctuator being tracked. The presence of active fluctuators modulates the tunneling conductance, thus the junction voltage.

7.2   Power Spectral Density
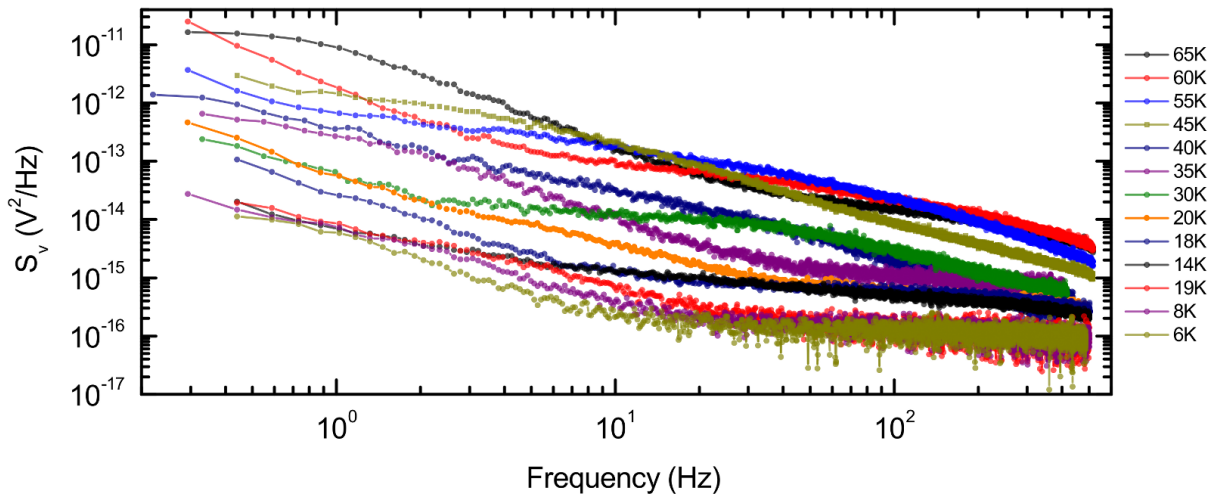
Figure 7.2:   Tunneling resistance noise power spectral density at several temperature points.

As expected for ultra small tunnel junctions, the tunneling resistance noise power spectral density is dominated by several distinct fluctuators. Figure 7.2 shows the temperature evolution of the tunneling noise PSD from $T = 65$ K to $T = 6$ K. Note that in figure 7.2 the temperature is varied by approximately a factor of 10 and the noise power spectral density at $f = 1$ Hz falls off by more than a factor of 1000, which is much faster than the $S_{R_n}/R_n^2 \propto 1/T$ dependence expected in the featureless $1/f$-noise regime.

After cooling down to base we found that the junction tunneling resistance is characterized by one fluctuator in our measurement bandwidth, $f < 10$ kHz, and trackable in the temperature range: $T \approx 6 - 13.5$ K. Figure 7.3 shows time traces dominated by the fluctuator at $T = 9$ K and for several bias voltages, $V_b = 12, 21,$ and 24 mV.
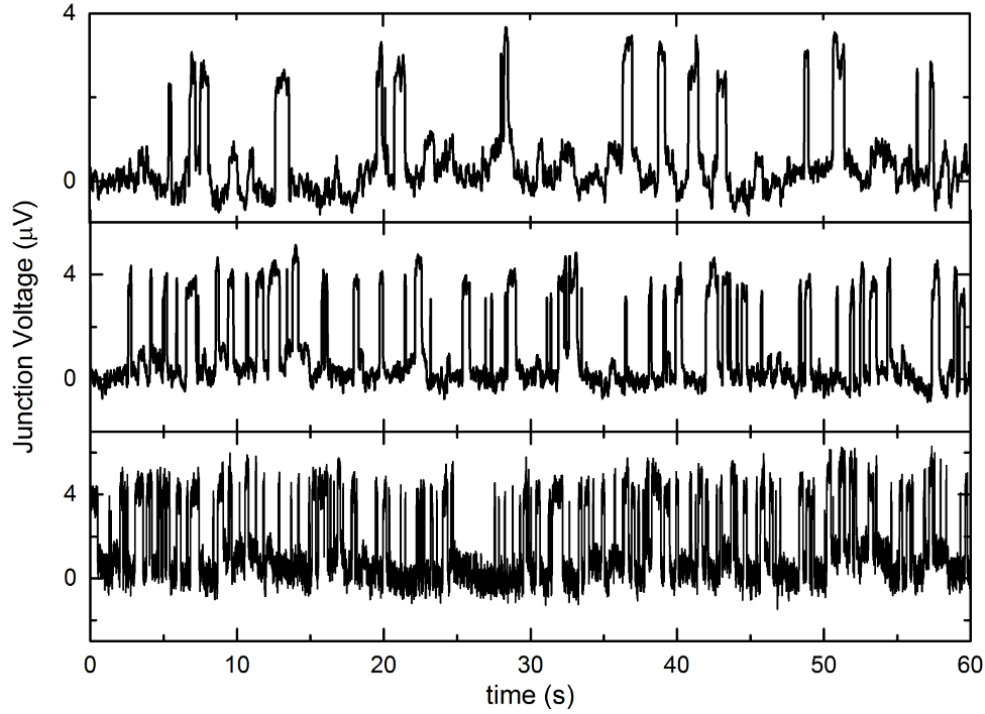
Figure 7.3: Time series capture of junction JJ45 at three different bias points, $V_b = 12, 21$, and 24 mV, all at $T = 9$ K.

7.3 Time domain analysis

A random telegraph noise is the switching between two discrete levels y_1 and y_2, $\delta y = |y_2 - y_1|$. The time intervals spent in the two states $\{y_1, y_2\}$ are characterized by their respective characteristic lifetimes τ_1 and τ_2. In the frequency domain a fluctuator generates a Lorentzian power spectral density, $S(\omega) \propto \tau_{eff}/(\omega^2 \tau_{eff}^2 + 1)$, where τ_{eff} is the effective characteristic time is combination of the characteristic times τ_1 and τ_2 given by:

$$\frac{1}{\tau_{eff}} = \frac{1}{\tau_1} + \frac{1}{\tau_2} \tag{7.1}$$

Because both timescales τ_1 and τ_2 are reduced to an effective timescale τ_{eff}, TLS analysis in the frequency domain alone cannot paint a complete picture of the TLS dynamics. In the time domain if there is only one active fluctuator or if other active TLSs have characteristic times
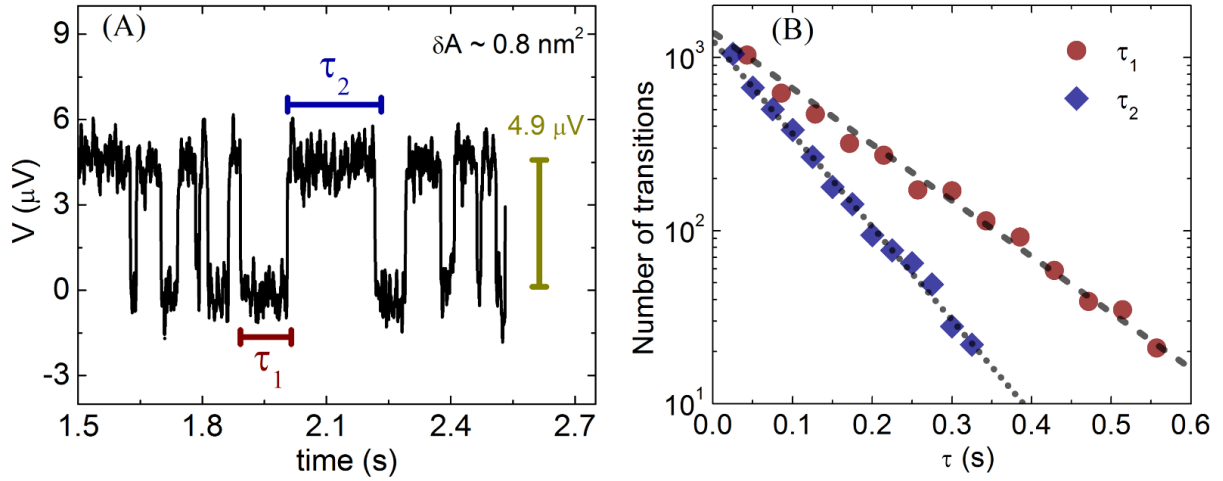
Figure 7.4: (A) Example time trace of the random telegraph noise. From the time capture, a histogram of the lifetimes τ_1 in the up-state and τ_2 in the down-state can be reconstructed. (B) Histogram of all the time the TLS spends in the up and down states. The dashed lines are fit to an exponential decay, $y = Ce^{-\tau/\tau_i}$, reflecting the probability distribution of the lifetimes.

τ_i that are sufficiently spaced apart, then it's possible to track the bistable voltage signal and reconstruct the lifetimes τ_1 and τ_2 of the fluctuator. Figure 7.4A shows a time trace snippet of the fluctuator at $T = 9$ K and $V_b = 30$ mV. We perform time domain analysis of the TLS by identifying all the switching events contained in a time trace, and extracting the lifetimes spent in the high-resistance state, τ_1 and the low-resistance state, τ_2. We can then bin the extracted lifetimes to create a histogram as shown in figure 7.4B, where the dashed lines are fits to $y \propto e^{-\tau/\tau_i}$ from which the characteristic timescale τ_i can be extracted.

Figure 7.5 shows the extracted TLS lifetime histograms at $T = 9$ K at several different biasing points, $V_b = 15, 18, 21,$ and 24 mV. The change in the slope of the exponential distribution is immediately apparent, indicating a strong voltage dependence in the TLS lifetimes.

7.3.1   Theoretical background: Two-state Markovian processes

The two level fluctuation can be modelled as a two-state Markovian process. The switching process has no memory, so that the probability of a transition in a time interval t and $t + \Delta t$
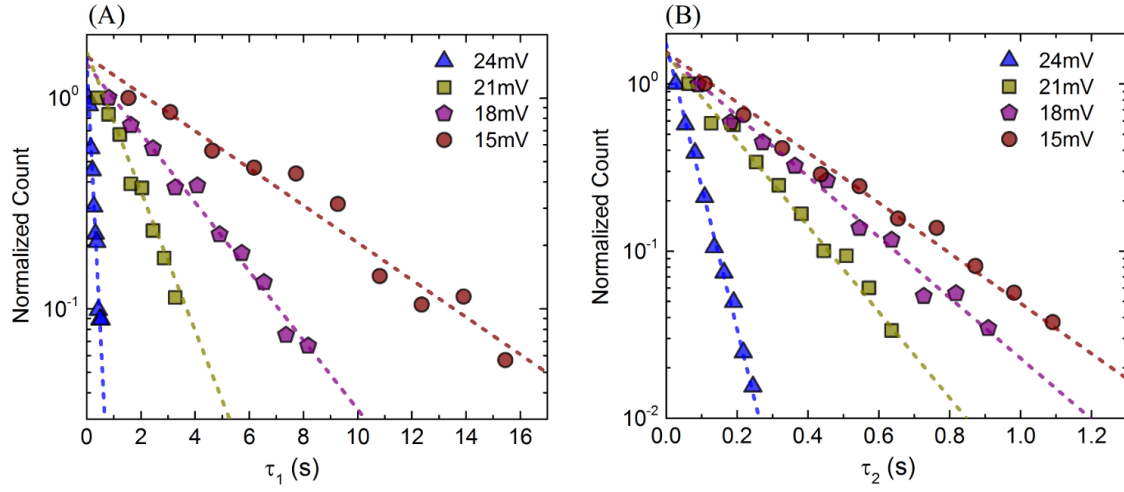
Figure 7.5: Histogram of the TLS lifetimes at $T = 9$ K for several different voltage bias points, $V_b = 15, 18, 21, 24$ mV. (A) High resistance state, τ_1. (B) Low resistance state, τ_2. The dashed lines are fits to the exponential probability distribution $\propto e^{-\tau/\tau_i}$

depends only on the interval length Δt and not on t.

Labeling the transition probability from state-1 to state-2 as $P_1(t)$, then $1 - P_1(t)$ is the probability that the transition $1 \rightarrow 2$ did not occur at time t. Labeling P_1^Δ as the probability of making the transition $1 \rightarrow 2$ in the time interval t and $t + \Delta t$, then:

$$\frac{dP_1(t)}{dt} \Delta t = (1 - P_1(t)) P_1^\Delta(t) \tag{7.2}$$

And the probability for a transition within a time interval Δt at time t:

$$P_1^\Delta(t, \Delta t) = C\Delta t \tag{7.3}$$

By combining the above two equations, we get the transition probability:

$$P_1(t) = 1 - e^{-t/\tau_1}, \tag{7.4}$$

where τ_1 is the characteristic lifetime in state-1. The probability of transition between a time

interval Δt is then:

$$\frac{dP_1}{dt}\Delta t = \frac{1}{\tau_1}e^{-t/\tau_1}\Delta t \tag{7.5}$$

Thus the lifetime τ_1 probability density is exponentially distributed:

$$\mathcal{P}_1(\tau) = \frac{1}{\tau_1}e^{-\tau/\tau_1}, \tag{7.6}$$

and similarly for the characteristic lifetime τ_2 in state-2: $\mathcal{P}_2(t) = 1/\tau_2 \exp(-t/\tau_2)$.

Given a random telegraph signal $v(t)$, we can then create a histogram of the lifetimes in state-1 and state-2 and calculate the characteristic times as given by equation 7.6. Figure 7.4B shows an example histogram that shows excellent agreement with the expected exponential distribution for a TLS.

7.4   TLS A: A quantum tunneling TLS

7.4.1   Temperature Dependence

Figure 7.6A shows the temperature dependence of the transition rates of TLS A at $V_b = 3$ mV. $\tau_1 = 1/\Gamma_1$ is the characteristic lifetime of the junction in the *low resistance* state, and $\tau_2 = 1/\Gamma_2$ is the characteristic lifetime of the junction in the *high resistance* state. In this particular case the TLS energy bias Δ never changes sign, and it happens that $\tau_1 > \tau_2$ for all voltage biases probed in the experiment. That is state-1 of the TLS characterized by τ_1 remains the lower energy (ground) state of the TLS at all bias points. Note that in general it is possible that the interaction with an external field (ie. electric or elastic) may potentially alter the TLS bias Δ, thus the sense of which state is the *ground* state.

Figure 7.6B depicts a schematic of the TLS potential energy. U_1 and U_2 are the potential barrier height out of the left, $|L\rangle$, and right, $|R\rangle$, wells respectively. The localized states $|L\rangle$ and $|R\rangle$ have an energy difference Δ and a tunnel coupling strength Δ_0. The TLS is said to be degenerate if $\Delta = 0$. TLS transitions can occur through thermal activation over the
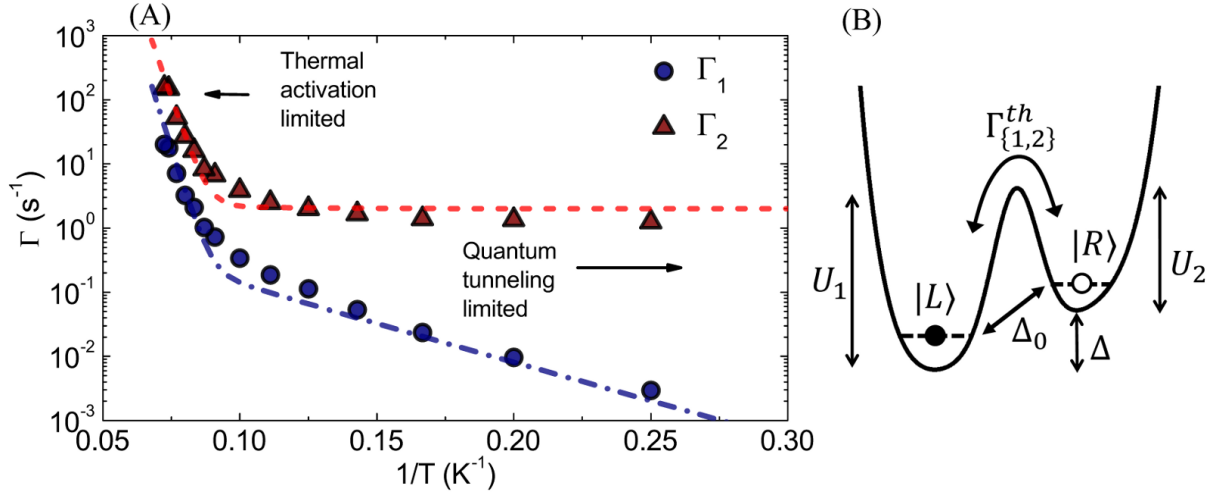
Figure 7.6: (A) Temperature dependence of the transition rates $\Gamma_i = 1/\tau_i$ for TLS A. $V_b = 3$ mV. The dashed lines are fits to the sum of thermal activation and quantum-limited tunneling rates. At high temperatures the thermal activation rate dominates, while at lower temperatures the rate is limited by quantum-tunneling. (B) Schematic two-level system potential energy.

potential barrier with a transition rate Γ^{th}, or via a quantum mechanical tunneling process with transition rate, Γ^{tun}.

In figure 7.6A we find that the TLS transition rates are well described by the sum of a Boltzmann thermally activated rate Γ_i^{th} and a one-phonon tunneling rate Γ_i^{ph}. So that the total transition rate is given by:

$$\Gamma_i = \Gamma_i^{th} + \Gamma_i^{ph}, \tag{7.7}$$

where $i \in \{1, 2\}$ to denote the rates out of the left and right wells.

At high temperatures the transitions occur due to thermal energy fluctuations driving the fluctuator above the potential barriers U_1 and U_2. At lower temperatures the thermal activation rates decay exponentially, and the TLS transitions are then limited by quantum mechanical tunneling through the barrier, along with the absorption/emission of a phonon.

The thermally activated rate is given by the usual Maxwell-Boltzmann factor:

$$\Gamma_i^{th} = \Gamma_0 \exp\left(-U_i/kT\right), \tag{7.8}$$

We find that for TLS A, $\Delta \gg \Delta_0$, so that the energy eigenstates can be approximately given by the localized basis states $|L\rangle$ and $|R\rangle$. The TLS energy is thus $E = \sqrt{\Delta^2 + \Delta_0^2} \approx \Delta$. The TLS can make a transition by absorbing/emitting a phonon of energy $\approx \Delta$ which can be thought of as momentarily making the TLS degenerate, allowing a quantum tunneling event with rate $\Delta_0/\hbar$. Thus the one-phonon transition rates are given by:

$$\Gamma_1^{tun} = \omega_0 e^{-\lambda} n_{BE}(E) = \frac{\omega_0 e^{-\lambda}}{\exp(E/kT) - 1} \tag{7.9}$$

$$\Gamma_2^{tun} = \omega_0 e^{-\lambda} \left(1 + n_{BE}(E)\right) = \frac{\omega_0 e^{-\lambda}}{1 - \exp(-E/kT)}, \tag{7.10}$$

where ω_0 is the attempt frequency on the order of the Debye frequency, $\lambda = 2d\sqrt{2mU/\hbar^2}$ is the WKB exponent to approximate the quantum tunneling probability out of localized wells, and n_{BE} is the Bose-Einstein distribution function to describe the phonon occupation probability.

In figure 7.6 the solid circles and triangles are the data points, while the dash and dot-dash lines are the two-component rate fits. In the high-T limit the thermally activated rate dominates and well fitted to an attempt frequency $\omega_0 \approx 2.5 \times 10^{11}$ s^{-1}, which is close to the typical Debye frequency. The potential barriers fits are $U_1 \approx 26.9$ meV and $U_2 \approx 24.8$ meV, corresponding to an asymmetry energy $\Delta E = U_1 - U_2 \approx 2.1$ meV.

At $T \approx 10$ K we observed a transition from thermal activation to a tunneling TLS behavior. Note that in the limit $T \to 0$, $\Delta E/k_B T \gg 1$, and the Bose-Einstein factor in the relaxation rate Γ_2 drops out, leaving only the quantum tunneling rate [64, 56]:

$$\Gamma_2^{ph} \approx \omega_0 \exp\left(-2d\sqrt{\frac{2mU}{\hbar^2}}\right) \approx 1 \text{ s}^{-1} \tag{7.11}$$

We can use the WKB approximation and the fitted parameters to deduce the value of the mass-distance product $m^{1/2}d$. Note that since the tunneling probability depends on both the tunneling species mass m and the tunneling distance d, it is not possible through this method to deduce the value of each quantity separately. The best we can do is to deduce the product,

$m^{1/2}d$. We find that the TLS is best fitted to:

$$m^{1/2}d \approx 1.5 \times 10^{-23} \; \sqrt{\text{kg}}.m, \tag{7.12}$$

which is consistent with the tunneling species being an atomic mass, $m \sim 10^{-27} - 10^{26}$ kg, and tunneling distances, $d \sim 1$ Å, the order of crystal lattice distances. For example if the tunneling species is an oxygen mass ($m \approx 2.7 \times 10^{-26}$ kg), then tunneling distance is, $d \approx 0.9$ Å. If we instead assume the tunneling species to have an electronic mass, the tunneling distance must be in the order of 160 Å, while not physically impossible the value is too large for the physical system as it is incompatible with the measured dipole moment of the TLS (to be discussed).
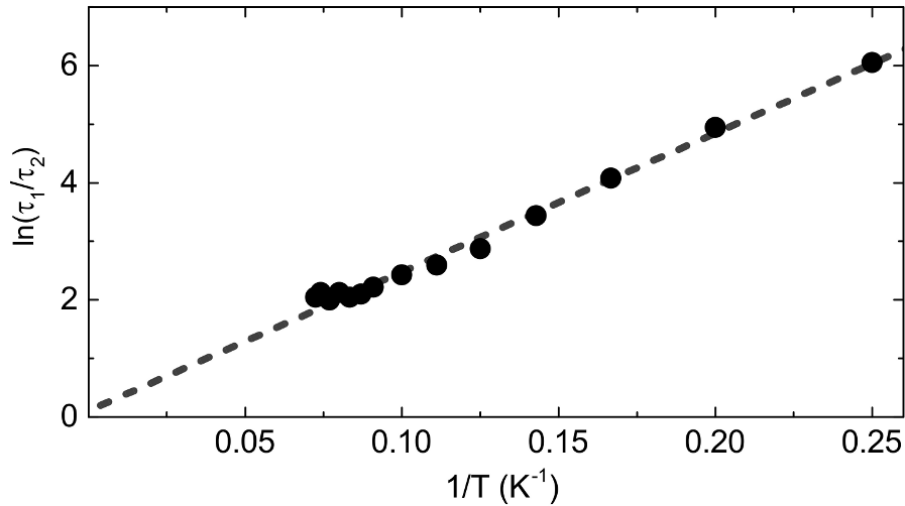
Figure 7.7: The switching ratio, $R = \tau_1/\tau_2$, as a function of $1/T$. Measured at $V_b = 3$ mV.

The ratio of the switching times, $R = \tau_1/\tau_2$, gives a very useful thermodynamic handle on the TLS switching dynamics. In the Boltzmann thermally activated regime,the ratio is given by:

$$R = \frac{\tau_1}{\tau_2} = \frac{\tau_0 \exp{(U_1/k_B T)}}{\tau_0 \exp{(U_1/k_B T)}} = \exp{(\Delta E/k_B T)} \tag{7.13}$$

That is a TLS whose switching dynamics follow equation 7.13 above is in thermodynamic equilibrium with the bath. Deviations from this exponential dependence typically indicate non-equilibrium conditions such as self-heating. Similarly the switching ratio in the quantum-

limited case follows the exact same exponential dependence:

$$R = \frac{\tau_1}{\tau_2} = \frac{\exp\left(\Delta/k_B T\right) - 1}{1 - \exp\left(-\Delta/k_B T\right)} = \exp\left(\Delta/k_B T\right) \tag{7.14}$$

In general the TLS left, $|1\rangle$, and right, $|2\rangle$, wells can have more than one microstates or degeneracies N_1 and N_2 respectively. In this case the expression of the switching rate ratio needs to be adjusted to take into account of the added entropy [73, 72]:

$$R = \frac{\tau_1}{\tau_2} = \frac{N_1}{N_2} \exp\left(\Delta/k_B T\right) \tag{7.15}$$

Figure 7.7 shows the switching ratio, $R = \tau_1/\tau_2$, plotted as a function of the inverse temperature $1/T$. Note that data points in both the thermally activated and quantum tunneling limited regimes have been included in the plot. The gray dashed line is a fit to $\ln(\tau_1/\tau_2) = C + (\Delta E/k_B)\frac{1}{T}$. We find that the switching ratios in both switching regimes follow the expected exponential dependence, implying that the TLS is in thermodynamic equilibrium over the temperature range probed above (down to $T = 4$ K at $V_b = 3$ mV). The extracted $\Delta E\left(V_b = 3 \text{ mV}\right) \approx 2$ meV is consistent with the value obtained from fitting the thermally activated switching rates above. The intercept $C = \ln(N_1/N_2) \approx 0$ implies that the TLS left and right wells have similar degeneracies, $N_1 \approx N_2$. Note that this is in stark contrast to that found in earlier experiments in PbInAu/In$_2$O$_3$/Pb edge junctions [73, 72], where a large entropy difference was found which in that case is consistent with the picture of an electron tunneling from the continuum (large entropy) into an electronic trap state (small entropy). In contrast the small entropy difference in the present experiment supports the picture of a particle tunneling from one potential well to another almost identical well, such as in the case of atomic defects in an amorphous dielectric.
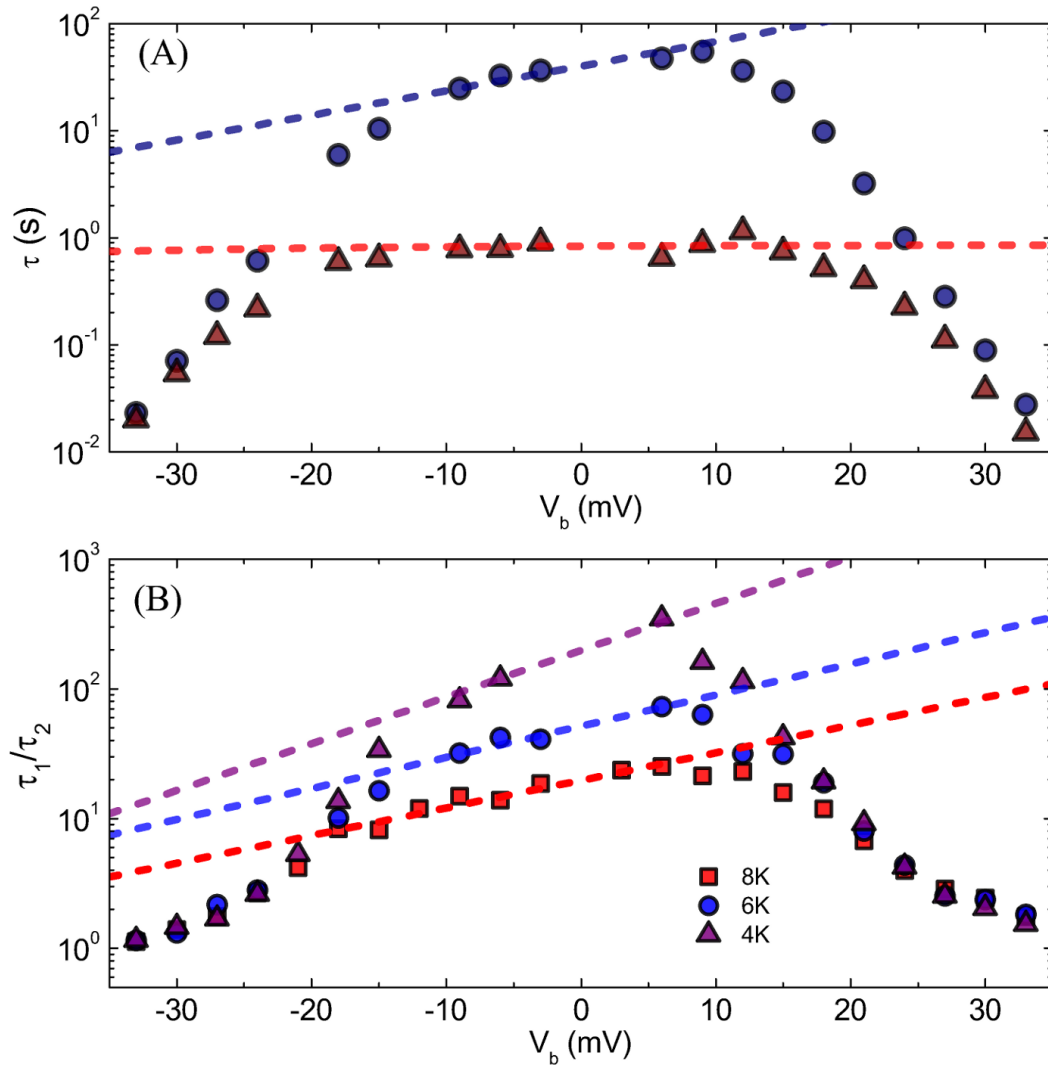
Figure 7.8: (A) Voltage dependence of the lifetimes τ_1 and τ_2 at $T = 6$ K. Blue dashed line is a one-phonon rate fit to the ground state lifetime. Red dashed line is a one-phonon rate fit to the excited state lifetime. At large voltage bias the TLS is driven out of equilibrium, which shows up as a sharp decay in the TLS lifetimes. (B) Voltage dependence of the switching ratio $R = \tau_1/\tau_2$ shown for several temperatures, $T = 4, 6,$ and 8 K, (purple triangles, blue circles, and red squares, respectively).

7.4.2   Static electric field response

The junction can be approximated as a parallel plate capacitor, such that the electric field in the dielectric is simply, $|\mathbf{E}| = V/t$, where $t \approx 1$ nm is the thickness of the tunneling dielectric. The interaction of the TLS dipole moment with this electric field leads to a correction in the TLS energy:

$$\Delta = \Delta(0) + \mathbf{E} \cdot \mathbf{P} = \Delta(0) + |\mathbf{E}||\mathbf{P}| \cos\theta, \tag{7.16}$$

where $\Delta(0)$ is the asymmetry energy at $V_b = 0$, $\mathbf{E}$ is the electric field across the junction dielectric, and $\mathbf{P}$ is the TLS dipole which makes an angle θ relative to the electric field.

Figure 7.8A plots the lifetimes τ_1 and τ_2 at $T = 6$ K as a function of the applied electric field (voltage bias). The voltage dependence shows two different behaviors, corresponding to the low and high bias voltage regimes. At high voltage biases, $V_b \gtrsim 20$ meV, we observed the onset of a non-equilibrium process, which will be described later in section 7.4.3. In this section we will describe the TLS dynamics at low voltage biases where the TLS remains in equilibrium.

The TLS lifetime in the excited state, τ_2 is relatively insensitive to the external field. This is consistent with the TLS transition being driven by phonon emission and tunneling to the ground state, given by equation 7.10. In the limit $\Delta/kT \gg 1$:

$$\tau_2 \approx \frac{\hbar}{\Delta_0} \left(1 - \exp\left(-\frac{\Delta}{kT}\right) \right) \approx \tau_q, \tag{7.17}$$

where $\tau_q = \hbar/\Delta_0$. The red dashed line in figure 7.8 represents a fit to this one-phonon rate.

In comparison the TLS lifetime in the ground state, τ_1, shows an exponential dependence on the applied bias, which is expected from the one-phonon rate (equation 7.9):

$$\ln(\tau_1/\tau_q) \approx \frac{\Delta(0)}{kT} + \gamma \frac{V_b}{kT}, \tag{7.18}$$

where $\tau_q = \hbar/\Delta_0$, $\Delta(0)$ is the TLS asymmetry energy at zero external field, kT is the thermal energy, and the slope γ is related to the electric dipole moment of the TLS. A fit to equation

7.18 above is shown as the blue dashed line in figure 7.8A.

The physical parameters $\Delta(0)$ and the TLS dipole moment $|\mathbf{P}|$ can be more readily extracted from fitting the ratio of the switching times τ_1/τ_2. By looking at τ_1/τ_2 we eliminate the dependence on the parameter τ_q. Figure 7.8B plots the switching rate ratio, $R = \tau_1/\tau_2 = \exp\left(\Delta(V_b)/kT\right)$, as a function of the applied electric field (voltage bias). At low voltage biases the TLS remains in equilibrium with the bath temperature and the dependence is given by:

$$\tau_1/\tau_2 = \exp\left(\frac{\Delta(V_b)}{kT}\right) = \exp\left(\frac{\Delta(0) + \gamma V_b}{kT}\right) \tag{7.19}$$

$$\ln(\tau_1/\tau_2) = \frac{\Delta(0)}{kT} + \left(\frac{\gamma}{kT}\right)V_b \tag{7.20}$$

where the slope γ gives the TLS dipole moment projected along the electric field's axis:

$$\gamma = |\mathbf{P}| \cos\theta / t \tag{7.21}$$

The dashed lines in figure 7.8B are linear fits to $\ln(\tau_1/\tau_2)$ according to equation 7.20 above. One feature to note is that the slope γ is monotonic across positive and negative voltage biases, this behavior is consistent with the simplest interpretation of the dipole-electric field interaction continuously tipping the TLS asymmetry energy Δ. The fitting parameters $\Delta(0)$ and γ are consistent across the temperature range probed, $T = 4 - 9$ K, giving the averaged values $\Delta(0) = 1.95$ meV and the slope $\gamma \approx 26$ μeV/mV_b, giving the aligned dipole moment strength:

$$P \cos\theta \approx 0.26 \ e\text{\AA} \tag{7.22}$$

Note that it is not possible in the present experiment to reconstruct the dipole angle θ. But to gain a better estimation for the value of the bare dipole moment, P, we could average out the θ dependence:

$$\langle P \rangle_\theta = \frac{1}{\pi} \int_{-\pi/2}^{\pi/2} P \cos\theta \ d\theta = P\left(\frac{2}{\pi}\right), \tag{7.23}$$

so that the bare dipole moment can be estimated as:

$$P \approx 0.26 \ e\text{Å}/(2/\pi) \approx 0.41 \ e\text{Å}, \tag{7.24}$$

the value of which reinforces the picture of a fluctuator with charge e tunneling through crystal lattice distances (~ 1 Å).

7.4.3   Non-equilibrium effects

Empirical description
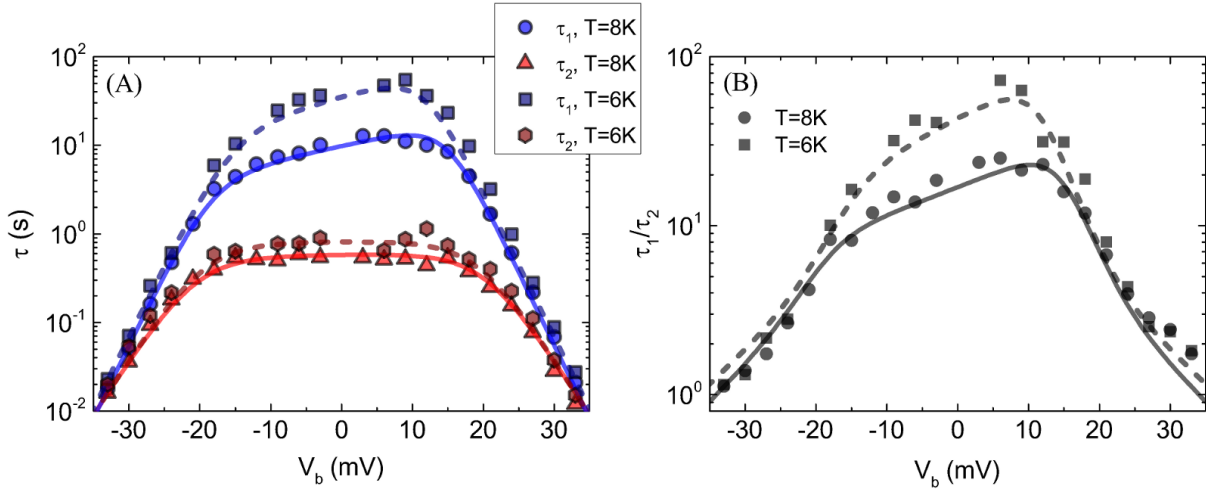
Figure 7.9:   (A) Voltage dependence of the TLS lifetimes fitted to a one-phonon rate and a second empirical exponential lifetime, $\propto \exp(-\gamma V_b)$. (B) TLS lifetimes ratio τ_1/τ_2 and the fitting lines, $T = 6, \ 8$ K.

We can empirically describe the behavior of the TLS lifetimes as the sum of two rates, the one-phonon scattering rate Γ_i^{ph} and a second rate Γ_i^* that has an approximately exponential dependence with respect to the voltage bias. At low voltage biases, the transition rate is dominated by the one-phonon rate, and the second rate dominates the high voltage bias regime due to its exponential dependence:

$$\Gamma_i = \Gamma_i^{ph} + \Gamma_i^*, \tag{7.25}$$

where Γ_i^* is approximately:

$$\Gamma_i^* \approx A_i \exp\left(B_i|V_b|\right) \tag{7.26}$$

Figure 7.9A plots the TLS lifetimes at $T = 6$, and 8 K, the dashed and solid lines are the fits to the two rate model. It is still not entirely clear what is the physical mechanism for this second exponential rate.

Self-heating model
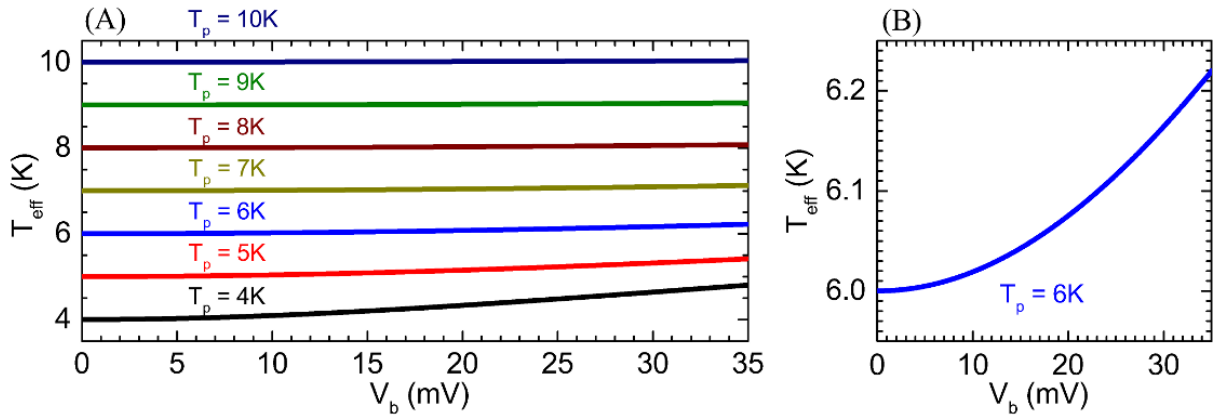
Figure 7.10:   Calculated effective electron temperature, following Kautz et. al. [32]. (A) Effective temperature due to self-heating for several different bath temperatures, $T_{bath} = 4 - 10$ K. (B) A more detailed plot on the self-heating correction to the electronic temperature for $T = 6$ K. The self-heating correction is less than $\Delta T \approx 220$ mK at $V_b \approx 35$ mV.

One obvious candidate for an exponential dependence is electronic self heating. The temperature of the TLS enters into the transition rates through the thermodynamic factors of $\exp\left(E/kT\right)$. However it should be stated at the outset that we have found self heating to be insufficient to account for how far the TLS is driven out of equilibrium.

We can estimate the extent of the electronic self-heating following the results of Kautz et. al. [32] from investigating the self-heating effect in Al single electron transistors (SETs). We also need to make the approximation that the TLS temperature T is approximately equal to the electronic temperature in the metallic leads [33, 34]. In SETs the metal island is isolated

from the thermallized left and right leads by the presence of the tunnel barriers. Consequently thermal conduction through the leads is small and it is known that the island temperature is determined by the electron-phonon heat transfer efficiency to the lattice [32]. The effective temperature is given by [32, 59, 76]:

$$T_e^5 = T_p^5 + \frac{P}{\Sigma V}, \tag{7.27}$$

where T_e is the effective electron temperature, T_p is the lattice temperature, P is the power dissipated, $\Sigma \approx 0.2$ nW K$^{-5}\mu$m^{-3} is the electron-phonon coupling parameter for Al, and V is the SET island volume. Note that it was found that the electron temperature in the island depends on the volume of the island and not the junction size [32]. This is likely due to the fact that the dimensions of the junctions typically used in SETs are shorter than the electron inelastic scattering length, $l_{in} \sim 0.5 - 1$ μm [25]. Therefore the SET island size represents the limiting volume for the electron-phonon interaction in equation 7.27.

In our single junction geometry the thermalization volume is not as restrictive as the SET island. Unlike in SETs, in the case of a single junction the thermal conduction through the left and right leads are not restricted by the tunnel barrier, consequently the thermalization volume should extend much further through the left and right metal electrodes. Thus the SET island volume ($V \approx 0.1$ μm^3) used in Kautz et. al. [32] should represent an upper bound for the self-heating effect in a single junction. Note that the junction sizes used in Al SETs are typically even smaller than our junction presently. A worst case scenario for self-heating is to assume that the power is dissipated within a volume covering the junction area, 60×90 nm^2 with a metal thickness $t \approx 120$ nm.

Figure 7.10 plots the self-heating correction (equation 7.27) assuming $V = 0.1$ μm^3 is a reasonable parameter to use for our single junction. As expected, the self-heating correction is small and only noticeable for $T = 4 - 5$ K.

In section 7.4.1 we have deduced the parameters for the two component TLS transition rates corresponding to the sum of the one-phonon relaxation and thermally activated rates. In figure
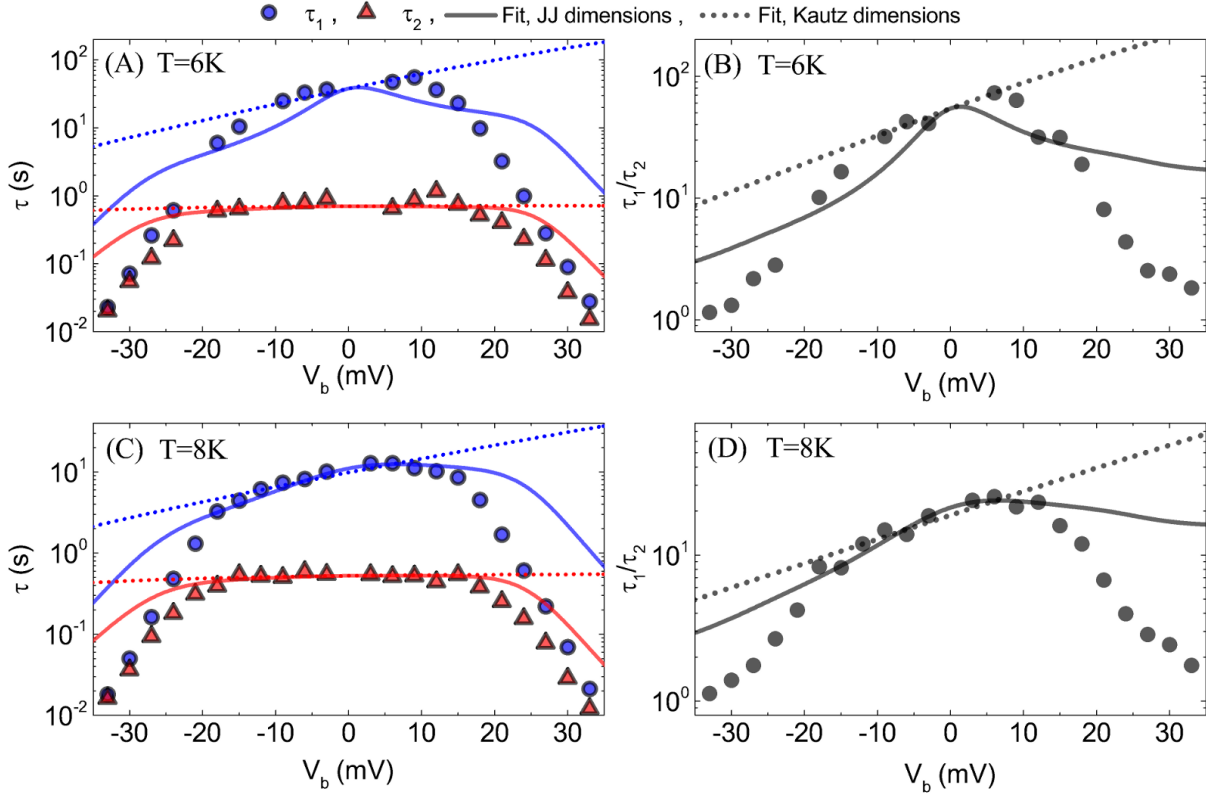
Figure 7.11: Self-heating model of the TLS lifetimes. The TLS transition rate is the sum of the one-phonon and thermally activated rates. The effective temperature at each bias points is calculated using the electron-phonon model, with $\Sigma = 0.2$ nW K$^{-5}\mu$m^{-3} and (dotted line) the SET volume used in Kautz [32], (solid lines) the physical junction dimension. (A-B) The TLS lifetimes and ratio at $T = 6$ K (C-D) The TLS lifetimes at $T = 8$ K.

7.11 we computed that model with the addition of a self-heating correction under an applied voltage bias. Figure 7.11(A-B) shows the fitted rates and the lifetime ratio at $T = 6$ K, figure 7.11(C-D) shows the fitted rates and lifetime ratio at $T = 8K$. The dotted lines represent the fit calculated assuming the self-heating correction used in Kautz et. al. [32]. The solid lines are the fit assuming the worst case scenario that the electron-phonon thermalization occurs within the volume of metal forming the junction area ($\approx 60 \times 90 \times 120$ nm^3). In either case the degree of self heating is not sufficient to account for the degree to which the TLS is being driven out of equilibrium, this is most evident in the poor fitting of the lifetime ratios τ_1/τ_2.

It is not surprising that the self-heating model cannot account for the non-equilibrium process

observed. To see this, consider that the TLS lifetime ratio $\tau_1/\tau_2 = \exp\left(\Delta/kT\right)$ depends only on the difference in the energy of the two states and on the temperature T, thus it summarizes the thermodynamic information on the TLS. This is in contrast to the individual transition rates which depend on both the thermodynamic and dynamical variables such as the tunneling probability and attempt frequency.

We can thus obtain the effective temperature T^* of the TLS by inverting the switching ratio $\tau_1/\tau_2 = \exp\left(\Delta/kT^*\right)$:

$$T^* = \frac{\Delta(V_b)}{k\ln\left(\tau_1/\tau_2\right)} = \frac{\Delta(0) + \gamma V_b}{k\ln\left(\tau_1/\tau_2\right)} \tag{7.28}$$
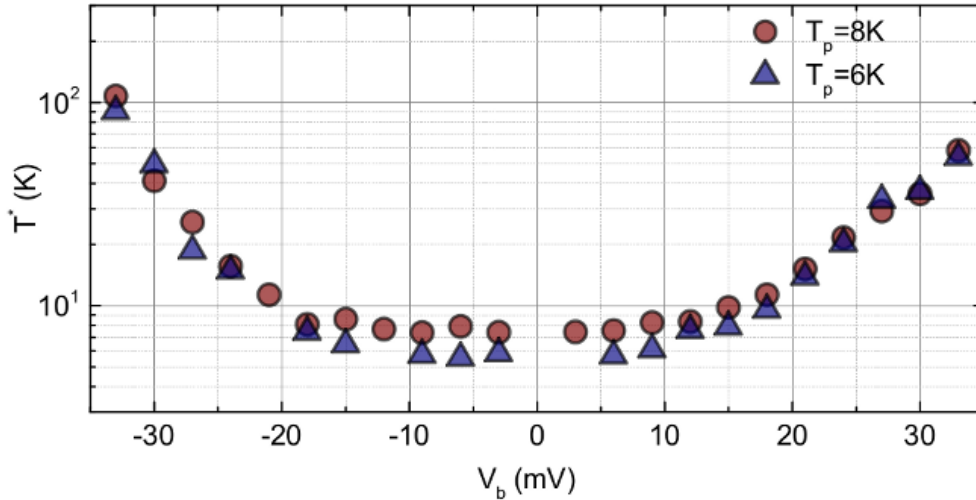
Figure 7.12: Effective temperature, T^* at bath temperature $T = 8$ K of the TLS deduced from the switching ratio $\tau_1/\tau_2 = \exp\left(\Delta E/k_B T^*\right)$.

If the TLS is in thermal equilibrium with the lattice then the effective temperature T^* will be equal to the lattice temperature T_p. However if the TLS is driven out of equilibrium, then the TLS may see an increased effective temperature, defined by equation 7.28. Figure 7.12 plots the effective temperature T^* of the TLS as a function of the voltage bias. The red circles are the TLS effective temperature for a bath temperature of $T_p = 8$ K, and the blue triangles represent $T_p = 6$ K. At low voltage biases the TLS is in equilibrium with the bath, $T^* = T_p$. The TLS is then driven out of equilibrium in the vicinity $V_b \lesssim 20$ mV and $V_b \gtrsim 12$ mV.

More importantly the effective temperature T^* increases exponentially, that $T^* \sim 60$ K at $V_b \approx 33$ mV and even reaching $T^* \sim 100$ K at $V_b \approx -33$ mV. It is somewhat un-physical to imagine a self-heating process that can account for that amount of 'heating'. In fact we observed a transition to thermally activated rates in the region $T \approx 10$ K, that if the TLS is being heated, then by $T \approx 22$ K the characteristic TLS lifetime, $1/\tau = 1/\tau_1 + 1/\tau_2$, would have been $\tau \approx 1$ μs, well outside the bandwidth of our measurement. Instead at a TLS effective temperature, $T^* \approx 22$ K, we in fact observed the TLS to have a characteristic lifetime $\tau \approx 0.1$ s. That is roughly *five* orders of magnitude off from the assumption that the TLS is thermally driven, and a strong indication that the TLS is being driven by a process other than electronic Joule heating.

Inelastic electron scattering

An alternative explanation is that the TLS is being driven out of equilibrium due to its interaction with the tunneling electrons. In fact it is known that the TLS-electron interaction in metallic glasses lead to TLS relaxation times that are orders of magnitude shorter compared to TLSs in insulating glasses [24, 69].

The tunneling electrons can scatter off the TLS, losing or gaining an energy Δ in the process and driving the TLS transition. The transition rates can be calculated in a method similar to the calculation of one-electron scattering rates for metallic glasses [51, 69], with the addition that in tunnel junctions, an energy difference eV_b is maintained across the two electrodes. The TLS transition rate from the ground to excited state can then be calculated via Fermi's golden rule [69, 33]:

$$\Gamma_{ge} = \frac{2\pi}{\hbar} \left| \langle e|H'|g \rangle \right|^2 f_\epsilon (1 - f_{\epsilon'}) \delta(\epsilon' - (\epsilon - \Delta + eV_B)), \tag{7.29}$$

Where the δ-function is defined to enforce the conservation of energy condition, and f_ϵ is the Fermi-Dirac distribution:

$$f_\epsilon = f(\epsilon) = \frac{1}{1 + \exp(\epsilon/kT)} \tag{7.30}$$

The ground-to-excited state transition rate is then given by:

$$\Gamma_{ge} \propto \int \int \, d\epsilon \, d\epsilon' \, \frac{1}{1 + \exp\left(\epsilon/kT\right)} \left(1 - \frac{1}{1 + \exp\left(\epsilon'/kT\right)}\right) \delta\left(\epsilon' - (\epsilon - \Delta + V_b)\right) \qquad (7.31)$$

$$\Gamma_{ge} = \frac{M}{e^2 R} \frac{eV_b - \Delta}{1 - \exp\left(-(eV_b - \Delta)/kT\right)} \qquad (7.32)$$

Similarly the transition from the excited to ground state occurs through an electron scattering process where the electron gains an energy Δ. The corresponding rate is then:

$$\Gamma_{eg}^{in} = \frac{M}{e^2 R} \frac{eV_b + \Delta}{1 - \exp\left(-(eV_b + \Delta)/kT\right)}, \qquad (7.33)$$

where M is a proportionality constant related to the scattering cross-section for the electron-TLS interaction, and R is the tunneling resistance. The ratio of the inelastic scattering rates is given by:

$$\frac{\tau_1}{\tau_2} = \frac{eV_b + \Delta}{eV_b - \Delta} \frac{1 - \exp\left(-\frac{eV_b - \Delta}{kT}\right)}{1 - \exp\left(-\frac{eV_b + \Delta}{kT}\right)} \qquad (7.34)$$

Note that for small voltage biases, $V_b \ll \Delta$, we recover the switching ratio for a TLS in thermal equilibrium: $\tau_1/\tau_2 \approx \exp\left(\Delta/kT\right)$. However in the limit $V_b - \Delta \gg kT$, we see that the TLS switching ratio falls, $\tau_1/\tau_2 \to 1$. This is precisely the behavior observed in the data. The application of a voltage bias drives the TLS to very high effective temperatures T^* as evidenced in the switching ratio, $\tau_1/\tau_2 \to 1$, without requiring the TLS to be thermally driven.

While the one-electron scattering process qualitatively describes how the TLS can be driven out of equilibrium without actual heating, it fails to recover the V_b exponential dependence observed in the data. The one-electron scattering rate is *linear* in the voltage bias V_b, a far too weak dependence to be able to describe the data. One possible way to recover an exponential-V_b dependence through inelastic electron scattering, is the inclusion of higher order scattering processes. Since :

$$e^x = \sum_n \frac{x^n}{n!}, \qquad (7.35)$$

it is possible to approximate an exponential dependence by including the higher order x^n terms, which correspond to the n-electron scattering process.

As a toy model, we consider a process where two electrons scatter off the TLS where each electron loses/gains an energy $\Delta/2$. An n-electron process then involves each electron losing/gaining an energy Δ/n. Also we are interested in the large bias regime, where $V_b - \Delta \gg kT$, such that the Fermi-Dirac distribution is approximately:

$$f(\epsilon) = \begin{cases} 1 & \epsilon > 0 \\ 0 & \epsilon < 0 \end{cases}$$
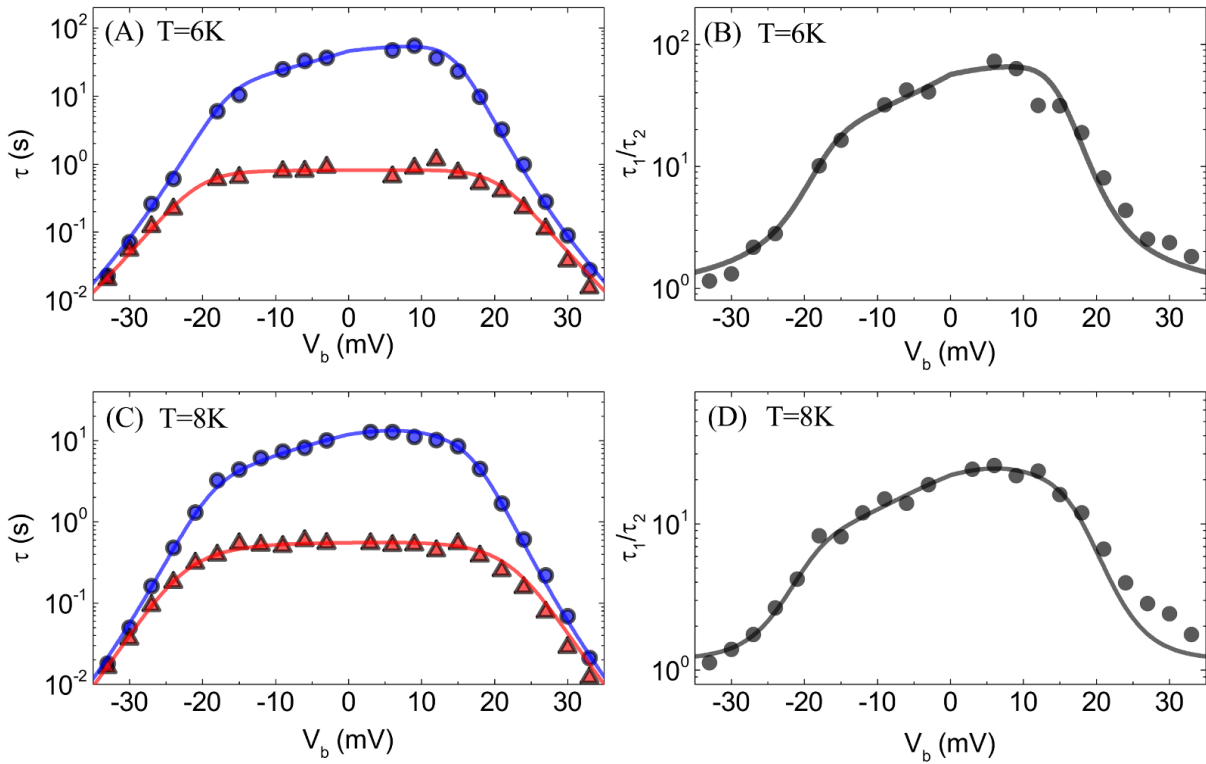
Figure 7.13: Effective temperature, T^* at bath temperature $T = 8$ K of the TLS deduced from the switching ratio $\tau_1/\tau_2 = \exp\left(\Delta E/k_B T^*\right)$.

The two electron process is then given by:

$$\Gamma_2 \propto \int \int d\epsilon_1 d\epsilon_2 \; f(\epsilon_1)\big(1 - f(\epsilon_1 + V_b - \Delta/2)\big) \; f(\epsilon_2)\big(1 - f(\epsilon + V_b - \Delta/2)\big) \tag{7.36}$$

$$\Gamma_2 \propto (eV_b - \Delta/2)^2 \tag{7.37}$$

The n-electron process is then:

$$\Gamma_1 \approx \frac{A_1}{\hbar}\left(eV_b - \Delta\right) \tag{7.38}$$

$$\Gamma_2 \approx \frac{A_2}{\hbar^2}\left(eV_b - \frac{\Delta}{2}\right)^2 \tag{7.39}$$

$$\Gamma_n \approx \frac{A_n}{\hbar^n}\left(eV_b - \frac{\Delta}{n}\right)^n \tag{7.40}$$

Where the total rate will be:

$$\Gamma = \sum_n \Gamma_n \tag{7.41}$$

Figure 7.13 shows the inelastic electron scattering fits, including higher order processes. As a toy model the order-n inelastic electron scattering process can be used to fit the observed data. It remains to be seen however, if there can be a physically consistent complete theory.

Barrier thinning or lowering

An alternative for the exponential V_b dependence is a tunnel barrier thinning or lowering process. This was first suggested by Rogers and Buhrman for a TLS seen in their Nb-Nb$_2$O$_5$-PbBi tunnel junctions [56, 58]. In Rogers et. al. the TLS was only trackable in the frequency space, thus only the effective rate $1/\tau = 1/\tau_1 + 1/\tau_2$ was analyzed. Similar to our data, they observed a TLS transition rate that varies exponentially with the applied bias. This effect was attributed to a barrier thinning effect that couples to the transition rate exponentially through

the WKB tunneling probability, giving the TLS tunnel splitting the form:

$$\Delta_0 = \hbar\omega_0 \exp\left[-2d(1 - \gamma e V_b)\sqrt{\frac{2mU}{\hbar^2}}\right], \tag{7.42}$$

where γ is a proportionality factor describing how much the barrier is thinned per applied voltage bias V_b. Additionally Rogers. et. al. argued that the voltage dependence is likely to come from a barrier thinning effect rather than a barrier lowering (ie. couples more to d rather than to the U). This is because the exponential dependence was not seen in the thermally activated regime where the rates are sensitive to the barrier height U, but not the well distance d.

While the barrier thinning conjecture might seem able to explain the exponential V_b-dependence seen in the TLS transition rates, it cannot account for the dependence seen in the ratio of the transition rates, τ_1/τ_2. Since for our TLS, $\Delta \gg \Delta_0$, the TLS energy is $E = \sqrt{\Delta^2 + \Delta_0^2} \approx \Delta$, which means the thermodynamic information is contained in the factors of $\exp(\Delta/kT)$, independent of the tunnel coupling Δ_0. This means that variation in the tunnel coupling Δ_0 does not affect the ratio τ_1/τ_2, contrary to our observed data. Even if $\Delta_0 \sim \Delta$, the TLS dynamics will likely follow that of an incoherent tunneling TLS, in which case the relevant TLS energy is $E = \Delta$ and not that found for coherent tunneling TLSs, $E = \sqrt{\Delta^2 + \Delta_0^2}$.

Unfortunately the data set in Rogers et. al. [56] lacked a full analysis in the time-domain, instead only the effective rate $1/\tau = 1/\tau_1 + 1/\tau_2$ was tracked through spectral analysis. The missing data on the voltage dependence of the ratio τ_1/τ_2 would likely have ruled out barrier thinning as a viable mechanism, or at the very least provided the extra information to see if barrier thinning remains plausible for their data.

7.5   TLS B: Thermally activated TLS

Figure 7.14 plots the time capture of a second trackable TLS, which is labeled as *TLS B*. In contrast to TLS A, TLS B is activated at much higher temperatures ($T \approx 60$ K) and its tunnel
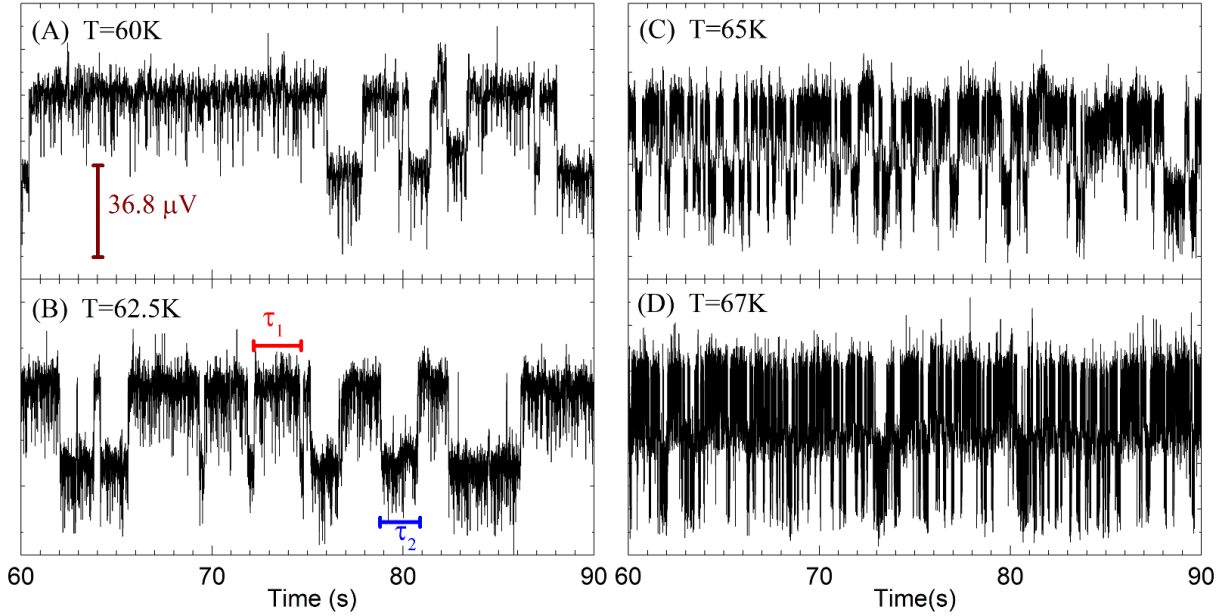
Figure 7.14: TLS B time traces shown for several different temperatures. (A) $T = 60$ K. (B) $T = 62.5$ K. (C) $T = 65$ K. (D) $T = 67$ K, all taken at $V_b = 50$ mV. The lifetimes τ_1 and τ_2 strictly refer to the lifetimes in the higher and lower resistance states respectively.

coupling appears to be very small that there was no apparent crossover to a quantum-limited switching behavior. Figure 7.16A plots the lifetimes τ_1 and τ_2 for TLS B as a function of temperature. Here τ_1 refers to the TLS lifetime in the *higher resistance* state and τ_2 refers to the lifetime in the *lower resistance* state (figure 7.14B).

Numerical fits of the thermally activated rates reveal that the potential barrier heights are $U_1 \approx 151.6$ and $U_2 \approx 146.1$ meV ($\Delta E(V_b = 50$ mV$) \approx 5.5$ meV), which are relatively large compared to TLS A and explains why the tunnel coupling is small. From the numerical fit we also extracted the attempt frequency, $\omega_0 \approx 1 \times 10^{12}$ Hz, in the order of the typical Debye frequencies.

The difference in the governing dynamics between TLS B and TLS A are due to the differences in the potential barrier parameters, and do not necessarily require that the TLSs have an entirely different microscopic origin. In fact the behavior of TLS B is entirely consistent with the picture of a fluctuating atomic dipole, just as in the case of TLS A.

Figure 7.17A shows the switching rates τ_1 and τ_2 at $T = 60$ K as a function of the applied
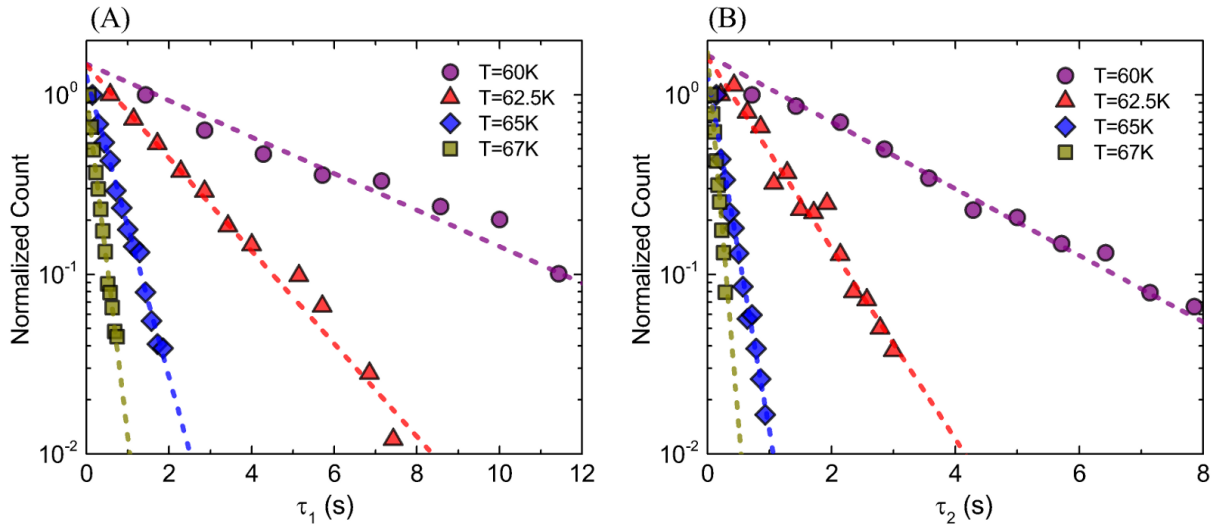
Figure 7.15: TLS B switching histograms for $V_b = 50$ mV shown for several temperature points.
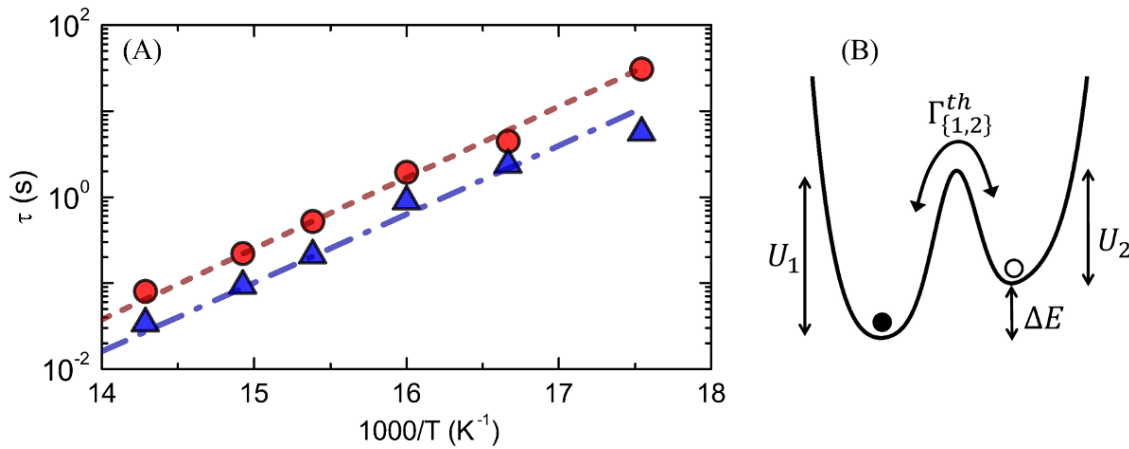
Figure 7.16: (A) Maxwell-Boltzmann over the barrier thermal activation rates, $V_b = 50$ mV. Both TLS lifetimes τ_1 and τ_2 are well fitted (dashed-lines) to the thermal rate, $\tau_i \propto \exp\left(U_i/k_B T\right)$. (B) Potential energy diagram of the TLS.
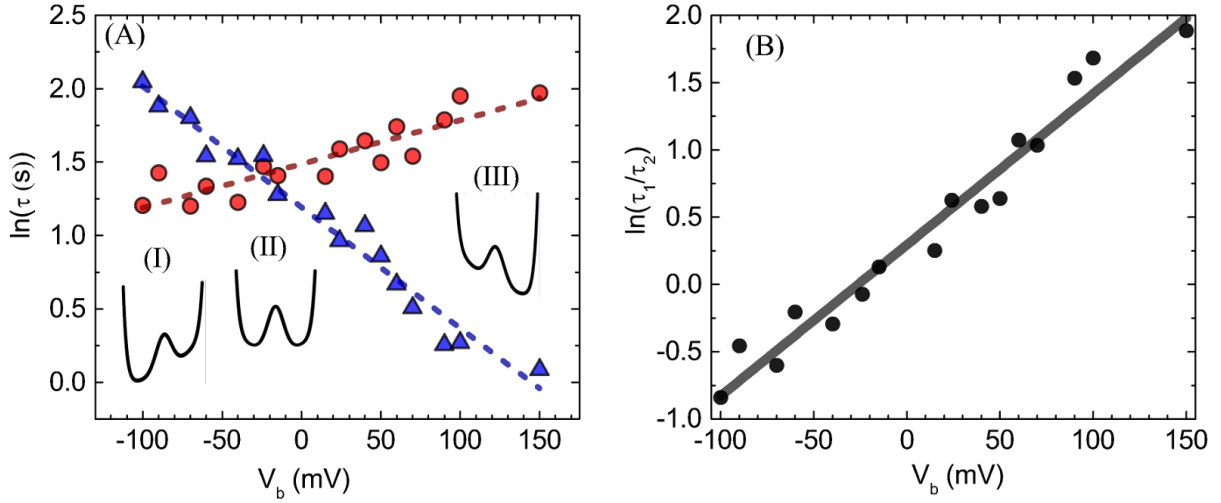
Figure 7.17: (A) The switching rates τ_1 (high resistance) and τ_2 (low resistance) as a function of the applied electric field. (B) The switching ratio $R = \tau_1/\tau_2$ as a function of the applied field. The effect of the TLS dipole interaction with an external **E**-field as a tilting of the double-well potential well. The well tilt energy correction is simply the dipole interaction energy, $\delta E = -\mathbf{p} \cdot \mathbf{E}$.

electric field, $E = V_b/t$, $t \approx 1$ nm. The electric field dependence of τ_1 and τ_2 are monotonic with the opposite signs for the two switching times. This behavior is consistent with the interpretation of the TLS having an electric dipole moment, $\mathbf{p}$, interacting with the applied electric field. The resulting interaction energy, $\delta E = -\mathbf{p} \cdot \mathbf{E}$, tilts the double well potential of the TLS and can even be sufficient to swap the lower energy state, $\tau_1 > \tau_2$, or $\tau_1 < \tau_2$. Note that this behavior is markedly different to that found in Wakai et. al. [73, 72], where the voltage bias dependence of both switching times have the same sign. In Wakai et. al. the random telegraph signal was attributed to the filling and emptying of an electronic trap located within the tunnel barrier. The trap is filled by an electron tunneling from one of the electrode, and is emptied by tunneling to the opposite electrode.

A more detailed examination of the individual switching times in figure 7.17A reveal that the two lifetimes are not symmetrically affected by the applied field (ie. equal magnitudes & opposite signs). For τ_1 the dipole correction to the asymmetry energy is 16.4 μeV/mV$_b$, while for τ_2 the correction is 41.7 μeV/mV$_b$. The difference in the energy correction does have a

natural physical interpretation in that the effective double well potential of the TLS is not exactly symmetric. That is the center of the dipole moment and the maximum of the potential barrier are shifted in coordinate space with respect to each other.

At zero applied field the double well potential of the TLS is tilted with some asymmetry energy, $\Delta E(V_b = 0)$. The dipole energy acts to flip the TLS double well asymmetry, such that at approximately $V_b \approx -23.7$ mV the double well potential is degenerate and the ratio is given by, $\tau_1/\tau_2 = 1$.

Similar to TLS A, the slope in figure 7.17B contains the information on the aligned dipole moment strength of the TLS:

$$k_B T \ln \left(\frac{\tau_1}{\tau_2} \right) = \Delta E_0 + \left(\frac{P \cos \theta}{t} \right) V_b, \qquad (7.43)$$

which gives the aligned dipole moment strength: $|\mathbf{P}| \cos \theta \approx 0.6$ eÅ (using $t \approx 1$ nm), which is consistent with the picture of an effective electronic charge e tunneling over a lattice distance of order 1 Å. Similarly, we can also integrate out the θ dependence (equation 7.23) to get a rough estimate for the dipole moment, $\langle P \rangle_\theta \approx 0.94$ eÅ

7.6 Mechanisms for the modulation of the tunnel barrier due to TLS defects

In the electron trap model proposed by Wakai et. al. [72], the Coulomb repulsion of an occupied trap state blocks the tunneling around a characteristic area δA, leading to the required modulation of the tunneling resistance $\delta R = (\delta A/A)R$.

In the dipole picture, Yu et. al.[13] demonstrated that the dipole potential V_{dip} associated with a TLS can modify the tunnel barrier potential U_0. The tunneling probability is thus:

$$|T|^2 \propto \int_0^L dz \sqrt{\frac{2m}{\hbar^2} \left(U_0 \mp eV_{dip} \right)} \qquad (7.44)$$

The dipole angle θ and the location of the dipoles within the tunnel barrier are randomly

distributed leading to distribution of the effective strength $\delta R/R$ of each dipoles. This is consistent with our observation of a range of δR values in the fluctuators we observed. It was found that the averaged value and the typical TLS densities could ultimately account for the magnitude of the critical current noise in $Al/AlO_x/Al$ junctions.

7.7   Dipole selection for coherent tunneling TLSs

In the tunneling TLS model the eigenstates are given by the symmetric and anti-symmetric linear combinations of the local basis states $|L\rangle$ and $|R\rangle$,

$$|\psi_1\rangle = \cos\frac{\xi}{2}|L\rangle + \sin\frac{\xi}{2}|R\rangle \tag{7.45}$$

$$|\psi_2\rangle = \sin\frac{\xi}{2}|L\rangle - \cos\frac{\xi}{2}|R\rangle, \tag{7.46}$$

where $\tan\xi = \Delta_0/\Delta$. And the dipole moment in the left and right well local states are:

$$p_0 = q\int x\phi_1^*\phi_1\ dx = -q\int x\phi_2^*\phi_2\ dx \tag{7.47}$$

In the tunneling eigenstates, ψ_1 and ψ_2, the dipole can be calculated:

$$p_1 = q\int x\psi_1^*\psi_1\ dx \approx p_0\cos^2\frac{\xi}{2} - p_0\sin^2\frac{\xi}{2} \tag{7.48}$$

$$= p_0\cos\xi \tag{7.49}$$

$$= p_0\frac{\Delta}{E} \tag{7.50}$$

Similarly the dipole in the excited state ψ_2 is given by:

$$p_2 = q\int x\psi_2^*\psi_2\ dx = -p_1 = -p_0\frac{\Delta}{E} \tag{7.51}$$

An important consequence is that if the coupling to the critical current is through the

fluctuation of the dipole moment $\mathbf{p}$, then only the TLSs with non-zero bias ($\Delta \neq 0$) can contribute to the critical current fluctuation. Furthermore, the dominant dipoles are those with $\Delta \gg \Delta_0$, note that most of the TLSs will satisfy this condition since the TLSs are uniform in Δ but is logarithmic in Δ_0: $P(\Delta, \Delta_0) \, d\Delta d\Delta_0 = P_0/\Delta_0 \, d\Delta d\Delta_0$.

CHAPTER 8

FUTURE WORK AND PRELIMINARY RESULTS

8.1 Introduction

In this chapter we will describe preliminary results from two experiments that could form the basis for further work in measurements of critical current noise.

8.2 Piezoelectric response

In chapter 7 we have investigated the TLS electric dipole coupling to an external static electric field. The dipole coupling modifies the energy of the TLS in each localized well by an amount, $\epsilon = -\mathbf{P} \cdot \mathbf{E}$, so that the result of its interaction with an external $\mathbf{E}$-field is a modification of the TLS asymmetry energy by an amount, $\delta\Delta = 2\mathbf{P} \cdot \mathbf{E}$. The *aligned* electric dipole moment, $\tilde{P} = \mathbf{P} \cdot \hat{\mathbf{E}}$, of the TLS can thus be defined as:

$$\tilde{P} = \frac{1}{2} \frac{\partial \Delta}{\partial |\mathbf{E}|} \tag{8.1}$$

Similarly, since the TLS also interacts with the phonon strain field, $\mathbf{S}$, we can define an elastic dipole moment γ given by:

$$\gamma = \frac{1}{2} \frac{\partial \Delta}{\partial |\mathbf{S}|} \tag{8.2}$$

We have fabricated an Al-AlO$_x$-Al junction identical to that measured in chapter 7, but on a 200 μm^2 thick STO substrate. The backside of the STO substrate was coated with 200 nm of gold to form the backgate. To tune the strain in the STO substrate, a backgate voltage V_g

is applied between the backgate and one of the junction electrodes.

SrTiO$_3$ (STO) was chosen as the piezoelectric substrate due to its giant piezoelectric effect at low temperatures. In conventional piezoelectric materials, such as PZT (PbZr$_x$Ti$_{1-x}$O$_3$) or lithium niobates (LiNbO$_3$), the piezoelectric constant tends to diminish at low temperatures. STO however exhibits the inverse behavior where it is a weak piezoelectric at high temperatures but exhibits a giant piezoelectric effect at low temperatures [28].

Unfortunately we have measured only one of such device, while the junction was characterized by a few isolated Lorentzians, the random telegraph signal in the time domain was not sufficiently separated and large enough to submit to a time domain analysis. However we may still provide some analysis of the strain response in the frequency space.

8.2.1 Measurement overview
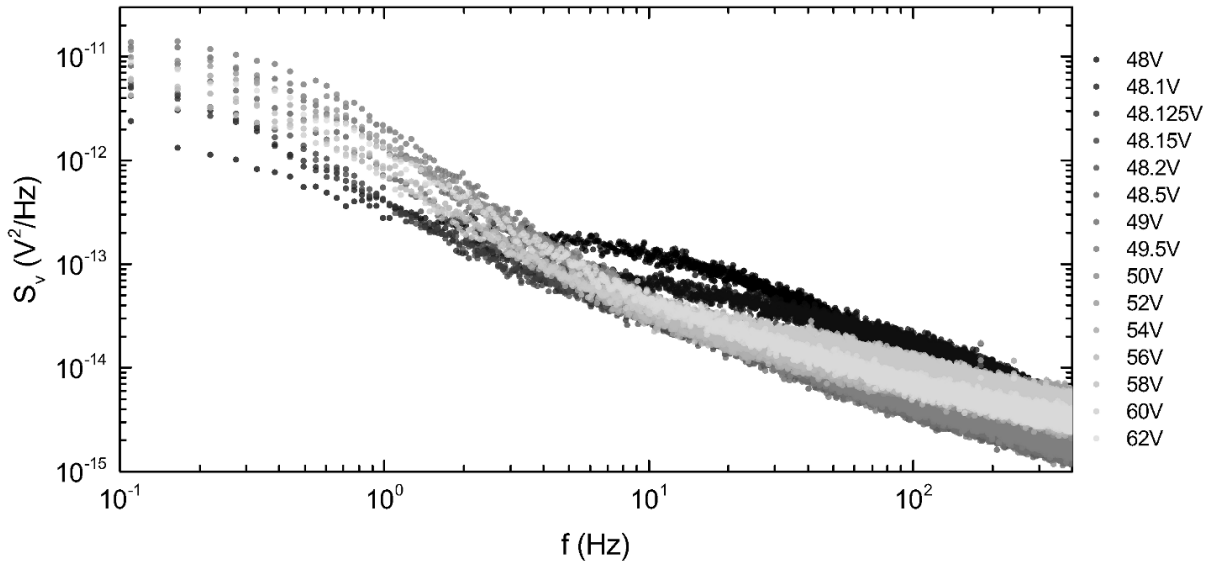
Figure 8.1: Resistance noise at $T = 5$ K, taken at $V_b = 6$ mV with for a range of backgate voltages $V_g = 48 - 62$ V. The traces start with the darker colors at $V_g = 48$ V and the lightest color at $V_g = 62$ V.

The strain response due to an applied electric field is given by:

$$S_{ij} = d_{kij}E_k, \tag{8.3}$$

where for our STO substrate, we find from Grupp and Goldman [28], $d_{xxz} \approx 1 \times 10^{-9}$ m/V. Since our substrate is 200 μm thick, the applied strain per backgate voltage V_g is:

$$\frac{\delta S_{xx}}{\delta V} = 5 \times 10^{-6} \ V_g^{-1} \tag{8.4}$$

Figure 8.1 plots the junction tunneling resistance power spectral density for a range of backgate voltages from $V_g = 48$ V to $V_g = 62$ V, taken at $T = 5$ K and $V_b = 6$ mV. We note two TLSs: TLS-1 with a very low characteristic frequency $f_c \sim 0.8$ Hz, and TLS-2 with $f_c \sim 20-90$ Hz which is clearly seen to move as a function of V_g. It is more difficult to quantify the behavior of TLS-1 since its corner frequency unfortunately lies towards the lower cutoff of our measurement bandwidth. However it would appear that the variance of the random telegraph signal due to TLS-1 is strongly affected by the strain, however the corner frequency cannot be precisely located.

Figure 8.2 shows a detailed view for $V_g = 48$ and 48.1 V. We find that TLS-2 can be fitted with $f_c(V_g = 48\text{V}) \approx 25$ Hz and $f_c(V_g = 48.1\text{V}) \approx 90$ Hz. A change in $\delta V_g = 0.1$ V in the backgate corresponds to a $\delta S \approx 0.5 \times 10^{-6}$ in the substrate strain. Unfortunately TLS-2 moves out of the measurement bandwidth at $V_g \geq 48.125$ V, and we do not have higher bandwidth data to be able to track this TLS.

The behavior of TLS-2 is as expected for a TLS modified by an elastic dipole coupling. The specific details of the TLS corner frequency depends on the TLS dynamics, whether it is thermally activated, or quantum tunneling limited. However, in general the corner frequency will be a function of the TLS asymmetry energy Δ, which is modified by the TLS elastic dipole moment interaction. This behavior is clearly seen in figure 8.2.
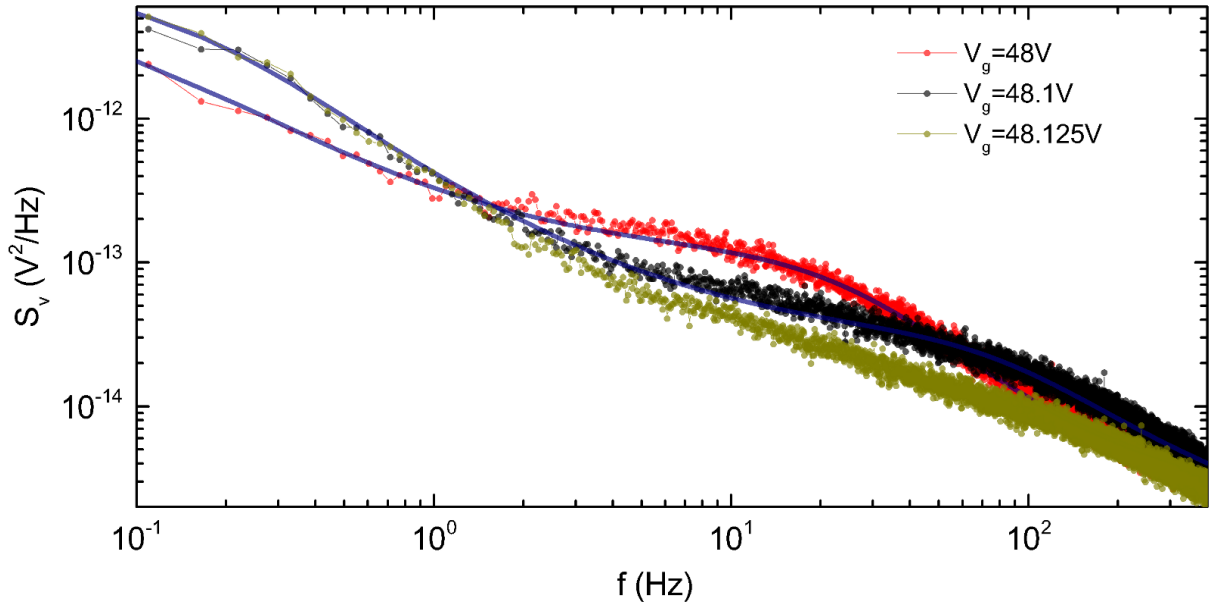
Figure 8.2: Detailed view of the power spectral density for $V_g = 48$, and 48.1 V. $T = 5$ K and $V_b = 6$ mV.

8.2.2   Piezoelectric response at $T = 8$ K

One particular TLS was identified at $T = 8$ K, probed with a voltage bias $V_b = 6$ mV. Figure 8.3 plots the power spectral density showing the TLS Lorentzian at a few selected backgate voltages. This particular TLS has a corner frequency $f_c \approx 2$ Hz, and as a function of applied strain we see an obvious response in the TLS variance and a much weaker dependence in its corner frequency. Figure 8.4A plots the strain response of the TLS variance, and 8.4B plots the strain response of the TLS corner frequency f_c.

For a tunneling TLS with energy splitting $E = \sqrt{\Delta^2 + \Delta_0^2}$, the power spectral density is given by the Lorentzian [74, 38]:

$$S_V(f) = \frac{\delta V^2}{2\pi} \mathrm{sech}^2(E/2kT) \ \frac{f_c}{f_c^2 + f^2},$$ (8.5)

where $\delta V = (\delta R/R)V$ is the change in the junction voltage between the two TLS configurations.

The variance response as a function of the applied strain implies that the TLS energy splitting
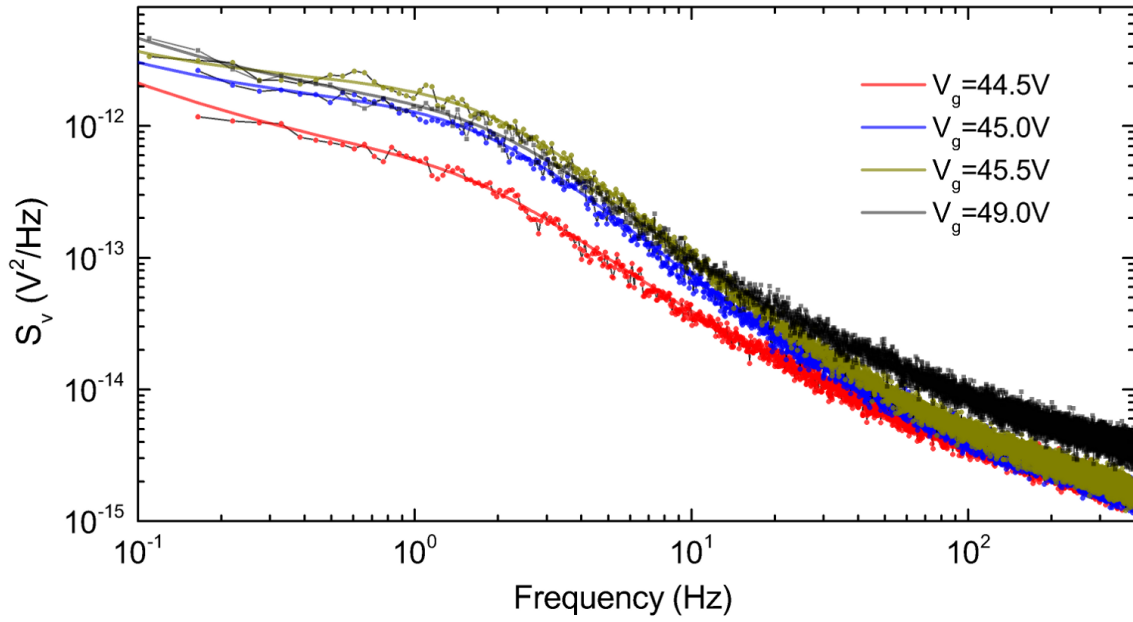
Figure 8.3: Power spectral density at several backgate voltages, $T = 8$ K, $V_b = 6$ mV. One particular TLS is seen to respond to the applied strain, with $f_c \approx 2$ Hz.
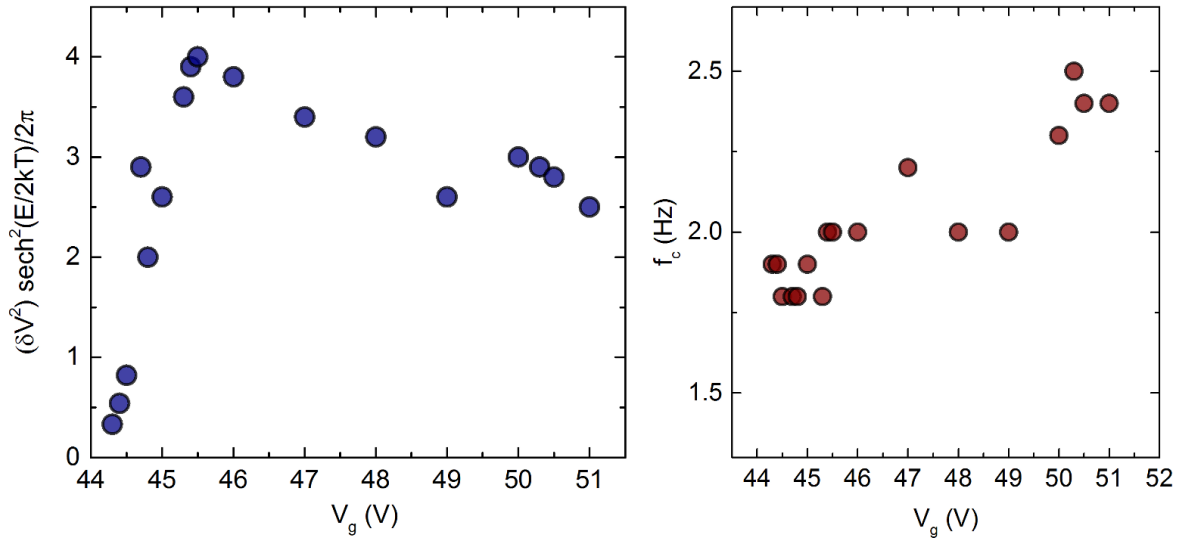
Figure 8.4: (A) Response of the TLS variance, $\delta V^2 \mathrm{sech}^2(E/2kT)$ to the applied strain. (B) Response of the TLS corner frequency to the applied strain.

E is modified by the application of the substrate strain. In particular the cusp feature at $V_g \approx 45.5$ V is reminiscent of a TLS being swept through its energy $\left(E = \sqrt{\Delta^2(V_g) + \Delta_0^2}\right)$ degeneracy point, by the continuous tilting of its asymmetry Δ. Although the strong slope asymmetry between either side of the cusp suggests a more complex behavior, or possibly related to a non-uniform strain-voltage response of the STO piezoelectric substrate.

On the other hand, the TLS corner frequency is seen to have a much weaker response to the applied strain. The corner frequency has a somewhat increasing monotonic trend as the backgate voltage is increased. However the change in the corner frequency through the range of backgate voltages do not exceed $\Delta f_c \sim 0.5$ Hz.

Unfortunately the extraction of the TLS elastic dipole moment requires a much more precise understanding on the exact TLS-strain response, which is currently still lacking.

8.2.3 Conclusions

Clearly a better understanding of the TLS strain response requires a lot more measurements to traverse a fuller parameter space. However these initial results point to an interesting method to probe at the dynamics of the TLSs. Already we can clearly point out that the TLS dynamics are highly affected by the crystal strain. Critically, the way these TLSs couple to the strain field may provide an important evidence to see whether or not they are correctly described by the model of an atomic fluctuator localized in a double-well potential.

We note that Grabovskij et. al. [26] have performed a similar strain tuning experiment in the TLSs coupled to a phase qubit at the qubit frequency. In that experiment they have observed that the energy, $E = \sqrt{\Delta^2 + \Delta_0^2}$, of the TLSs are modified by the applied strain.

8.3   TLSs in an engineered tunnel barrier
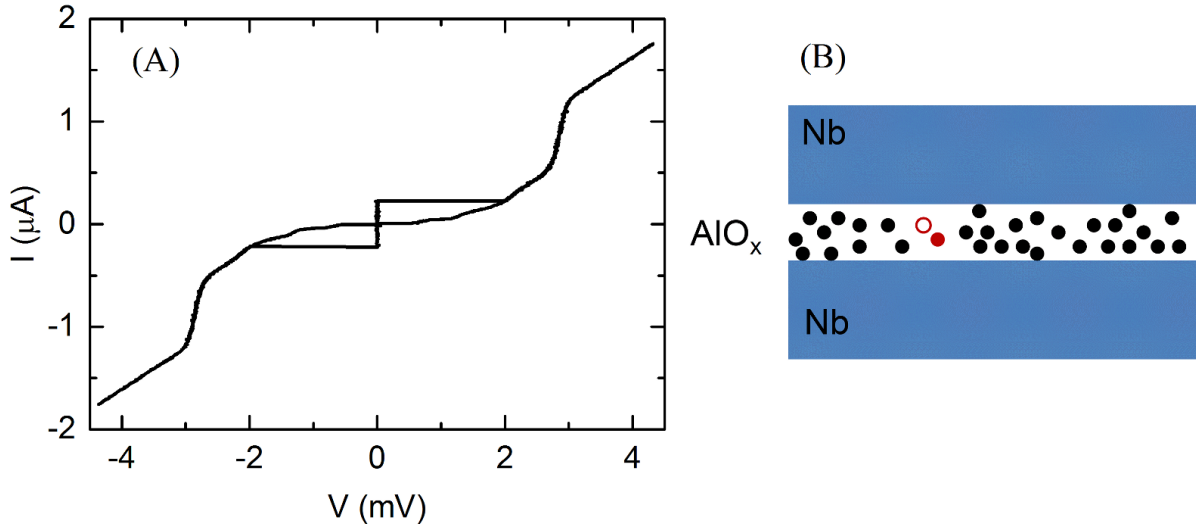
Figure 8.5: (A) IV characteristics of sample e527, a Nb-AlO$_x$-Nb junction with co-deposited tunnel barrier. (B) A cartoon representation of a strongly disordered amorphous AlO$_x$ dielectric. The tunneling characteristics maybe dominated by a small area of extremely thin barrier, with strong local disorder.

In this section we present initial noise measurements on AlO$_x$ tunnel barriers that have been fabricated using methods other than the standard ambient temperature oxygen diffusion. These devices were Nb-AlO$_x$-Nb trilayer junctions, grown by the group of James Eckstein at the University of Illinois at Urbana-Champaign.

In one of their Nb-trilayer architectures [79, 75], the base electrode is a single crystal Nb epitaxially grown on a sapphire substrate, followed by the deposition of a single crystal Al buffer layer. The AlO$_x$ tunnel barrier is then grown by the deposition of Al in a flux of oxygen atoms fed into the system through a gas injection port [79]. The co-deposited AlO$_x$ tunnel barrier typically receives an additional oxygen diffusion step to complete the oxidation, performed at 30 Torr of UHP oxygen for 60 minutes. A top poly-crystalline Nb electrode is then deposited to complete the Nb-trilayer stack.

In one of the samples, sample e527, the trilayer stack was purposefully designed to not include a buffer Al layer, instead it had the AlO$_x$ tunnel barrier co-deposited directly on the
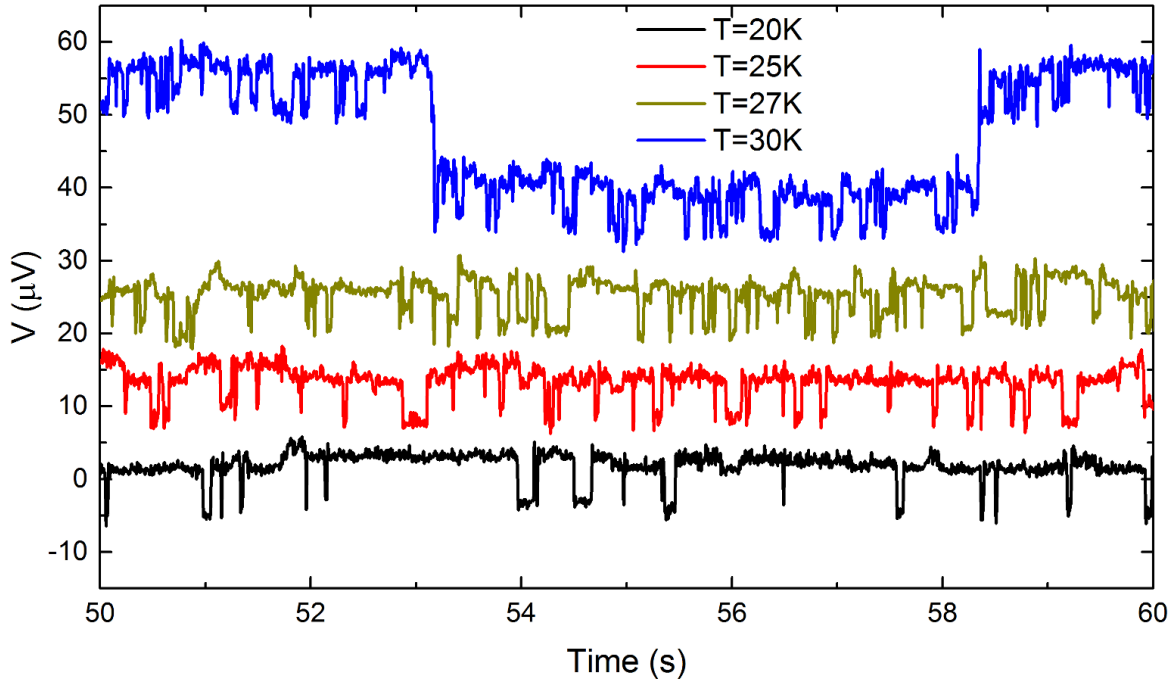
Figure 8.6: Time traces for $T = 20, 25, 27, 30$ K. At $T = 30$ K a second TLS with a larger $\delta A/A$ sets in.

base crystalline Nb electrode. The tunnel barrier is then completed in the standard process with an oxygen diffusion at 30 Torr and 60 minutes at ambient room temperature.

We found that in this particular sample, the tunneling resistance exhibited a strong random telegraph signal. This was unexpected since the junction area was approximately, $A \approx 4 \times 4 \ \mu\text{m}^2$, which we anticipated to have many activated TLSs giving rise to a featureless $1/f^\alpha$ power spectrum. On top of that, the signal due to a single fluctuator, $\delta R/R = \delta A/A \sim 3 \times 10^{-8}$, should have been extremely small given the large junction size.

Figure 8.5A plots the IV transport characteristics at $T = 1.8$ K. The barrier non-uniformity is apparent in the elevated sub-gap leakage current. We conjecture that this could be due to a strong disorder in the amorphous AlO_x tunneling, where some localized regions of the dielectric can have an effectively thinner tunneling barrier, which then dominates the conduction through the junction.

The tunneling resistance of the junction exhibited a strong random telegraph noise, in this
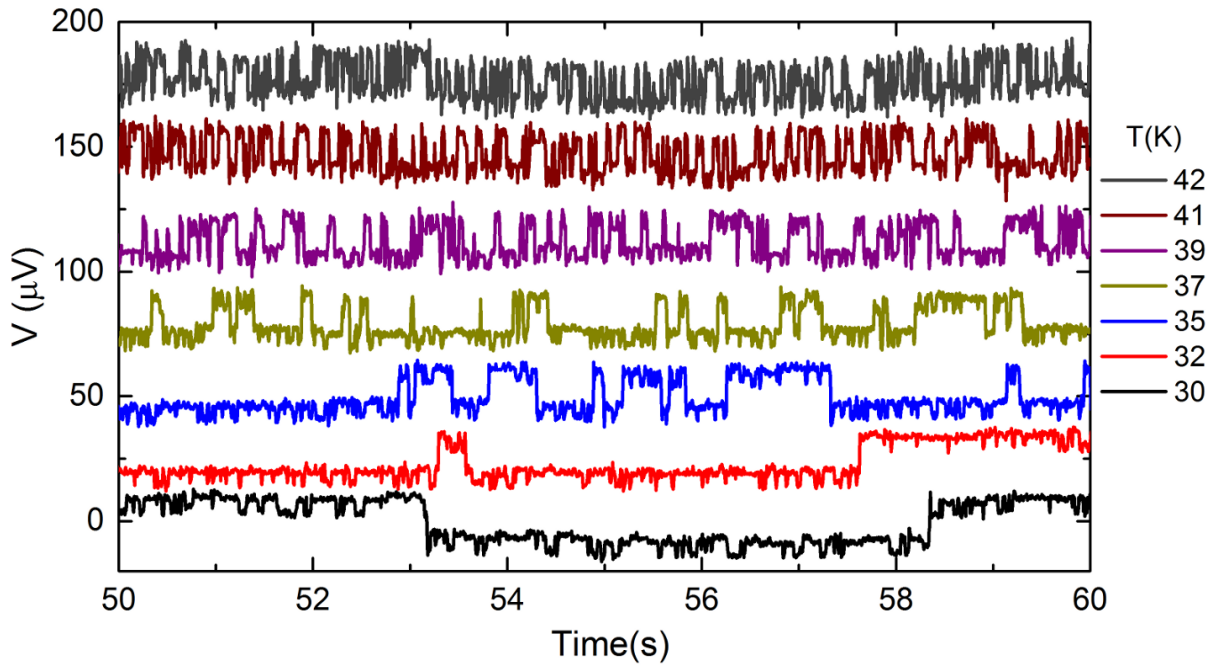
Figure 8.7: Time traces for $T = 30, 32, 35, 37, 39, 41,$ and 42 K, showing the thermal activation of TLS B. TLS A is still visible for some time after TLS B moves into the measurement bandwidth .
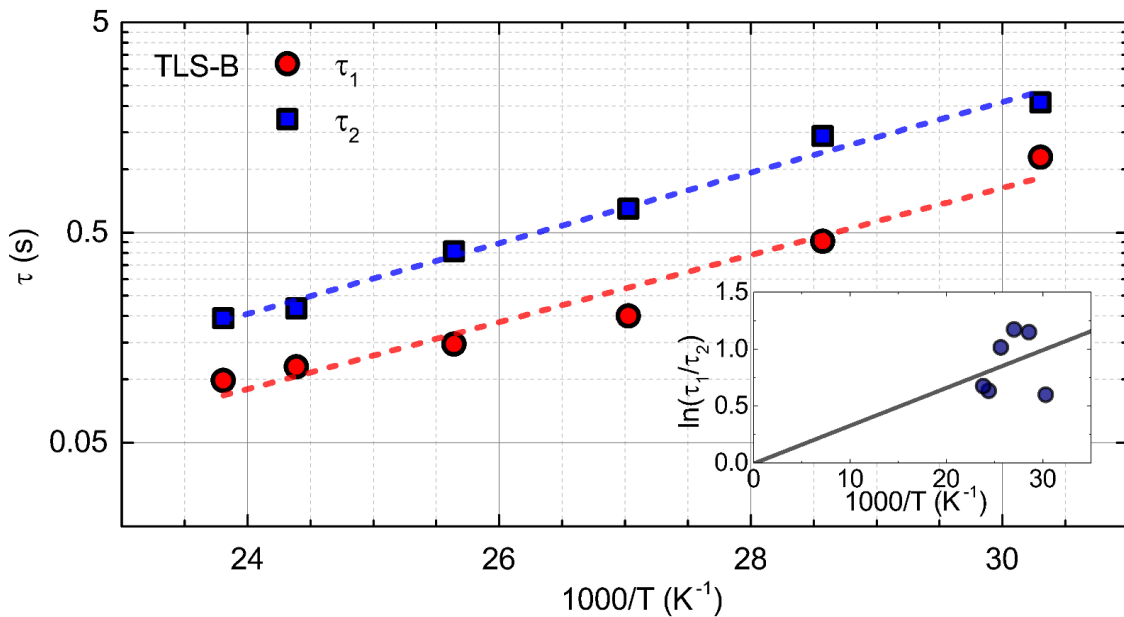
Figure 8.8: Temperature dependence of the switching times for TLS-B, showing thermally activated dynamics. (inset) The TLS lifetime ratio, $\ln(\tau_1/\tau_2)$, and an extrapolated line to high temperatures.

case we were able to resolve two distinct TLSs that have characteristic frequencies spaced far enough from each other to permit their observation. TLS-A is visible in the measurement bandwidth in the temperature range $T \approx 10 - 30$ K, while TLS-B sets in at around $T = 30$ K and dominates the noise spectrum at higher temperatures. A time trace showing the activation of TLS-A is shown in figure 8.6. The activation of TLS-B is given in figure 8.7.

TLS-A has a fractional area, $\delta A / A \approx 1.2 \times 10^{-3}$, while TLS-B is larger at $\delta A / A \approx 2.9 \times 10^{-3}$. While it's not surprising that the TLSs have differing fractional areas, it is extremely unusual in that they both seem to have extremely large effective areas.

For TLS-B we have performed a time domain analysis, identical to the procedure discussed in chapter 7. It was found that TLS-B is governed by a simple thermal activation dynamics, as shown in figure 8.8. The inset in figure 8.8 shows the natural logarithm of the switching lifetime ratio $\ln(\tau_1/\tau_2)$ as a function of $1/T$. Despite the scatter in the data and the limited range, extrapolation to high temperatures $(1/T \to 0)$ is consistent with the ratio $\tau_1/\tau_2 \to 1$. This is consistent with the localized double-well representation of the TLS.

Ultimately e527 was not explored enough to fully understand why these TLSs were visible in such a large junction. However this sample did point out the possibility of investigating the $1/f^\alpha$ low frequency noise and the dynamics of the TLSs, *as a function* of the barrier disorder. The ability to co-deposit the tunnel dielectric and vary its density and stoichiometric composition may prove invaluable in understanding these TLSs.

One crucial lesson is perhaps the value of the ability to *increase* the amount of disorder in the amorphous barrier. We suggest that the oxygen diffusion exposure (pressure $\times$ time) following the co-deposition of the tunnel barrier can be systematically varied to study the noise properties. If the junction can also be made small, $A \sim 0.1$ μm^2, then the TLS dynamics may even be more easily accessible. Importantly, a systematic study of the TLS dynamics as a function of the barrier disorder may provide a connection to microscopic theories of TLSs. One such theory was proposed by DuBois et. al. [15], which attributed the TLSs to a delocalized oxygen in the amorphous AlO_x, and is highly sensitive to the level of disorder.

CHAPTER 9

CONCLUSIONS

Our measurements of the $1/f^\alpha$ noise in $\mathrm{Al/AlO}_x/\mathrm{Al}$ junctions support the linear T-dependence and noise magnitude as previously measured in Eroms. et. al. [18] and Pottorf et. al. [53]. Crucially, we have been able to observe the breakdown of the Gaussian averaging of these TLS ensemble by investigating the noise scaling as a function of the junction area and temperature. In particular, by investigating small junction areas, $A \sim 0.005 - 0.1 \ \mu\mathrm{m}^2$, we have been able to observe the deviation from a featureless $1/f^\alpha$ spectral shape, by the appearance of pronounced Lorentzians. By quantifying the spectral variance, $\langle (\omega \delta S)^2 \rangle / \langle \omega S \rangle^2$, we were able to deduce the TLS defect density, n:

$$n \approx 2.53 \ \mu\mathrm{m}^2 \mathrm{K}^{-1} e^{-1} \rightarrow \sigma_0 \sim 69.7 \ \mu\mathrm{m}^{-2} \mathrm{K}^{-1} \tag{9.1}$$

This TLS density is curiously consistent with that obtained from heat capacity/thermal conductivity/ultrasound absorption experiments which first suggested the existence of two level systems in glassy insulators [51, 82]. In addition this density is also similar to that deduced from counting the density of spurious avoided level crossings in qubit energy spectroscopy [65]. The consistency of the TLS density obtained across vastly different experiments is a strong indication that the defects seen from critical current noise, avoided level crossings at the qubit frequency, and even resonator losses originate from the same ensemble (source), namely the amorphous native oxides (AlO_x, NbO_x, ...) which is the dielectric consistently encountered in superconducting quantum circuits. Combining this estimated density with the measured $1/f$ power spectral density in large junctions, we are able to deduce the average fluctuator

strength, $\langle \delta A^2 \rangle \approx (0.3 \text{ nm}^2)^2$.

In ultra-small junctions, we have been able to isolate a single fluctuator and studied the dynamics of the TLS transitions. The observed tunneling rates of the individual TLS support the conjecture that the fluctuating species is an atomic mass tunneling over distances of order, ~ 1 Å. The electric dipole moment obtained from the TLS response to an external static electric field is estimated to be in the order of, $\sim 0.5 - 1 \ e$Å $\approx 2 - 5$ D. While we conclude that the fluctuating species is likely to be an atomic species (as opposed to electrons), the precision of our estimate is not sufficient to single out the most probable atomic mass.

At the beginning of this project the question of critical current noise in qubits equated to asking: what is the magnitude of the $1/f$ noise, and is it or will it ever be large enough to limit qubit coherence? Our experiments have shown that the junctions and temperature in the typical qubit operation is well below the threshold for the breakdown of $1/f$ noise. On the other hand, our results suggest that the same TLSs that caused $1/f$ critical current noise are the same TLS species that currently limit resonator losses in qubit operation.

In approaching a modern problem in the form of decoherence in superconducting qubits, we have re-entered a field that was started over four decades ago with the first observation of anomalous heat capacity in insulating glasses [82].

REFERENCES

[1] AMBEGAOKAR, V. and BARATOFF, A., "Tunneling between superconductors," *Phys. Rev. Lett.*, vol. 11, pp. 104–104, Jul 1963.

[2] ANDERSON, P. W., HALPERIN, B. I., and VARMA, C. M., "Anomalous low-temperature thermal properties of glasses and spin glasses," *Philosophical Magazine*, vol. 25, no. 1, pp. 1–9, 1972.

[3] ANSARI, M. H. and WILHELM, F. K., "Noise and microresonance of critical current in josephson junction induced by kondo trap states," *Phys. Rev. B*, vol. 84, p. 235102, Dec 2011.

[4] ANTON, S. A., *Magnetic flux noise in SQUIDs and qubits.* PhD thesis, University of California, Berkeley, 2013.

[5] ANTON, S. M., NUGROHO, C. D., BIRENBAUM, J. S., O'KELLEY, S. R., ORLYANCHIK, V., DOVE, A. F., OLSON, G. A., YOSCOVITS, Z. R., ECKSTEIN, J. N., VAN HARLINGEN, D. J., and CLARKE, J., "Low-frequency critical current noise in josephson junctions induced by temperature fluctuations," *Applied Physics Letters*, vol. 101, no. 9, pp. –, 2012.

[6] ASTAFIEV, O., PASHKIN, Y. A., NAKAMURA, Y., YAMAMOTO, T., and TSAI, J. S., "Temperature square dependence of the low frequency $1/f$ charge noise in the josephson junction qubits," *Phys. Rev. Lett.*, vol. 96, p. 137001, Apr 2006.

[7] BARDEEN, J., COOPER, L. N., and SCHRIEFFER, J. R., "Theory of superconductivity," *Phys. Rev.*, vol. 108, pp. 1175–1204, Dec 1957.

[8] BARENDS, R., KELLY, J., MEGRANT, A., SANK, D., JEFFREY, E., CHEN, Y., YIN, Y., CHIARO, B., MUTUS, J., NEILL, C., O'MALLEY, P., ROUSHAN, P., WENNER, J., WHITE, T. C., CLELAND, A. N., and MARTINIS, J. M., "Coherent josephson qubit suitable for scalable quantum integrated circuits," *Phys. Rev. Lett.*, vol. 111, p. 080502, Aug 2013.

[9] BARENDS, R., KELLY, J., MEGRANT, A., VEITIA, A., SANK, D., JEFFREY, E., WHITE, T. C., MUTUS, J., FOWLER, A. G., CAMPBELL, B., CHEN, Y., CHEN, Z., CHIARO, B., DUNSWORTH, A., NEILL, C., OMALLEY, P., ROUSHAN, P., VAINSENCHER, A., WENNER, J., KOROTKOV, A. N., CLELAND, A. N., and MARTINIS, J. M., "Superconducting

quantum circuits at the surface code threshold for fault tolerance," *Nature*, vol. 508, pp. 500–503, apr 2014.

[10] BERRET, J. and MEINER, M., "How universal are the low temperature acoustic properties of glasses?," *Zeitschrift fr Physik B Condensed Matter*, vol. 70, no. 1, pp. 65–72, 1988.

[11] CHEN, W., PATEL, V., and LUKENS, J., "Fabrication of high-quality josephson junctions for quantum computation using a self-aligned process," *Microelectronic Engineering*, vol. 73-74, pp. 767 – 772, 2004.

[12] CLARKE, J. and WILHELM, F. K., "Superconducting quantum bits," *Nature*, vol. 453, pp. 1031–1042, June 2008.

[13] CONSTANTIN, M. and YU, C. C., "Microscopic model of critical current noise in josephson junctions," *Phys. Rev. Lett.*, vol. 99, p. 207001, Nov 2007.

[14] CRANE, T. A., *Low-frequency $1/f$ noise: Low temperature measurements and effect on superconducting qubit dephasing.* PhD thesis, University of Illinois at Urbana-Champaign, 2005.

[15] DUBOIS, T. C., PER, M. C., RUSSO, S. P., and COLE, J. H., "Delocalized oxygen as the origin of two-level defects in josephson junctions," *Phys. Rev. Lett.*, vol. 110, p. 077002, Feb 2013.

[16] DUTTA, P., DIMON, P., and HORN, P. M., "Energy scales for noise processes in metals," *Phys. Rev. Lett.*, vol. 43, pp. 646–649, Aug 1979.

[17] DUTTA, P. and HORN, P. M., "Low-frequency fluctuations in solids: $1/f$ noise," *Rev. Mod. Phys.*, vol. 53, pp. 497–516, Jul 1981.

[18] EROMS, J., VAN SCHAARENBURG, L. C., DRIESSEN, E. F. C., PLANTENBERG, J. H., HUIZINGA, C. M., SCHOUTEN, R. N., VERBRUGGEN, A. H., HARMANS, C. J. P. M., and MOOIJ, J. E., "Low-frequency noise in josephson junctions for superconducting qubits," *Applied Physics Letters*, vol. 89, no. 12, pp. –, 2006.

[19] FAORO, L. and IOFFE, L. B., "Quantum two level systems and kondo-like traps as possible sources of decoherence in superconducting qubits," *Phys. Rev. Lett.*, vol. 96, p. 047001, Jan 2006.

[20] FAORO, L. and IOFFE, L. B., "Microscopic origin of critical current fluctuations in large, small, and ultra-small area josephson junctions," *Phys. Rev. B*, vol. 75, p. 132505, Apr 2007.

[21] FAORO, L., KITAEV, A., and IOFFE, L. B., "Quasiparticle poisoning and josephson current fluctuations induced by kondo impurities," *Phys. Rev. Lett.*, vol. 101, p. 247002, Dec 2008.

[22] GARFUNKEL, G. A., ALERS, G. B., and WEISSMAN, M. B., "Mesoscopic noise studies of atomic motions in cold amorphous conductors," *Phys. Rev. B*, vol. 41, pp. 4901–4919, Mar 1990.

[23] GARFUNKEL, G. A., *Universal conductance fluctuations, glassy kinetics, and $1/f$ noise.* PhD thesis, University of Illinois at Urbana-Champaign, 1989.

[24] GOLDING, B., GRAEBNER, J. E., KANE, A. B., and BLACK, J. L., "Relaxation of tunneling systems by conduction electrons in a metallic glass," *Phys. Rev. Lett.*, vol. 41, pp. 1487–1491, Nov 1978.

[25] GORDON, J. M. and GOLDMAN, A. M., "Electron inelastic scattering in aluminum films and wires at temperatures near the superconducting transition," *Phys. Rev. B*, vol. 34, pp. 1500–1507, Aug 1986.

[26] GRABOVSKIJ, G. J., PEICHL, T., LISENFELD, J., WEISS, G., and USTINOV, A. V., "Strain tuning of individual atomic tunneling systems detected by a superconducting qubit," *Science*, vol. 338, no. 6104, pp. 232–234, 2012.

[27] GREENBERG, Y. S., IZMALKOV, A., GRAJCAR, M., IL'ICHEV, E., KRECH, W., MEYER, H.-G., AMIN, M. H. S., and VAN DEN BRINK, A. M., "Low-frequency characterization of quantum tunneling in flux qubits," *Phys. Rev. B*, vol. 66, p. 214525, Dec 2002.

[28] GRUPP, D. E. and GOLDMAN, A. M., "Giant piezoelectric effect in strontium titanate at cryogenic temperatures," *Science*, vol. 276, no. 5311, pp. 392–394, 1997.

[29] HOUCK, A. A., KOCH, J., DEVORET, M. H., GIRVIN, S. M., and SCHOELKOPF, R. J. *Quantum Inf. Process.*, vol. 8, no. 2-3, pp. 105–115, 2009.

[30] ISRAELOFF, N. E., WEISSMAN, M. B., NIEUWENHUYS, G. J., and KOSIOROWSKA, J., "Electrical noise from spin fluctuations in cumn," *Phys. Rev. Lett.*, vol. 63, pp. 794–797, Aug 1989.

[31] JULIN, J. K., KOPPINEN, P. J., and MAASILTA, I. J., "Reduction of low-frequency $1/f$ noise in al-alo$_x$-al tunnel junctions by thermal annealing," *Applied Physics Letters*, vol. 97, no. 15, 2010.

[32] KAUTZ, R. L., ZIMMERLI, G., and MARTINIS, J. M., "Self-heating in the coulomb-blockade electrometer," *Journal of Applied Physics*, vol. 73, no. 5, pp. 2386–2396, 1993.

[33] KENYON, M., COBB, J., AMAR, A., SONG, D., ZIMMERMAN, N., LOBB, C., and WELLSTOOD, F., "Dynamics of a charged fluctuator in an al-alo$_x$-al single-electron transistor," *Journal of Low Temperature Physics*, vol. 123, no. 1-2, pp. 103–126, 2001.

[34] KENYON, M., LOBB, C. J., and WELLSTOOD, F. C., "Temperature dependence of low-frequency noise in alal2o3al single-electron transistors," *Journal of Applied Physics*, vol. 88, pp. 6536–6540, Dec. 2000.

[35] KHALIL, M., *A study of two-level system defects in dielectric films using superconducting resonators.* PhD thesis, University of Maryland, 2014.

[36] KLINE, J. S., VISSERS, M. R., DA SILVA, F. C. S., WISBEY, D. S., WEIDES, M., WEIR, T. J., TUREK, B., BRAJE, D. A., OLIVER, W. D., SHALIBO, Y., KATZ, N., JOHNSON, B. R., OHKI, T. A., and PAPPAS, D. P., "Sub-micrometer epitaxial josephson junctions for quantum circuits," *Superconductor Science and Technology*, vol. 25, no. 2, p. 025005, 2012.

[37] KOCH, J., YU, T. M., GAMBETTA, J., HOUCK, A. A., SCHUSTER, D. I., MAJER, J., BLAIS, A., DEVORET, M. H., GIRVIN, S. M., and SCHOELKOPF, R. J. *Phys. Rev. A*, vol. 76, p. 042319, 2007.

[38] KOGAN, S., *Electronic Noise and Fluctuations in Solids.* Cambridge University Press, 2008.

[39] LISENFELD, J., MÜLLER, C., COLE, J. H., BUSHEV, P., LUKASHENKO, A., SHNIRMAN, A., and USTINOV, A. V., "Measuring the temperature dependence of individual two-level systems by direct coherent control," *Phys. Rev. Lett.*, vol. 105, p. 230504, Dec 2010.

[40] MACHLUP, S., "Noise in semiconductors: Spectrum of a two parameter random signal," *Journal of Applied Physics*, vol. 25, pp. 341–343, Mar. 1954.

[41] MANDELBROT, B. B. and WALLIS, J. R., "Some long-run properties of geophysical records," *Water Resources Research*, vol. 5, no. 2, pp. 321–340, 1969.

[42] MANUCHARYAN, V. E., KOCH, J., GLAZMAN, L. I., and DEVORET, M. H., "Fluxonium: Single cooper-pair circuit free of charge offsets," *Science*, vol. 326, no. 5949, pp. 113–116, 2009.

[43] MARTINIS, J. M., COOPER, K. B., MCDERMOTT, R., STEFFEN, M., ANSMANN, M., OSBORN, K. D., CICAK, K., OH, S., PAPPAS, D. P., SIMMONDS, R. W., and YU, C. C., "Decoherence in josephson qubits from dielectric loss," *Phys. Rev. Lett.*, vol. 95, p. 210503, Nov 2005.

[44] MÜCK, M., KORN, M., MUGFORD, C. G. A., KYCIA, J. B., and CLARKE, J., "Measurements of 1/f noise in josephson junctions at zero voltage: Implications for decoherence in superconducting quantum bits," *Applied Physics Letters*, vol. 86, no. 1, pp. –, 2005.

[45] MURCH, K. W., WEBER, S. J., LEVENSON-FALK, E. M., VIJAY, R., and SIDDIQI, I., "1/f noise of josephson-junction-embedded microwave resonators at single photon energies and millikelvin temperatures," *Applied Physics Letters*, vol. 100, no. 14, pp. –, 2012.

[46] OH, S., CICAK, K., KLINE, J. S., SILLANPÄÄ, M. A., OSBORN, K. D., WHITTAKER, J. D., SIMMONDS, R. W., and PAPPAS, D. P., "Elimination of two level fluctuators in superconducting quantum bits by an epitaxial tunnel barrier," *Phys. Rev. B*, vol. 74, p. 100502, Sep 2006.

[47] PAIK, H., SCHUSTER, D. I., BISHOP, L. S., CATELANI, G., SEARS, A. P., JOHNSON, B. R., REAGOR, M. J., FRUNZIO, L., GLAZMAN, L., GIRVIN, S. M., DEVORET, M. H., and SCHOELKOPF, R. J. *Phys. Rev. Lett.*, vol. 107, p. 240501, 2011.

[48] PALADINO, E., GALPERIN, Y. M., FALCI, G., and ALTSHULER, B. L., "$1/f$ noise: Implications for solid-state quantum information," *Rev. Mod. Phys.*, vol. 86, pp. 361–418, Apr 2014.

[49] PHILLIPS, W. A., "Two-level states in glasses," *Reports on Progress in Physics*, vol. 50, no. 12, p. 1657, 1987.

[50] PHILLIPS, W., "Tunneling states in amorphous solids," *Journal of Low Temperature Physics*, vol. 7, no. 3-4, pp. 351–360, 1972.

[51] PHILLIPS, W., *Amorphous solids: low-temperature properties*. Topics in current physics, Springer-Verlag, 1981.

[52] PLOURDE, B. L. T., ROBERTSON, T. L., REICHARDT, P. A., HIME, T., LINZEN, S., WU, C. E., and CLARKE, J. *Phys. Rev. B.*, vol. 72, p. 060506(R), 2005.

[53] POTTORF, S., PATEL, V., and LUKENS, J. E., "Temperature dependence of critical current fluctuations in nb/alox/nb josephson junctions," *Applied Physics Letters*, vol. 94, no. 4, pp. –, 2009.

[54] ROGERS, C. T. and BUHRMAN, R. A. *IEEE Transactions on Magnetics*, vol. MAG-19, no. 3, p. 453, 1983.

[55] ROGERS, C. T. and BUHRMAN, R. A., "Composition of $1/f$ noise in metal-insulator-metal tunnel junctions," *Phys. Rev. Lett.*, vol. 53, pp. 1272–1275, Sep 1984.

[56] ROGERS, C. T. and BUHRMAN, R. A., "Nature of single-localized-electron states derived from tunneling measurements," *Phys. Rev. Lett.*, vol. 55, pp. 859–862, Aug 1985.

[57] ROGERS, C. T. and BUHRMAN, R., "Discrete lorentzian structure in low frequency voltage noise spectra of very small area josephson tunnel junctions," *Magnetics, IEEE Transactions on*, vol. 21, pp. 126–129, Mar 1985.

[58] ROGERS, C. T., *A study of individual electron trapping centers and $1/f$ noise in metal-insulator-metal tunnel junctions*. PhD thesis, Cornell University, 1987.

[59] ROUKES, M. L., FREEMAN, M. R., GERMAIN, R. S., RICHARDSON, R. C., and KETCHEN, M. B., "Hot electrons and energy transport in metals at millikelvin temperatures," *Phys. Rev. Lett.*, vol. 55, pp. 422–425, Jul 1985.

[60] SAVO, B., WELLSTOOD, F. C., and CLARKE, J., "Low-frequency excess noise in nb-al$_2$o$_3$-nb josephson tunnel junctions," *Applied Physics Letters*, vol. 50, no. 24, pp. 1757–1759, 1987.

[61] SCHREIER, J. A., HOUCK, A. A., KOCH, J., SCHUSTER, D. I., JOHNSON, B. R., CHOW, J. M., GAMBETTA, J. M., MAJER, J., FRUNZIO, L., DEVORET, M. H., GIRVIN, S. M., and SCHOELKOPF, R. J. *Phys. Rev. B*, vol. 77, p. 180502(R), 2008.

[62] SCOFIELD, J. H., "ac method for measuring lowfrequency resistance fluctuation spectra," *Review of Scientific Instruments*, vol. 58, pp. 985–993, June 1987.

[63] SENDELBACH, S., HOVER, D., KITTEL, A., MÜCK, M., MARTINIS, J. M., and McDERMOTT, R., "Magnetism in squids at millikelvin temperatures," *Phys. Rev. Lett.*, vol. 100, p. 227006, Jun 2008.

[64] SHANKAR, R., *Principles of Quantum Mechanics*. Springer, 1994.

[65] STOUTIMORE, M. J. A., KHALIL, M. S., LOBB, C. J., and OSBORN, K. D., "A josephson junction defect spectrometer for measuring two-level systems," *Applied Physics Letters*, vol. 101, no. 6, 2012.

[66] SWIHART, J. C., "Solutions of the bcs integral equation and deviations from the law of corresponding states," *IBM Journal of Research and Development*, vol. 6, pp. 14–23, Jan 1962.

[67] VAN HARLINGEN, D. J., ROBERTSON, T. L., PLOURDE, B. L. T., REICHARDT, P. A., CRANE, T. A., and CLARKE, J., "Decoherence in josephson-junction qubits due to critical-current fluctuations," *Phys. Rev. B*, vol. 70, p. 064517, Aug 2004.

[68] VINANTE, A., FALFERI, P., MEZZENA, R., and MÜCK, M., "Hot-electron effect in palladium thin films," *Phys. Rev. B*, vol. 75, p. 104303, Mar 2007.

[69] VLADAR, K. and ZAWADOWSKI, A., "Theory of the interaction between electrons and the two-level system in amorphous metals. i. noncommutative model hamiltonian and scaling of first order," *Phys. Rev. B*, vol. 28, pp. 1564–1581, Aug 1983.

[70] VOSS, R. F. and CLARKE, J., "$1/f$ noise in music and speech," *Nature*, vol. 258, no. 5533, pp. 317–318, 1975.

[71] VOSS, R. F. and CLARKE, J., "Flicker $(1/f)$ noise: Equilibrium temperature and resistance fluctuations," *Phys. Rev. B*, vol. 13, pp. 556–573, Jan 1976.

[72] WAKAI, R. T., *Fluctuations in dc-SQUIDs: Quantum noise effects, low frequency noise, and single electron trapping*. PhD thesis, University of Illinois at Urbana-Champaign, 2013.

[73] WAKAI, R. T. and VAN HARLINGEN, D. J., "Direct lifetime measurements and interactions of charged defect states in submicron josephson junctions," *Phys. Rev. Lett.*, vol. 58, pp. 1687–1690, Apr 1987.

[74] WEISSMAN, M. B., "$1/f$ noise and other slow, nonexponential kinetics in condensed matter," *Rev. Mod. Phys.*, vol. 60, pp. 537–571, Apr 1988.

[75] WELANDER, P. B., *Epitaxial aluminum oxide thin films on niobium (110): A study of their growth and their use in superconducting tunnel junctions.* PhD thesis, University of Illinois at Urbana-Champaign, 2007.

[76] WELLSTOOD, F. C., URBINA, C., and CLARKE, J., "Hot-electron effects in metals," *Phys. Rev. B*, vol. 49, pp. 5942–5955, Mar 1994.

[77] WELLSTOOD, F. C., URBINA, C., and CLARKE, J., "Flicker $(1/f)$ noise in the critical current of josephson junctions at 0.094.2k," *Applied Physics Letters*, vol. 85, no. 22, pp. 5296–5298, 2004.

[78] WELLSTOOD, F. C., *Excess noise in the dc SQUID: 4.2K to 20mK*. PhD thesis, University of California, Berkeley, 1988.

[79] YOSCOVITS, Z. R., *Study of the effects of surface cladding on 3D transmon*. PhD thesis, University of Illinois at Urbana-Champaign, 2014.

[80] YOSHIHARA, F., HARRABI, K., NISKANEN, A. O., NAKAMURA, Y., and TSAI, J. S., "Decoherence of flux qubits due to $1/f$ flux noise," *Phys. Rev. Lett.*, vol. 97, p. 167001, Oct 2006.

[81] YU, C. C., "Why study noise due to two level systems: A suggestion for experimentalists," *Journal of Low Temperature Physics*, vol. 137, no. 3-4, pp. 251–265, 2004.

[82] ZELLER, R. C. and POHL, R. O., "Thermal conductivity and specific heat of noncrystalline solids," *Phys. Rev. B*, vol. 4, pp. 2029–2041, Sep 1971.

[83] ZIEL, A. V. D., "On the noise spectra of semi-conductor noise and of flicker effect," *Physica*, vol. 16, no. 4, pp. 359 – 372, 1950.

[84] ZIEL, A. V. D., "Flicker noise in electronic devices," vol. 49, pp. 225–297, 1979.

[85] ZMUIDZINAS, J., "Superconducting microresonators: Physics and applications," *Annual Review of Condensed Matter Physics*, vol. 3, no. 1, pp. 169–214, 2012.

[86] ZORIN, A. B., AHLERS, F.-J., NIEMEYER, J., WEIMANN, T., WOLF, H., KRUPENIN, V. A., and LOTKHOV, S. V., "Background charge noise in metallic single-electron tunneling devices," *Phys. Rev. B*, vol. 53, pp. 13682–13687, May 1996.